Applying Lidar and High-Resolution Multispectral Imagery for Improved Quantification and Mapping of Tundra Vegetation Structure and Distribution in the Alaskan Arctic

A Dissertation

Presented in Partial Fulfillment of the Requirements for the

Degree of Doctorate of Philosophy

with a

Major in Natural Resources

in the

College of Graduate Studies

University of Idaho

by

Heather E. Greaves

Major Professor: Jan U.H. Eitel, Ph.D.

Committee Members: Lee A. Vierling, Ph.D.; Natalie T. Boelman, Ph.D.; Kevin L. Griffin, Ph.D.

Department Administrator: Lee A. Vierling, Ph.D.

August 2017

AUTHORIZATION TO SUBMIT DISSERTATION

This dissertation of Heather E. Greaves, submitted for the degree of Doctorate of Philosophy with a Major in Natural Resources and titled "Applying Lidar and High-Resolution Multispectral Imagery for Improved Quantification and Mapping of Tundra Vegetation Structure and Distribution in the Alaskan Arctic," has been reviewed in final form. Permission, as indicated by the signatures and dates below, is now granted to submit final copies to the College of Graduate Studies for approval.

Major Professor: _____ Date: _____
Jan U.H. Eitel, Ph.D.

Committee Members: _____ Date: _____
Lee A. Vierling, Ph.D.

_____ Date: _____
Natalie T. Boelman, Ph.D.

_____ Date: _____
Kevin L. Griffin, Ph.D.

Department Administrator: _____ Date: _____
Lee A. Vierling, Ph.D.

ABSTRACT

Climate change is disproportionately affecting high northern latitudes, and the extreme temperatures, remoteness, and sheer size of the Arctic tundra biome have always posed challenges that make application of remote sensing technology especially appropriate. Advances in high-resolution remote sensing continually improve our ability to measure characteristics of tundra vegetation communities, which have been difficult to characterize previously due to their low stature and their distribution in complex, heterogeneous patches across large landscapes.

In this work, I apply terrestrial lidar, airborne lidar, and high-resolution airborne multispectral imagery to estimate tundra vegetation characteristics for a research area near Toolik Lake, Alaska. Initially, I explored methods for estimating shrub biomass from terrestrial lidar point clouds, finding that a canopy-volume based algorithm performed best. Although shrub biomass estimates derived from airborne lidar data were less accurate than those from terrestrial lidar data, algorithm parameters used to derive biomass estimates were similar for both datasets. Additionally, I found that airborne lidar-based shrub biomass estimates were just as accurate whether calibrated against terrestrial lidar data or harvested shrub biomass—suggesting that terrestrial lidar potentially could replace destructive biomass harvest.

Along with smoothed Normalized Differenced Vegetation Index (NDVI) derived from airborne imagery, airborne lidar-derived canopy volume was an important predictor in a Random Forest model trained to estimate shrub biomass across the 12.5 km^2 covered by our lidar and imagery data. The resulting 0.80 m resolution shrub biomass maps should provide important benchmarks for change detection in the Toolik area, especially as deciduous shrubs continue to expand in tundra regions. Finally, I applied 33 lidar- and imagery-derived predictor layers in a validated Random Forest modeling approach to map vegetation community distribution at 20 cm resolution across the data collection area, creating maps that will enable validation of coarser maps, as well as study of fine-scale ecological processes in the area.

These projects have pushed the limits of what can be accomplished for vegetation mapping using airborne remote sensing in a challenging but important region; it is my hope that the methods explored here will illuminate potential paths forward as landscapes and technologies inevitably continue to change.

ACKNOWLEDGEMENTS

Essentially, this dissertation exists thanks to my committee, who devised the original Team Laser project and brought me on board. Dr. Lee Vierling and Dr. Jan Eitel have both provided steady support, advice, and enthusiasm, and I especially appreciate the trust they showed in allowing me independence to disappear down deep research rabbit holes for long periods of time that might have worried less optimistic advisors. And despite their geographic remoteness, Dr. Natalie Boelman and Dr. Kevin Griffin have had an outsize influence on my research career – which is to say that they launched it, bringing me along to help with science in Alaska long before I ever considered pursuing a PhD. Since then, their insightful advice and comments have helped keep my research balanced and situated in the broader science community, and I'm only sorry that I don't get to enjoy their company more often. Collectively, my committee have presented an admirable example of professional camaraderie and supportive collaboration; every student should have such positive and understanding mentors.

Particular mentions are also owed to Team Laser members Dr. Troy Magney and Dr. Case Prager, for valuable research conversations and contextualization in addition to all the fun, and especially to Patrick Fekety, who seemed to actually enjoy our innumerable coffee-fueled hours discussing minute details of R and Python coding and the nuances of Random Forest modeling.

Financially, this dissertation exists thanks to NASA – specifically thanks to NASA Terrestrial Ecology grant NNX12AK83G awarded to Lee Vierling and the rest of my committee, and NASA Earth Science Fellowship NNX15AP04H awarded to myself. I am also grateful for a Graduate Research Supplemental Grant from the University of Idaho's College of Natural Resources that defrayed significant tuition costs. A fun and informative side project involving drone-based remote sensing was enabled by The Explorer's Club Exploration Fund Mamont Scholarship and Toolik Field Station, and I also benefitted from UI's GPSA Travel Awards enough times to be worth mentioning. Finally, sincere thanks are owed to the staff and general support of the UI College of Natural Resources and Toolik Field Station (University of Alaska Fairbanks).

DEDICATION

For my parents, Melanie Lynn Greaves and John Oliver Bernard Greaves (of course),
and for Patrick.

TABLE OF CONTENTS

Authorization to Submit Dissertation ii
Abstract iii
Acknowledgements iv
Dedication v
Table of Contents vi
List of Figures viii
List of Tables ix
Chapter 1: Estimating aboveground biomass and leaf area of low-stature Arctic shrubs with terrestrial LiDAR 1
Abstract 1
1. Introduction 1
2. Methods 5
3. Results 12
4. Discussion 17
Acknowledgements 21
References 21
Chapter 2: Applying terrestrial lidar for evaluation and calibration of airborne lidar-derived shrub biomass estimates in Arctic tundra 27
Abstract 27
1. Introduction 27
2. Methods 28
3. Results and Discussion 34
Acknowledgements 37
References 37
Supplemental Data 39
Chapter 3: High-resolution mapping of aboveground shrub biomass in Arctic tundra using airborne lidar and imagery 40
Abstract 40
1. Introduction 40
2. Methods 45

3. Results 53
4. Discussion 60
5. Conclusions 64
Acknowledgements 64
References 65
Chapter 4: Mapping Arctic tundra vegetation at sub-meter resolution with airborne lidar and multispectral imagery 71
Abstract 71
1. Introduction 71
2. Methods 72
3. Results and Discussion 80
Acknowledgements 95
References 95
Supplemental Data 100
Appendix A: Copyright permission from Elsevier 104
Appendix B: Copyright permission from Taylor & Francis 105

LIST OF FIGURES

Figure 1.1. Study area in northern Alaska, USA. 5
Figure 1.2. Schematic showing arrangement plots, subplots, and scan positions. 6
Figure 1.3. Photograph and point clouds showing one subplot. 8
Figure 1.4. Visualization of volumetric and voxel-counting approaches. 11
Figure 1.5. Optimization results. 13
Figure 1.6. Optimized regression relationships. 15
Figure 1.7. Leave-one-plot-out validation regressions. 16
Figure 1.8. Regression relationships for leaf mass, total mass, and leaf wet area. 17
Figure 2.1. Study area in northern Alaska. 29
Figure 2.2. Representative detail of TLS and ALS datasets. 30
Figure 2.3. Calibration training and test results: TLS-harvest. 34
Figure 2.4. Calibration training and test results: ALS-TLS, ALS-harvest. 35
Figure S2.1. Conceptual diagram showing processing relationships among datasets. 39
Figure 3.1. Location of study area in northern Alaska. 45
Figure 3.2. Example of complex tundra microtopography and absence of 'bare earth'. 49
Figure 3.3. Training and test results for shrub biomass derived from lidar canopy volume. 53
Figure 3.4. Random Forest regression results for models with different predictor sets. 56
Figure 3.5. A: Shrub biomass maps for the three lidar collection footprints. 58
Figure 3.6. Toolik shrub biomass estimates and coefficient of variation. 59
Figure 3.7. Histograms for the Toolik map. 60
Figure 3.8. Shrub biomass values with standard deviation and coefficient of variation. 60
Figure 4.1. Airborne data collection footprints. 73
Figure 4.2. Map of vegetation communities for the Toolik footprint shown at 1:25,000 scale. 89
Figure 4.3. 1:6500 scale detail of a well-known research area south of Toolik Field Station. 90
Figure 4.4. Map of vegetation communities for the Pipeline footprint shown at 1:19,500 scale. 91
Figure 4.5. 1:6500 scale detail of an area within the Pipeline footprint. 92
Figure 4.6. Map of vegetation communities for the Imnavait footprint shown at 1:17,500 scale. 93
Figure 4.7. 1:6500 scale detail of a well-known research area within the Imnavait footprint. 94

LIST OF TABLES

Table 1.1. Riegl VZ-400 technical specifications 6
Table 2.1. ALS and TLS instrument and collection specifications 31
Table 2.2. Values of processing parameters included in canopy volume optimization 32
Table 2.3. Strongest parameter sets for calibration of canopy volume to biomass 35
Table 3.1. Lidar collection specifications 46
Table 3.2. Input groups and variables included in Random Forest variable selection. 50
Table 3.3. Predictor sets included in Random Forest variable selection 52
Table 3.4. Percent of the time each predictor was selected for each Random Forest model 55
Table 4.1. Lidar collection specifications 74
Table 4.2. Random Forest vegetation classification input layers 77
Table 4.3. Final class names and counts for all reference data 79
Table 4.4. Confusion matrix and accuracy metrics including only withheld test plots 86
Table 4.5. Confusion matrix and accuracy metrics including all reference plots 87
Table S4.1. Crosswalk between original reference plot classification and final class names 100
Table S4.2. Weights matrix for calculating Cohens weighted kappa 101
Table S4.3. Fifteen most important Random Forest variables ranked per class 102

CHAPTER 1: ESTIMATING ABOVEGROUND BIOMASS AND LEAF AREA OF LOW-STATURE ARCTIC SHRUBS WITH TERRESTRIAL LIDAR

Greaves, H.E., Vierling, L.A., Eitel, J.U.H., Boelman, N.T., Magney, T.S., Prager, C.M., and Griffin, K.L. "Estimating aboveground biomass and leaf area of low-stature Arctic shrubs with terrestrial LiDAR". *Remote Sensing of Environment* (164), 2015, pp. 26-35.

Abstract

Arctic tundra ecosystems are responding to effects of climatic warming via shifts in vegetation composition and increased woody biomass. In this sensitive ecosystem, minor increases in woody plant biomass may induce significant changes in ecosystem structure and function. However, establishing methods for quantifying and potentially scaling woody plant biomass in low-stature biomes is challenging. In this study, we investigated the potential to use terrestrial laser scanning (TLS) to remotely estimate harvested biomass and leaf area of two dominant low-stature (<1.5 m tall) Arctic shrub species in 0.64 m^2 subplots established in northern Alaskan tundra. We explored two biomass estimation approaches (volumetric surface differencing and voxel counting) applied to point clouds obtained from close-range (2 m) and variable-range (~50 m) terrestrial laser scans. Relationships between harvested biomass and TLS metrics were strong for all combinations of approaches, with voxel counting giving a marginally better result than surface differencing for close-range data (R^2 = 0.94 vs 0.92; RMSE = 102 g vs 117 g) and surface differencing proving stronger than voxel counting for variable-range data (R^2 = 0.91 vs 0.82; RMSE = 119 g vs 169 g). Strong relationships between total harvested biomass and total leaf dry mass (R^2 = 0.93; RMSE = 13.4 g), and between leaf dry mass and leaf wet area (R^2 = 0.99; RMSE = 9.01 cm^2) justify estimation of shrub leaf area from TLS-derived shrub biomass. Our results show that rapidly acquired, repeatable terrestrial laser scans taken at multiple ranges can be processed using simple biomass estimation approaches to yield aboveground biomass and leaf area estimates for low-stature shrubs at fine spatial scales (sub-meter to ~50 meters) with the fidelity required to monitor small but ecologically meaningful changes in tundra structure. Further, these data may be employed as ground reference data for broader scale remote sensing data collection, such as airborne LiDAR scanning, that would enable shrub biomass and leaf-area estimates at fine spatial resolution over large spatial extents.

1. Introduction

The Arctic has undergone rapid climatic warming during recent decades (Hinzman et al., 2005), resulting in increased size, abundance, and range of deciduous shrubs in the treeless Arctic

tundra (Myers-Smith et al., 2011; Sturm et al., 2001). Substantial expansion of Arctic shrubs—especially dwarf birch (*Betula nana*), willow (*Salix* spp.), and alder (*Alnus viritis*)—would represent a fundamental transformation of the tundra ecosystem, with potential implications for carbon cycling (Mack et al., 2004; Sistla et al., 2013), permafrost dynamics (Blok et al., 2010; Walker et al., 2003), and fire regimes (Higuera et al., 2008), as well as wildlife habitat and trophic interactions (Rich et al., 2013; Tape et al., 2010). Accurate baseline maps of Arctic shrub biomass would facilitate the understanding and monitoring of these ongoing changes by permitting more accurate accounting of carbon pools and fluxes over space and time. In particular, methods are needed that can accurately quantify shrub biomass at fine spatial scales (sub-meter to ~100 m) to allow for high-fidelity ground-based monitoring of vegetation change over time, while also permitting the accurate translation and scalability of these measurements to landscape-level estimates. However, creating broad-extent maps that capture the fine biomass gradations and considerable spatial heterogeneity among low-stature tundra plant communities remains challenging (Beck et al., 2011; Selkowitz, 2010).

Accurate biomass measurements usually require destructive sampling, which is time-intensive, costly, impractical to perform at fine spatial resolution over large, remote areas like the Arctic tundra, and by definition prohibits repeat monitoring necessary to detect change (Mascaro et al., 2014). Consequently, satellite-based optical remote sensing techniques that rely on spectral vegetation indices such as the normalized difference vegetation index (NDVI; Tucker 1979) are frequently used in the Arctic tundra to estimate biomass (Boelman et al., 2003; Simms and Ward, 2013; Walker et al., 1995) and other plant community characteristics such as community structure (e.g., Boelman *et al.* 2011) and ecosystem carbon storage and fluxes (e.g., Street *et al.* 2007; Shaver *et al.* 2013). These studies have been useful for understanding multiyear trends in the greening or browning of the arctic; however, using satellite derived passive remote sensing techniques can be problematic because such indices can be strongly affected by factors like canopy architecture, viewing geometry, and the mixing of reflectance signals from plant leaves, woody stems, background soil, and surface water (Boelman et al., 2005; Gamon et al., 2013; Jackson and Huete, 1991; Jacquemoud and Baret, 1990; Verhoef, 1984). In the Arctic, these effects may be amplified by the small dimensions of Arctic tundra plants and their leaves (Vierling et al., 1997). Additionally, given the rapid progression of tundra plant phenology and the limited number of cloud-free satellite images that can be captured during the short (10-12 weeks) Arctic growing season, it can be difficult to obtain satellite data that passively capture spectral information at representative peak greenness (Boelman et al., 2011; Stow et al., 2004). Finally, although satellite-based spectral vegetation indices

have succeeded in distinguishing biomass differences between the tallest and shortest Arctic shrubs, it is currently difficult to remotely discern biomass differences within those extremes (Beck et al., 2011; Selkowitz, 2010). Yet these differences are of key importance to monitoring and understanding tundra plant communities and the wildlife that depend on them, especially given the potential for climate-change induced shifts in tundra plant community dominance (Myers-Smith *et al.* 2011 and references therein) and the effect such shifts could have on tundra biodiversity (Pajunen et al., 2011), wildlife (Rich et al., 2013; Tape et al., 2010), and carbon and nutrient cycling (Mack et al., 2004; Schimel et al., 2004).

Airborne laser scanning (ALS) is a LiDAR (Light Detection and Ranging) remote-sensing technique that may satisfy the need for tools that can distinguish fine gradations in vegetation height and density. ALS is well established in forestry research for characterizing three-dimensional (3D) variation in tree canopy structure (Lefsky et al., 2002), and has proven to be a highly accurate tool for estimating aboveground forest biomass, especially when complemented by additional data such as multispectral imaging (Zolkos et al., 2013 and references therein). Its successful application in the realm of forestry suggests that ALS holds great promise for biomass estimation in other biomes, including the Arctic tundra.

However, the use of ALS to map biomass in low-stature ecosystems like tundra is relatively understudied (Glenn et al., 2011; Mitchell et al., 2011; Riaño et al., 2007). The low areal laser return density (<5 points/m^2) and relatively large laser footprint (>30 cm diameter) characteristic of much ALS data collection can create a detection threshold that causes shrubs to be misclassified as ground, or underestimates shrub heights, especially where shrub structure is irregular or complex (Nyström et al., 2012; Riaño et al., 2007; Streutker and Glenn, 2006; Lee A Vierling et al., 2013). Advancements in the technology such as smaller laser footprints, higher laser return density, and the inclusion of auxiliary data like multispectral imagery is improving the accuracy of ALS biomass and height estimation (Mitchell et al., 2011; Reese et al., 2014; Zolkos et al., 2013), but there is still a need for tools that will allow researchers to rapidly and correctly calibrate ALS biomass estimates in low-stature ecosystems, and to quantify the error associated with those estimates.

Terrestrial laser scanning (TLS) is a ground-based LiDAR technique that may provide the valuable link between destructively harvested biomass samples and ALS biomass estimates. While ALS generally has a spatial accuracy of up to 5-10 cm (e.g., Streutker & Glenn 2006), TLS accuracy can be within millimeters—which is especially beneficial in low-stature ecosystems where a 5 cm error may represent 25% or more of average vegetation height. TLS has been used in numerous

ecological applications, including quantification of fuelbed characteristics (Loudermilk et al., 2009), tree canopy structure (Béland et al., 2011; Hopkinson et al., 2004; Michel et al., 2008; Moorthy et al., 2011), and shrub structure and biomass (Ku et al., 2012; Olsoy et al., 2014; Lee A Vierling et al., 2013). Laser return intensity information contained in TLS data has also been used to estimate both structural and physiological characteristics of plants, including chlorophyll content of broadleaf trees (Eitel et al., 2010), nitrogen content of crops (Eitel et al., 2014a, 2011), and photosynthetic downregulation of various plant species (Magney et al., 2014), as well as leaf area and leaf and woody area ratios of shrubs and conifers (Clawges et al., 2007; Olsoy et al., 2014).

Despite its widespread adoption for measurement of vegetation characteristics at fine scales (i.e. sub-centimeter accuracy at ranges of 1 to 100+ meters), there has been relatively little investigation into the potential use of TLS as a tool for validating and calibrating ALS low-stature vegetation quantification (Lee A Vierling et al., 2013). Hopkinson et al. (2013) used a histogram matching approach to calibrate ALS estimates of effective leaf area index in a forested system (including understory shrubs) against a waveform TLS system, but such approaches are still uncommon. This is partly because established methods relating ALS data to aboveground biomass (e.g., Estornell *et al.* 2012) generally rely on height percentile metrics that are confounded by the scan geometry and varying point density of TLS data, making these methods difficult to transfer to TLS datasets. As a next step, developing allometric equations and suitable, generalizable algorithms to relate destructively harvested biomass samples to TLS metrics could permit simple and accurate estimation of aboveground biomass at fine to moderate scales (1 to ~50 m). If relationships among aboveground biomass, leaf biomass, and leaf area are strong for the focal species or functional group, it may also be possible to indirectly derive vegetation leaf area from total estimated vegetation biomass. Pairing these allometric equations with relationships between TLS data and ALS data could allow further scaling up of not only aboveground low-stature vegetation biomass, but also of other vegetation properties, such as carbon and nitrogen content, that are critical to understanding ecosystem structure and function.

The objective of this study was to test the ability of TLS data to provide accurate biomass estimates for two dominant shrub species (dwarf birch [*Betula nana* L.] and diamond-leaf willow [*Salix pulchra* Cham.]) in small plots in the Arctic tundra. We investigated (1) the strength of relationships between destructively harvested shrub biomass and TLS-derived biomass estimates from multiple scan distance ranges; (2) the accuracy of two simple post-processing approaches (voxel counting and volumetric surface differencing) for deriving shrub biomass from TLS data; and

(3) the potential for using allometric relationships to estimate shrub leaf and woody biomass and leaf area from TLS-derived aboveground shrub biomass.

2. Methods

2.1. Study area

Field data were collected near Toolik Field Station (68°37'39" N, 149°35'51" W) at Toolik Lake, in the northern foothills of the Brooks Range in Alaska, USA (Figure 1.1). Mean precipitation at Toolik Lake is approximately 300 mm, with roughly half as snow. Summer temperatures average 10°C, and the growing season is short (~10-12 weeks), although the sun is above the horizon continuously for part of this time. The landscape consists mostly of rolling tussock-tundra hills underlain by permafrost and dominated by tussock cottongrass (*Eriophorum vaginatum* L.) and other sedges (mostly *Carex* spp.), with low-stature deciduous shrubs (especially *Betula nana* L. and *Salix* spp.) growing among the tussocks and dominating small water tracks. Cottongrass tussocks, moss hummocks, and glacial features such as kames create complex topography at fine (<1 m) to medium-fine (50 m) spatial scales. Taller shrubs (2-3 m) grow in more deeply thawed riparian zones, wet sedge fens and bogs lie in poorly drained areas, and dry heath communities occur on well-drained, wind-scoured knobs and ridges.

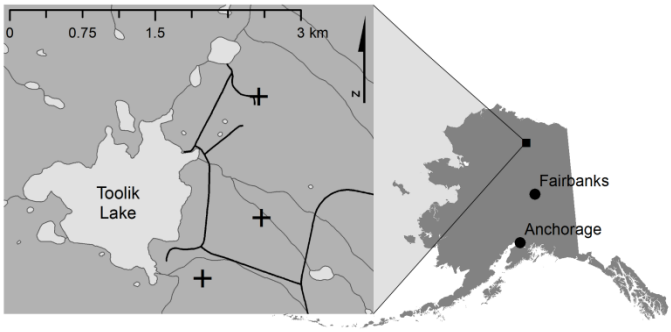

Figure 1.1. Study area in northern Alaska, USA. Crosses indicate location of terrestrial laser scanning plots.

2.2. Field data collection

In early summer 2013, we established twenty-four small (0.45 m-radius) subplots, which were divided among three larger (25 m-radius) circular field plots in settings that captured a variety of shrub morphology around Toolik Lake (Figure 1.1). Scans were conducted with a Riegl VZ-400 terrestrial laser scanner (RIEGL Laser Measurement Systems GmbH, Austria; hereafter referred to as the "TLS"). The Riegl VZ-400 employs a 1550 nm laser (Table 1.1) with onboard waveform processing that allows it to record multiple returns for each laser pulse. This reduces occlusion or "shadowing",

in which the first target encountered by a laser pulse prevents that pulse from reaching additional targets that may lie behind the first. Plot-level ("variable-range") TLS scans were performed from either four or five exterior scan positions surrounding each plot, depending on local terrain complexity, as well as from one position at the center of each plot, for a total of five or six variable-range scans per plot (Figure 1.2). Reflective targets were placed and scanned at each plot to permit subsequent co-registration of point clouds for both variable-range and close-range scans. The exterior scans were performed at a nominal point spacing of 1 cm at a distance of 30 m (angular step 0.3 milliradians). Central scans were coarser, with a nominal point spacing of 2 cm at 30 m (angular step 0.7 milliradians).

Table 1.1. Riegl VZ-400 technical specifications.

Wavelength	1550 nm
Field of view	100° vertical x 360° horizontal
Effective / maximum measurement rate	42 kHz / 122 kHz
Minimum / maximum nominal range	1.5 m / 600 m
Repeatability	3 mm
Beam divergence	0.35 mrad
Weight	9.6 kg

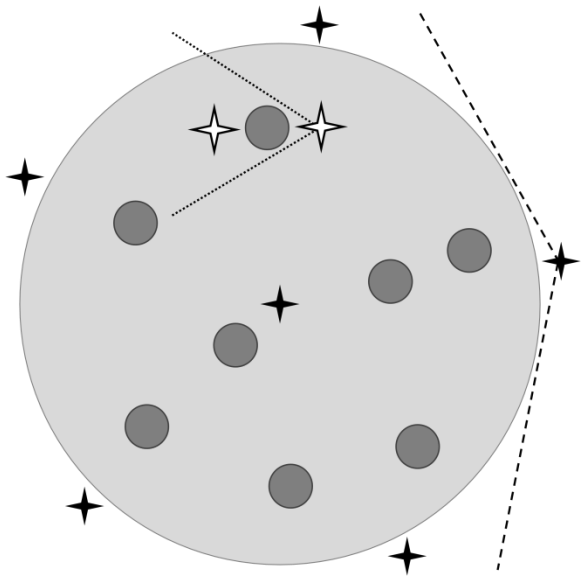

Figure 1.2. Schematic (not to scale) showing field arrangement of one 25 m-radius plot (pale grey) and eight 0.45 m-radius subplots (dark grey). Black stars show exterior and central (variable-range) scan positions; white stars show close-range scan positions for one subplot. Dashed lines bracket the potential scan coverage for one exterior scan position; dotted lines show potential scan coverage for one close-range scan.

Within each of these large plots, we subjectively situated eight 0.45 m-radius circular subplots, seeking to include individuals and collections of *Salix pulchra* and *Betula nana* that spanned a wide range of height and density that we visually determined was representative of those species in the area. To precisely capture vegetation structure, each of these twenty-four subplots and their immediate vicinity was scanned with the TLS from two opposing directions at a distance of ~2 m and a nominal point spacing of 1 mm at a distance of 2 m ("close-range"; angular step 0.5 milliradians). Subplots were placed without regard for the locations of the variable-range scan positions, and thus occurred at varying distances ("variable-range", ~2-50 m) from those positions.

Following close-range scans, shrubs were harvested from each subplot by identifying all *B. nana* and *S. pulchra* stems that originated within each subplot and clipping or sawing them off at the top of the moss layer. Harvested shrubs were transported from the field to the lab in closed plastic bags to help maintain leaf water content. To establish leaf dry mass-wet leaf area relationships, subsamples of approximately sixty leaves from each of the two focal species in nineteen subplots were separated from stems immediately on returning to the lab. These leaf subsamples were run through a leaf area meter (LI-3100, LI-COR Inc., Lincoln, Nebraska), then dried at 50°C for at least 48 hours and weighed. All other harvested material was dried at 50°C for at least 48 hours or until weight measurements stabilized. Once dry, leaf material was separated from stems, and leaf and stem dry mass were measured.

2.3. TLS pre-processing

For each of the twenty-four small subplots, we co-registered and merged the two opposing-direction close-range point clouds in RiScan Pro (RIEGL Laser Measurement Systems GmbH, Austria) to form a single close-range point cloud per subplot (Figure 1.3B). Each of the resulting twenty-four point clouds was subsequently clipped to a radius of 0.75 m. The clipping radius was larger than the original subplot radius in order to capture shrub stems and leaves that originated within the subplot but extended outside of it. The 0.75 m-radius subplot point clouds were then manually edited to remove the majority of "mosquito hits"—spurious points in midair occurring as a result of laser returns from plentiful airborne mosquitoes. The five or six variable-range scans covering each of the three large plots were also co-registered and merged using the software RiScan Pro to form a single point cloud per plot. The subplots were clipped from these variable-range point clouds following the same process as for close-range point clouds, using the same subplot center coordinates and 0.75 m radius used to clip the close-range point clouds (Figure 1.3C).

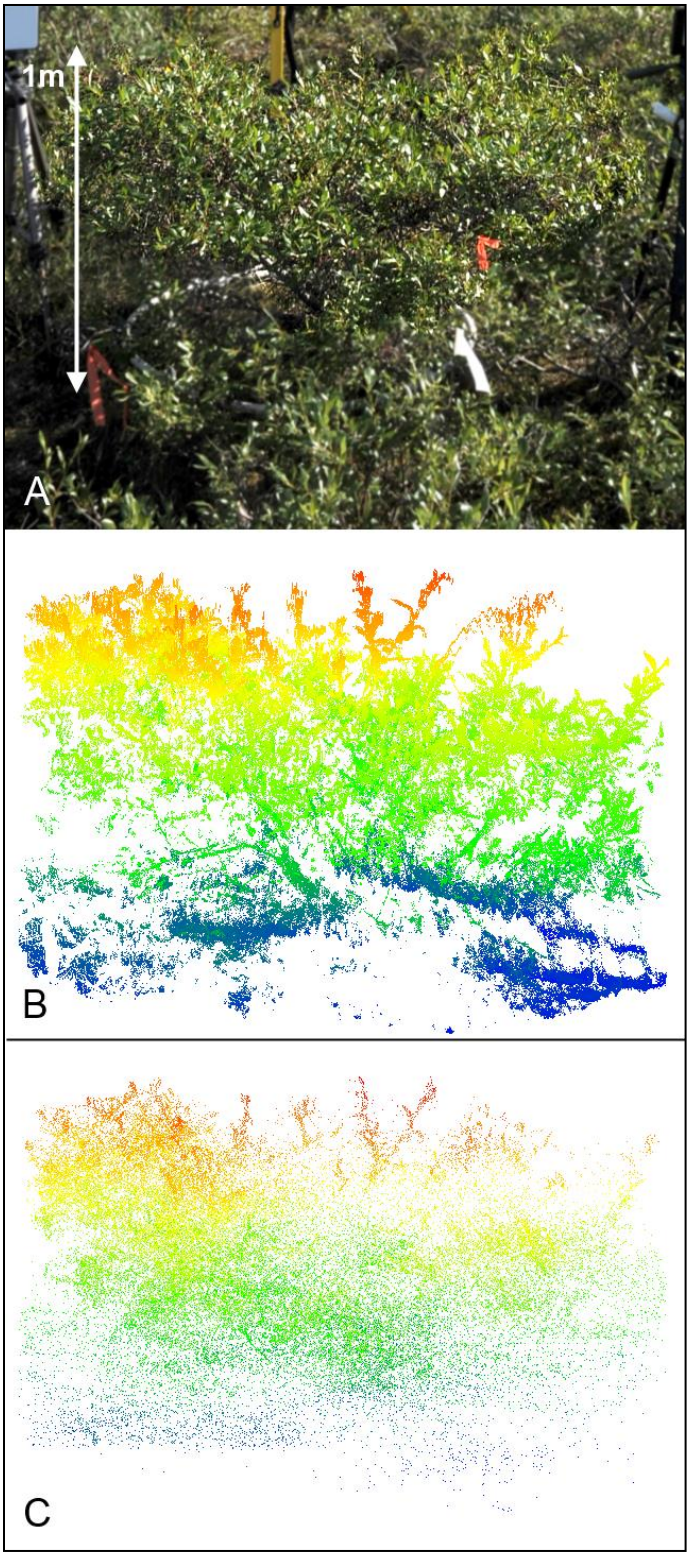

Figure 1.3. Photograph (A) and point clouds (B, C) showing one subplot (shrub biomass 1498 g). Point clouds were extracted from scans taken at close range (B; 2 m scan distance) and variable range (C; 2-50 m scan distance). Point cloud color indicates relative point height.

As part of the data recorded during a TLS scanning session, the Riegl VZ-400 includes a dimensionless quality metric for each point called the "deviation", which represents the probability that the point is an air return (also known as a ghost return or mixed-edge return) rather than a return from a real target (Pfennigbauer, 2010). This probability increases when a single laser pulse encounters multiple targets within a small distance range (less than about 0.50 m; Pfennigbauer, 2010), which occurs frequently within the dense branching structure of Arctic shrubs. Because of this complication, it was not apparent what deviation threshold value we should use to differentiate air returns from true target returns; therefore, we ran all analyses multiple times, varying the deviation threshold in steps of 2 between 2 and 80 (for close-range scans), and in steps of 20 up to 1000 (for variable-range scans) to identify the optimum deviation threshold value. Keeping only laser returns with a deviation less than the threshold value had the side effect of thinning the point clouds during processing.

2.4. Biomass estimation

We tested two approaches for deriving aboveground total shrub biomass from TLS point clouds: a voxel-counting approach, and a volumetric approach based on surface differencing. Voxel-based approaches usually increment biomass estimates based on how many voxels (i.e. cubic volumes of space, or 3D pixels) of a given size are occupied by laser returns, and such approaches have been applied successfully with TLS data to characterize vegetation characteristics including fuel bed volume (Loudermilk et al., 2009), leaf area distribution and density (Béland et al., 2011; Hosoi and Omasa, 2006), and sagebrush biomass (Olsoy et al., 2014). Volumetric methods such as surface differencing, surface modeling, and convex hull analysis have been used successfully in similar applications with broadly similar results (Eitel et al., 2014a; Keightley and Bawden, 2010; Loudermilk et al., 2009; Olsoy et al., 2014). Although both of these approaches can be applied with accurate results, they rely on different assumptions: while voxel-based methods tend to assume that no part of the target plant is occluded (i.e., the complete vegetation structure is visible to the TLS), volumetric methods assume that vegetation biomass is consistently related to vegetation volume. The appropriateness of these assumptions depends on the density and distribution of the target vegetation—for example, voxel-based assumptions of complete structural representation may not be appropriate in very dense vegetation where the TLS laser cannot penetrate, while the volumetric assumption of constant biomass density may be inappropriate in vegetation with irregularly distributed canopy gaps.

Because there is no prior example of either approach applied to Arctic shrub species, we compared versions of both approaches, using point clouds from both close-range and variable-range TLS scans. While close-range point clouds represented "best-possible" TLS datasets for very small (~1 m) areas, analyzing the coarser (2-50 meters) variable-range scans allowed us to determine how well relationships would hold, and which scanning (e.g., point spacing) and processing (e.g., deviation threshold) parameters might need to be changed, when applying our approaches to TLS point clouds with the irregular point spacing and frequent occlusion characteristic of variable-range TLS datasets.

2.4.1. Volumetric biomass estimation

The volumetric biomass estimation approach employed a program (available from the authors) written in the Interactive Data Language (IDL) software package (Version 8.0, ITT Visual Information Solutions) (Eitel et al., 2014a). This program used TLS subplot point clouds to create two 1 x 1 cm gridded surfaces for each subplot: a digital terrain model (DTM) representing the bare earth, and a digital canopy model (DCM) representing the top of the shrub canopy (Figure 1.4 left). The value assigned to each surface grid cell was determined by identifying the minimum (DTM) or maximum (DCM) height value within a search radius from the center of the grid cell, or by linear interpolation of neighboring grid cell values if no height value was found within the search radius. The optimal search radius for each surface was found empirically by varying the search radius between 1 and 20 cm in intervals of 1 cm. The volume of the point cloud was calculated as the difference between the DCM height and the DTM height at each grid cell multiplied by the area of the grid cell and summed over all grid cells.

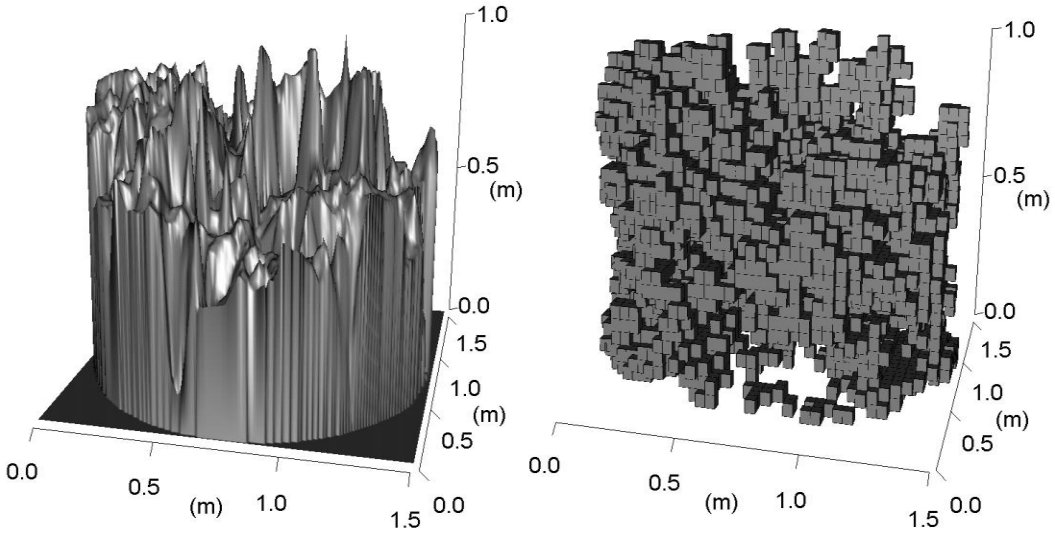

Figure 1.4. Visualization of the volumetric biomass estimation approach (left) and the voxel-counting approach (right). The same subplot as in Figure 1.3 is shown in both images.

2.4.2. Voxel-based biomass estimation

The voxel approach used a simple script (available from the authors) written in the open-source software package R version 3.0.1 (R Core Team 2014). In this script, the three-dimensional space of each subplot point cloud was divided into voxels. The script counted the number of voxels that were occupied by at least one laser return, and provided the number of occupied voxels per unit ground area (Figure 1.4 right). Using a similar technique as in our volumetric approach, the optimal voxel size was empirically determined for each analysis by varying the length of voxel edges between 1 and 20 cm in steps of 1 cm.

2.5. Statistical methods

Relationships between close-range and variable-range TLS point cloud metrics and harvested biomass measurements were evaluated in R, using simple linear regression to find the coefficient of determination (R^2) and root-mean-square error (RMSE) for each approach. The same method was used to determine the strength of relationships among total biomass, leaf biomass, and leaf area. To evaluate model performance, we calculated root mean square differences (RMSD; Stage and Crookston 2007) to quantify the deviation of each predicted value against the 1:1 line. For this, we performed a "leave-one-plot-out" regression analysis, in which the biomass for subplots in each of the three large plots was predicted using regression coefficients estimated from TLS-biomass relationships in the other two plots.

3. Results

Owing to different scan ranges and resolutions, subplot point clouds from close-range and variable-range scans had drastically differing numbers of laser returns. Prior to removing low-quality laser returns based on a deviation threshold, point clouds from close-range scans had an average of 30 times more points than variable-range point clouds (minimum of 9 times more; maximum of 104 times more), and based on visual examination, point distribution in close-range point clouds reflected actual branch and stem morphology more precisely than did variable-range point clouds (Figure 1.3).

3.1. Parameter optimization

3.1.1. Close-range parameter optimization

Three processing parameters were empirically optimized for the volumetric approach: deviation threshold, upper search radius (DCM creation), and lower search radius (DTM creation). For regressions using close-range point clouds (Figure 1.5A), the best R^2 and RMSE values were achieved using a deviation threshold of 20 and an upper and lower search radius both equal to 2 cm. Using a deviation threshold of 20 resulted in the removal of an average of 49% of points from subplot point clouds. Varying the upper search radius had the strongest effect on the resulting regression, with R^2 values decreasing steadily as the upper search radius increased from 1 to 16 cm; further increases had little effect. The model was less sensitive to changes in the lower search radius and the deviation, although the best R^2 values corresponded to lower search radii of 2-5 cm and deviation thresholds from 10 to 30. In general, the volumetric approach was robust to variations in processing parameters, with no R^2 values found below 0.70 in the ranges tested for the close-range point clouds.

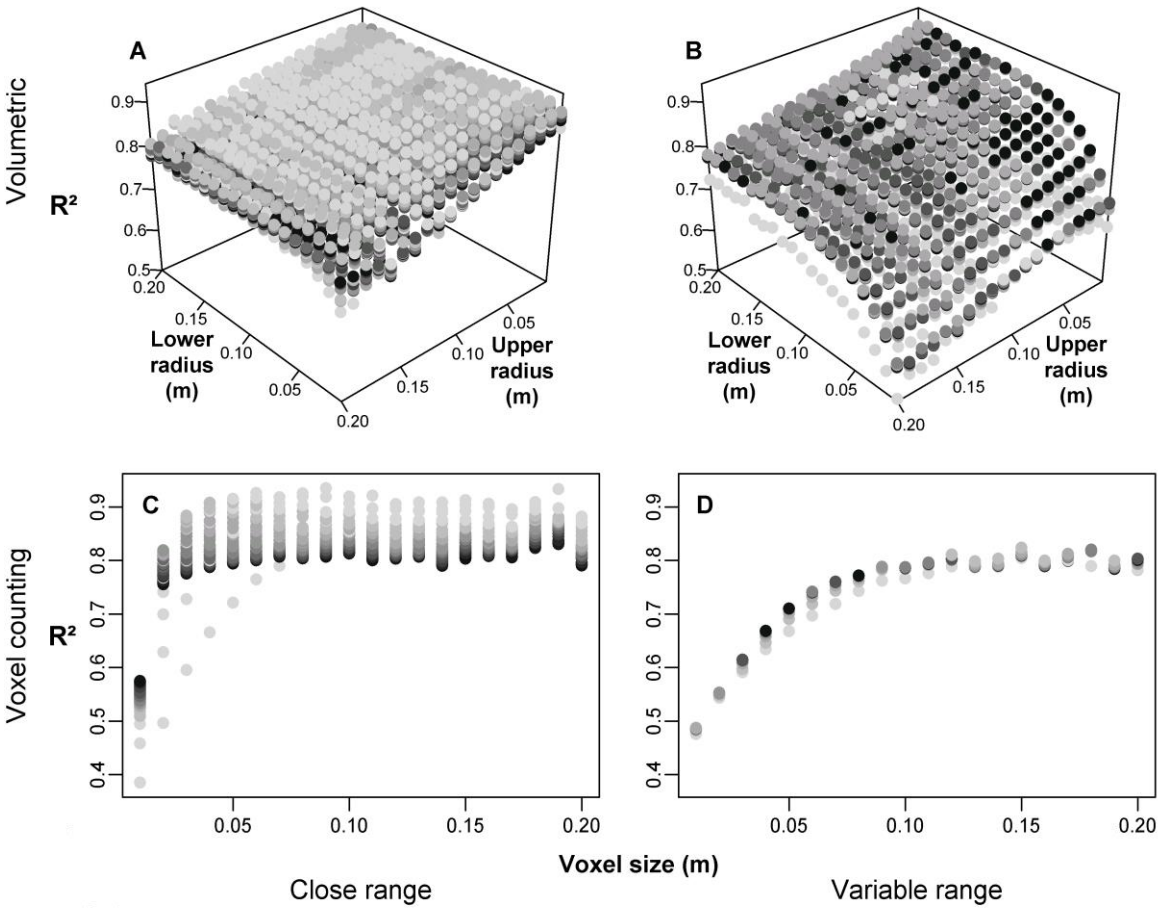

Figure 1.5. Optimization results. Top row: Response of biomass estimation R^2 to combinations of different upper and lower search radii and deviation thresholds in the volumetric approach using close-range (A) and variable-range data (B).Bottom row: Response of biomass estimation R^2 to combinations of voxel edge length and deviation threshold for the voxel-counting approach using close-range (C) and variable-range (D) data. Darker greys indicate higher deviation thresholds, ranging from 10-80 in steps of 5 (A and C) or from 100-500 in steps of 100 (B and D).

For the voxel approach, two processing parameters were optimized: deviation threshold and voxel size. The strongest close-range model used a deviation threshold of 4 with a voxel edge length of 9 cm (Figure 1.5C). A deviation threshold of 4 led to the removal of an average of 91% of points from subplot point clouds. Very small voxel sizes (1-2 cm) performed poorly regardless of deviation threshold, yielding model R^2 values as low as 0.38. The model was comparatively robust to variations in deviation threshold, although the best relationships were found with deviation thresholds of less than approximately 30.

3.1.2. Variable-range parameter optimization

For the volumetric approach using variable-range point clouds, regression results were strongest with small upper search radii; however, changing the lower search radius had a larger

impact on regression results (Figure 1.5B), which was not the case for close-range point clouds. Small lower search radii performed poorly, and R^2 values increased as the lower search radius increased from 1 cm to approximately 16 cm, then remained relatively constant. Optimized deviation thresholds were much higher for variable-range point clouds than for close-range point clouds. The best R^2 values were achieved with a lower search radius of 19 cm, an upper search radius of 1 cm, and a deviation maximum of 200. For the voxel approach, the best regression relationship was with a voxel size of 15 cm and a deviation threshold of 150 (Figure 1.5D).

3.2. Biomass estimation

3.2.1. Close-range biomass estimation

B. nana and *S. pulchra* samples were pooled for regression analysis, since preliminary analysis indicated that species was not a statistically significant predictor ($p > 0.40$). Relationships between harvested dry shrub biomass and TLS metrics were strong for both volumetric surface differencing and voxel-counting approaches using close-range scan data (Figure 1.6A and 1.6C). The voxel approach yielded a slightly higher coefficient of determination and lower RMSE ($R^2 = 0.94$ and RMSE = 102 g) than the volumetric approach ($R^2 = 0.92$ and RMSE = 117 g). A linear relationship provided the best fit for the volumetric approach, while a quadratic relationship fit best for the voxel approach. Regression error tended to increase with increasing biomass for both estimation approaches, although not in a linear fashion ($R^2 < 0.04$, $p > 0.18$).

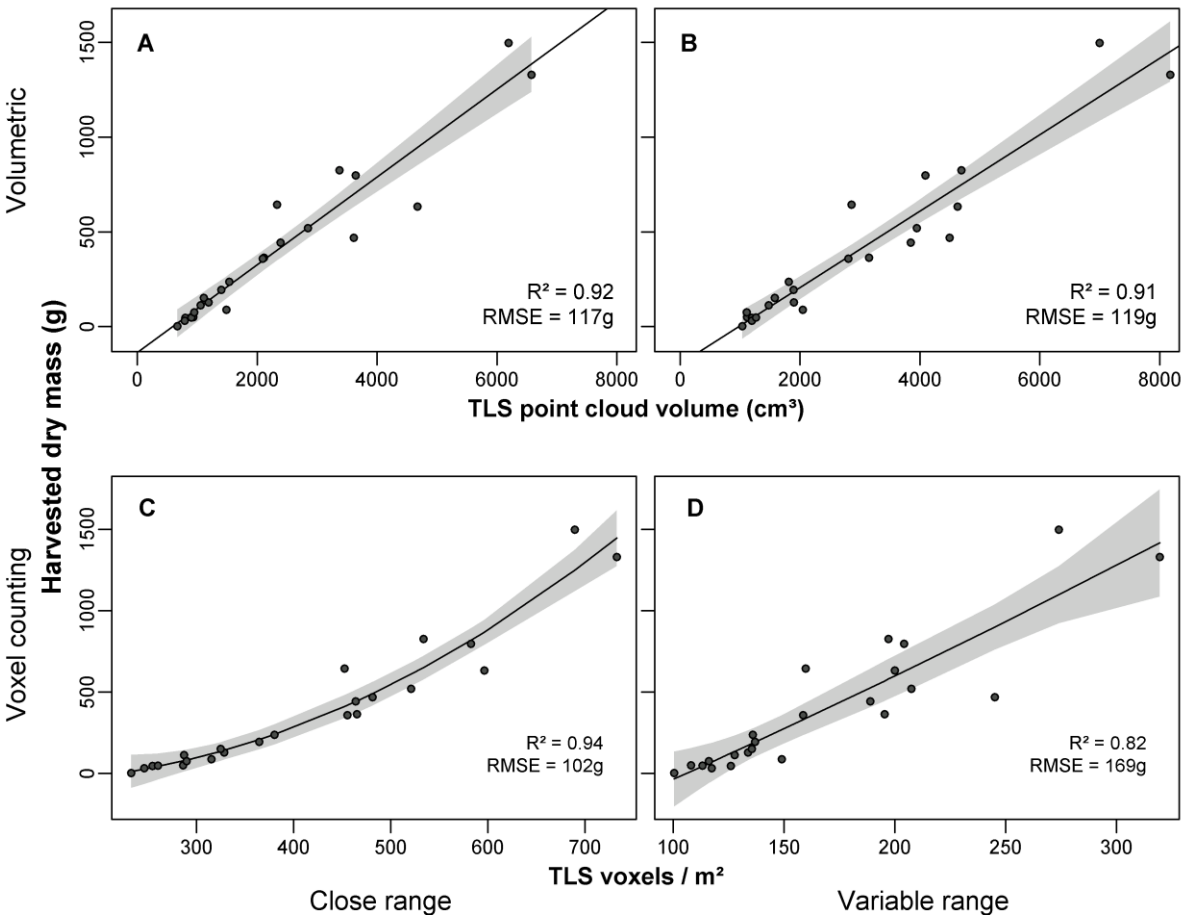

Figure 1.6. Optimized regression relationships between harvested biomass and TLS metrics for volumetric (top row) and voxel counting (bottom row) approaches, using data from close-range scans (left column) and variable-range scans (right column). Shaded areas are 95% confidence intervals.

3.2.2. Variable-range biomass estimation

Although biomass estimation results were similar for the volumetric and voxel approaches when applied to close-range point clouds, the volumetric approach outperformed the voxel approach when estimating shrub biomass from variable-range point clouds. Using variable-range point clouds, the best model R^2 was 0.91 with RMSE = 119 g for the volumetric approach (Figure 1.6B), compared to an R^2 of 0.82 and an RMSE of 169 g for the voxel approach (Figure 1.6D).

3.3. Close-range leave-one-plot-out analysis

In leave-one-plot-out volumetric analysis of close-range point clouds, biomass for subplots in each plot was well predicted from regression relationships established from subplots in the other two plots (Figure 1.7). None of the three regression intercepts differed significantly from zero ($p \geq$

0.38), and the 1:1 line fell on or within the 95% regression confidence envelope for all regressions, with the exception of Plot 1 for subplots with biomass greater than approximately 500 g.

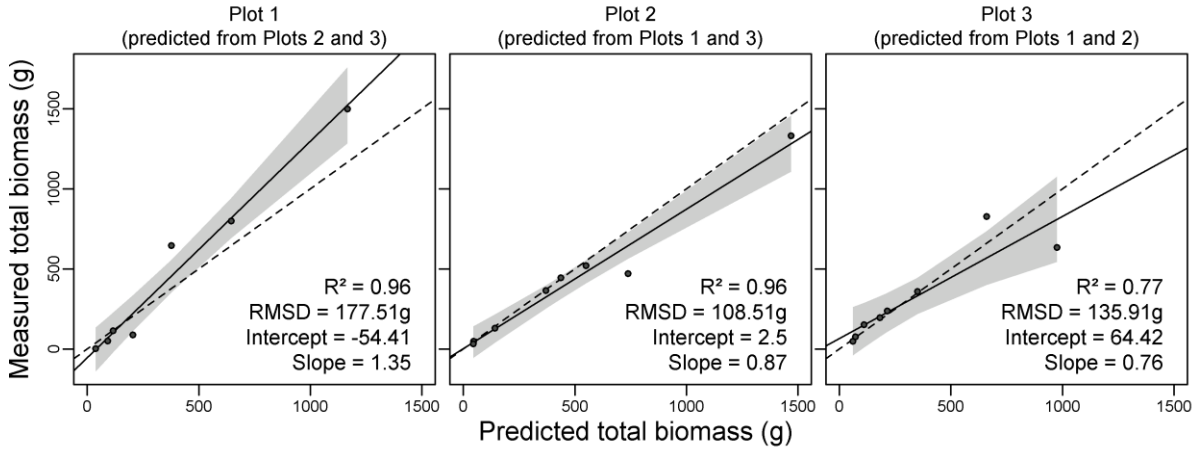

Figure 1.7. Leave-one-plot-out validation regressions. Solid line depicts regression fit; dashed line is 1:1 line. Shaded areas represent 95% regression confidence intervals.

3.4. Leaf mass and leaf area

Harvested leaf dry mass for *S. pulchra* and *B. nana* was strongly correlated with total aboveground harvested biomass (R^2 = 0.93, RMSE = 13.4 g; Figure 1.8). Because we found that species was not a significant predictor in the regression (p = 0.97), for this analysis all samples were pooled by subplot, regardless of species. Based on our laboratory analysis of a subset of leaves (with species again pooled by subplot), leaf dry mass was also highly correlated with leaf area (R^2 = 0.99, RMSE = 9.01 cm^2). In this case, species was a slightly significant predictor of the relationship between leaf mass and leaf area (p = 0.04), but we retained pooled results for consistency.

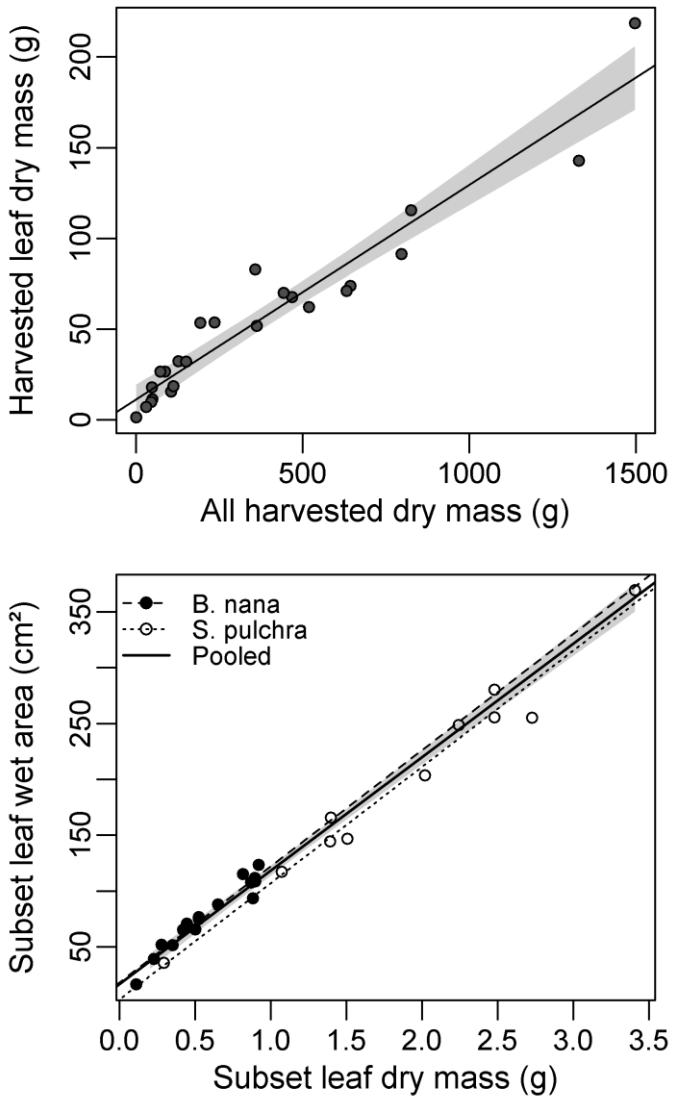

Figure 1.8. Top: Regression relationship between leaf dry biomass and total dry biomass in each plot. Shaded area indicates 95% confidence interval. Bottom: Regression relationships between leaf wet area and leaf dry mass for a subset of sampled leaves, showing relationship with species pooled (solid line) and separated (dashed and dotted lines). Shaded area indicates 95% confidence interval for pooled species regression.

4. Discussion

4.1. Biomass estimation

Our results show that TLS point clouds can be processed and calibrated with simple algorithms to yield highly accurate biomass estimates for two dominant, low-stature, deciduous shrub species in the Arctic tundra. The strength of the relationship between harvested biomass and TLS metrics derived from both our voxel and volumetric approaches indicates that non-destructive, TLS-based estimates of shrub biomass can be substituted for destructive sampling whenever

destructive sampling would be difficult, impractical, or impossible to conduct. Furthermore, owing to the strong relationships between total harvested biomass and total leaf dry mass (R^2 = 0.93; RMSE = 13.4 g), and between leaf dry mass and leaf wet area (R^2 = 0.99; RMSE = 9.01 cm^2), we found that TLS-derived shrub biomass estimates could also be used to non-destructively estimate shrub leaf mass and leaf area for these species.

Voxel-based and volumetric approaches both performed well, especially for close-range scans, and our results were comparable to results from previous studies linking TLS metrics to vegetation biomass (Ku et al., 2012; Lin et al., 2010; Olsoy et al., 2014; Lee A Vierling et al., 2013). For example, Ku et al. (2012) achieved R^2 values of 0.77-0.81 using TLS-derived height bins or percentile heights to estimate biomass of mesquite trees, which can have a shrub-like, multi-stemmed structure. Lin et al. (2010) related relative number of TLS returns to single-tree biomass with good results, although biomass proved more difficult to estimate for deciduous trees than for coniferous trees (R^2 = 0.88 vs. 0.97, respectively), potentially due to the occluding effect of large deciduous leaves. In our study, although leaves certainly occluded structure to some extent, the small dimensions (1-5 cm length) and relatively sparse distribution of *B. nana* and *S. pulchra* leaves probably limited occlusion and worked to our advantage.

For processing variable-range point clouds, which have sparser, more irregular point spacing, the volumetric approach proved considerably stronger than the voxel-counting approach, and nearly as strong as results obtained with close-range point clouds. This is encouraging for several reasons: first, it implies that a small number of co-registered variable-range TLS scans can be used to provide biomass estimates that are of similar quality to estimates obtained with a large number of close-range scans, which are more time-consuming to collect. It would also be fairly simple to use such data to calibrate optical remote sensing data at multiple scales, for example by scanning a 30 x 30 m area to relate to a Landsat pixel. Second, our results suggest that the volumetric surface-differencing biomass estimation method we employed is quite robust to variations in TLS scan range and point cloud quality. Third, the two essential point cloud features used in volumetric surface differencing are the top-of-canopy surface model (DCM) and the ground surface model (DTM), products that are easily obtainable from airborne laser scanning (ALS) datasets. This implies that despite differences between TLS and ALS data in scan angle, point density, and canopy penetration, volumetric surface differencing methods may transfer easily from TLS data to ALS data, at least in low-stature systems where the distribution of biomass density is comparatively uniform, and where the entire shrub is easily visible to a TLS. Indeed, volumetric

methods have shown promise for estimating aboveground biomass even in forested systems (Tao et al., 2014). Using the same biomass estimation approach to analyze both TLS and ALS data could greatly simplify the comparison and calibration of overlapping TLS and ALS datasets.

Although we show clear evidence that terrestrial LiDAR can be used to quantify aboveground shrub biomass in this ecosystem, a few limitations should be considered. For example, voxel-based biomass estimation methods, such as the voxel counting method used in this study, make intuitive sense as ways of relating patterns of points in 3D space to the biomass they represent; however, voxel methods are confounded by occlusion of targets, in which the first target encountered by a laser pulse prevents the laser from reaching additional targets that may lie behind the first. Effects of occlusion can be decreased by scanning a target from multiple directions (Van der Zande et al., 2008) or by employing a full-waveform LiDAR instrument (e.g., Zhao et al. 2011), but in dense vegetation the laser may still fail to fully penetrate the canopy, and the resulting point cloud may be a "shell" of the canopy rather than a complete representation. Without employing techniques such as ray-tracing, transmission ratio calculations, or point cloud modeling to compensate (Ashcroft et al., 2014; Béland et al., 2014, 2011; Bittner et al., 2012; Widlowski et al., 2014), this can result in weaker biomass estimates (Olsoy et al. 2014; voxel-based results from this study) but such mitigating strategies can be theoretically and computationally difficult, and could prove especially difficult to relate to ALS data.

On the other hand, while volumetric biomass estimation approaches account for the potentially un-scanned interior of a canopy, they instead assume that the biomass-per-volume of scanned vegetation is constant, regardless of species and size. Although this assumption also seems unappealing, the ability of our surface-differencing technique to accurately estimate a wide range of biomass across two species and multiple scan distances suggests that this may be a safe assumption in low-stature ecosystems, so long as relationships are sufficiently calibrated for the focal species or functional group. It is likely that with the advance of multi-wavelength laser technology, laser return intensity from multiple laser wavelengths could be used to improve biomass estimates by enhancing our ability to spectrally categorize surveyed objects into classes such as ground, rocks, vegetation species, and noise prior to biomass estimation (Brodu and Lague, 2012; Eitel et al., 2014b; Hartzell et al., 2014), which could greatly simplify the calibration process.

4.2. Implications of TLS processing and parameter optimization methods

The empirical optimization of multiple parameters in these analyses reflects the exploratory nature of the study, but also contributes to the growing pool of available information on TLS

processing for vegetation research. For example, in the optimization of the DTM ground surface creation during volume estimation, a much larger point search radius was required for variable-range point clouds (19 cm) than for close range point clouds (2 cm), likely reflecting the comparatively sparse distribution of ground-level points in variable-range point clouds. This indicates that additional variable-range scans may be required to compensate for increasing measurement distances, greater vegetation density, and terrain complexity (Glenn et al., 2011). Similarly, obtaining strong regression relationships with close-range scans required heavy deviation filtering of input point clouds, while variable-range point clouds required much lighter filtering. For future datasets, careful consideration and testing should be applied to identify the optimal processing parameters for a given scanner and target.

An additional consideration is the terrestrial laser scanner itself. In results for both of our close-range processing approaches, the best regression relationships were achieved with low deviation thresholds—20 for the volumetric approach and 4 for the voxel approach—which meant that large numbers of laser returns were eliminated during pre-processing. This suggests that for the Riegl VZ-400, the benefits of multiple returns may be counterbalanced by the comparatively large beam divergence, which leads to a large fraction of air returns (noise) in the raw data, at least for close-range scans. Analyses of point clouds acquired simultaneously using a Leica ScanStation2 TLS (single return 532 nm, <6 mm beam diameter; Leica Geosystems Inc., Heerbrugg, Switzerland) showed that comparable results can be achieved by applying the volumetric surface-differencing approach to data from a terrestrial laser scanner with a single return and a smaller beam diameter (data not shown). Alternatively, a TLS that returns the full waveform of the reflected laser pulse may be able to better resolve the complicated morphology of vegetation (Zhao et al., 2011).

4.3. Conclusions

This work has shown that biomass and leaf area of two dominant Arctic deciduous shrubs in small plots (1-50 m diameter) can be accurately estimated from TLS point clouds, whether point clouds were obtained at a uniform close range or composited from scans taken at multiple distances. Perhaps most importantly, our results suggest that TLS-derived shrub biomass may be confidently employed as ground reference data to calibrate biomass and leaf area estimates of these species from airborne laser scanning (ALS) campaigns that encompass a broader spatial extent, potentially improving the accuracy of shrub biomass mapping across the Arctic tundra and other remote areas and permitting a more nuanced understanding of aboveground carbon storage, biogeochemical cycling, fire potential, and wildlife habitat. Repeated TLS measurements of shrub

plots over time could also provide insight into climate-change-induced shrub expansion on the North Slope—especially if performed simultaneously with repeated ALS measurements—and allow future researchers to understand and predict potential changes in the trajectory of the Arctic ecosystem.

Acknowledgements

This work was supported by NASA Terrestrial Ecology grant NNX12AK83G and a NASA Idaho Space Grant Fellowship NNX10AM75H awarded to TSM. Riegl VZ-400 and accessories were provided by the UNAVCO Facility with support from NSF and NASA under NSF Cooperative Agreement No. EAR-0735156. The authors are extremely grateful for field and lab assistance from Moyo Ajayi and Rebecca Gibson, and for support from the staff and greater research community of Toolik Field Station, Institute of Arctic Biology, University of Alaska Fairbanks. This manuscript was greatly improved by comments from two anonymous reviewers.

References

Ashcroft, M. B., Gollan, J. R., & Ramp, D. (2014). Creating vegetation density profiles for a diverse range of ecological habitats using terrestrial laser scanning. Methods in Ecology and Evolution, 5(3), 263–272. doi:10.1111/2041-210X.12157

Beck, P. S. A., Horning, N., Goetz, S. J., Loranty, M. M., & Tape, K. D. (2011). Shrub cover on the North Slope of Alaska: a circa 2000 baseline map. Arctic, Antarctic, and Alpine Research, 43(3), 355–363. doi:10.1657/1938-4246-43.3.355

Béland, M., Baldocchi, D. D., Widlowski, J., Fournier, R. A., & Verstraete, M. M. (2014). On seeing the wood from the leaves and the role of voxel size in determining leaf area distribution of forests with terrestrial LiDAR. Agricultural and Forest Meteorology, 184, 82–97. doi:10.1016/j.agrformet.2013.09.005

Béland, M., Widlowski, J., Fournier, R. A., Côté, J., & Verstraete, M. M. (2011). Estimating leaf area distribution in savanna trees from terrestrial LiDAR measurements. Agricultural and Forest Meteorology, 151(9), 1252–1266. doi:10.1016/j.agrformet.2011.05.004

Bittner, S., Gayler, S., Biernath, C., Winkler, J. B., Seifert, S., Pretzsch, H., & Priesack, E. (2012). Evaluation of a ray-tracing canopy light model based on terrestrial laser scans. Canadian Journal of Remote Sensing, 38(05), 619–628. doi:10.5589/m12-050

Blok, D., Heijmans, M. M. P. D., Schaepman-Strub, G., Kononov, A. V., Maximov, T. C., & Berendse, F. (2010). Shrub expansion may reduce summer permafrost thaw in Siberian tundra. Global Change Biology, 16, 1296–1305. doi:10.1111/j.1365-2486.2009.02110.x

Boelman, N. T., Gough, L., McLaren, J. R., & Greaves, H. (2011). Does NDVI reflect variation in the structural attributes associated with increasing shrub dominance in arctic tundra? Environmental Research Letters, 6(3), 035501. doi:10.1088/1748-9326/6/3/035501

Boelman, N. T., Stieglitz, M., Griffin, K. L., & Shaver, G. R. (2005). Inter-annual variability of NDVI in response to long-term warming and fertilization in wet sedge and tussock tundra. Oecologia, 143(4), 588–97. doi:10.1007/s00442-005-0012-9

Boelman, N. T., Stieglitz, M., Rueth, H. M., Sommerkorn, M., Griffin, K. L., Shaver, G. R., & Gamon, J. A. (2003). Response of NDVI, biomass, and ecosystem gas exchange to long-term warming and fertilization in wet sedge tundra. Oecologia, 135(3), 414–21. doi:10.1007/s00442-003-1198-3

Brodu, N., & Lague, D. (2012). 3D terrestrial lidar data classification of complex natural scenes using a multi-scale dimensionality criterion: Applications in geomorphology. ISPRS Journal of Photogrammetry and Remote Sensing, 68, 121–134. doi:10.1016/j.isprsjprs.2012.01.006

Clawges, R., Vierling, L., Calhoon, M., & Toomey, M. (2007). Use of a ground-based scanning lidar for estimation of biophysical properties of western larch (Larix occidentalis). International Journal of Remote Sensing, 28(19), 4331–4344. doi:10.1080/01431160701243460

Eitel, J. U. H., Magney, T. S., Vierling, L. A., Brown, T. T., & Huggins, D. R. (2014). LiDAR based biomass and crop nitrogen estimates for rapid, non-destructive assessment of wheat nitrogen status. Field Crops Research, 159, 21–32. doi:10.1016/j.fcr.2014.01.008

Eitel, J. U. H., Magney, T. S., Vierling, L. A., & Dittmar, G. (2014). Assessment of crop foliar nitrogen using a novel dual-wavelength laser system and implications for conducting laser-based plant physiology. ISPRS Journal of Photogrammetry and Remote Sensing.

Eitel, J. U. H., Vierling, L. A., & Long, D. S. (2010). Simultaneous measurements of plant structure and chlorophyll content in broadleaf saplings with a terrestrial laser scanner. Remote Sensing of Environment, 114(10), 2229–2237. doi:10.1016/j.rse.2010.04.025

Eitel, J. U. H., Vierling, L. A., Long, D. S., & Hunt, E. R. (2011). Early season remote sensing of wheat nitrogen status using a green scanning laser. Agricultural and Forest Meteorology, 151(10), 1338–1345. doi:10.1016/j.agrformet.2011.05.015

Estornell, J., Ruiz, L. A., Velazquez-Marti, B., & Hermosilla, T. (2012). Estimation of biomass and volume of shrub vegetation using LiDAR and spectral data in a Mediterranean environment. Biomass and Bioenergy, 46, 710–721. doi:10.1016/j.biombioe.2012.06.023

Gamon, J. A., Huemmrich, K. F., Stone, R. S., & Tweedie, C. E. (2013). Spatial and temporal variation in primary productivity (NDVI) of coastal Alaskan tundra: Decreased vegetation growth following earlier snowmelt. Remote Sensing of Environment, 129, 144–153. doi:10.1016/j.rse.2012.10.030

Glenn, N. F., Spaete, L. P., Sankey, T. T., Derryberry, D. R., Hardegree, S. P., & Mitchell, J. J. (2011). Errors in LiDAR-derived shrub height and crown area on sloped terrain. Journal of Arid Environments, 75(4), 377–382. doi:10.1016/j.jaridenv.2010.11.005

Hartzell, P., Glennie, C., Biber, K., & Khan, S. (2014). Application of multispectral LiDAR to automated virtual outcrop geology. ISPRS Journal of Photogrammetry and Remote Sensing, 88, 147–155. doi:10.1016/j.isprsjprs.2013.12.004

Higuera, P. E., Brubaker, L. B., Anderson, P. M., Brown, T. A., Kennedy, A. T., & Hu, F. S. (2008). Frequent fires in ancient shrub tundra: implications of paleorecords for arctic environmental change. PloS One, 3(3), e0001744. doi:10.1371/journal.pone.0001744

Hinzman, L. D., Bettez, N. D., Bolton, W. R., Chapin, F. S., Dyurgerov, M. B., Fastie, C. L., … Yoshikawa, K. (2005). Evidence and implications of recent climate change in northern Alaska and other Arctic regions. Climatic Change, 72(3), 251–298. doi:10.1007/s10584-005-5352-2

Hopkinson, C., Chasmer, L., Young-Pow, C., & Treitz, P. (2004). Assessing forest metrics with a ground-based scanning lidar, 583, 573–583. doi:10.1139/X03-225

Hopkinson, C., Lovell, J., Chasmer, L., Jupp, D., Kljun, N., & van Gorsel, E. (2013). Integrating terrestrial and airborne lidar to calibrate a 3D canopy model of effective leaf area index. Remote Sensing of Environment, 136, 301–314. doi:10.1016/j.rse.2013.05.012

Hosoi, F., & Omasa, K. (2006). Voxel-based 3-D modeling of individual trees for estimating leaf area density using high-resolution portable scanning lidar. IEEE Transactions on Geoscience and Remote Sensing, 44(12), 3610–3618.

Jackson, R. D., & Huete, A. R. (1991). Interpreting vegetation indices. Preventative Veterinary Medicine, 11, 185–200.

Jacquemoud, S., & Baret, F. (1990). PROSPECT: A model of leaf optical properties spectra. Remote Sensing of Environment, 34(2), 75–91. doi:10.1016/0034-4257(90)90100-Z

Keightley, K. E., & Bawden, G. W. (2010). 3D volumetric modeling of grapevine biomass using Tripod LiDAR. Computers and Electronics in Agriculture, 74(2), 305–312. doi:10.1016/j.compag.2010.09.005

Ku, N., Popescu, S. C., Ansley, R. J., Perotto-Baldivieso, H. L., & Filippi, A. M. (2012). Assessment of available rangeland woody plant biomass with a terrestrial lidar system. Photogrammetric Engineering and Remote Sensing, 78(4), 349–361.

Lefsky, M. A., Cohen, W. B., Parker, G. G., & Harding, D. J. (2002). Lidar remote sensing for ecosystem studies. BioScience, 52(1), 19. doi:10.1641/0006-3568(2002)052[0019:LRSFES]2.0.CO;2

Lin, Y., Jaakkola, A., Hyyppä, J., & Kaartinen, H. (2010). From TLS to VLS: biomass estimation at individual tree level. Remote Sensing, 2(8), 1864–1879. doi:10.3390/rs2081864

Loudermilk, E. L., Hiers, J. K., O'Brien, J. J., Mitchell, R. J., Singhania, A., Fernandez, J. C., … Slatton, K. C. (2009). Ground-based LIDAR : a novel approach to quantify fine-scale fuelbed characteristics. International Journal of Wildland Fire, 18, 676–685.

Mack, M. C., Schuur, E. A. G., Bret-Harte, M. S., Shaver, G. R., & Chapin, F. S. (2004). Ecosystem carbon storage in arctic tundra reduced by long-term nutrient fertilization. Nature, 431(7007), 440–3. doi:10.1038/nature02887

Magney, T. S., Eusden, S. A., Eitel, J. U. H., Logan, B. A., Jiang, J., & Vierling, L. A. (2014). Assessing leaf photoprotective mechanisms using terrestrial LiDAR: towards mapping canopy photosynthetic performance in three dimensions. New Phytologist, 201(1), 344–356.

Mascaro, J., Asner, G. P., Davies, S., Dehgan, A., & Saatchi, S. (2014). These are the days of lasers in the jungle. Carbon Balance and Management, 9(1), 7. doi:10.1186/s13021-014-0007-0

Michel, P., Jenkins, J., Mason, N., Dickinson, K. J. M., & Jamieson, I. G. (2008). Assessing the ecological application of lasergrammetric techniques to measure fine-scale vegetation structure. Ecological Informatics, 3(4-5), 309–320. doi:10.1016/j.ecoinf.2008.07.002

Mitchell, J. J., Glenn, N. F., Sankey, T. T., Derryberry, D. R., Anderson, M. O., & Hruska, R. C. (2011). Small-footprint lidar estimations of sagebrush canopy characteristics. Photogrammetric Engineering and Remote Sensing, 77(5), 1–10.

Moorthy, I., Miller, J. R., Berni, J. A. J., Zarco-Tejada, P., Hu, B., & Chen, J. (2011). Field characterization of olive (Olea europaea L.) tree crown architecture using terrestrial laser scanning data. Agricultural and Forest Meteorology, 151(2), 204–214. doi:10.1016/j.agrformet.2010.10.005

Myers-Smith, I. H., Forbes, B. C., Wilmking, M., Hallinger, M., Lantz, T., Blok, D., … Hik, D. S. (2011). Shrub expansion in tundra ecosystems: dynamics, impacts and research priorities. Environmental Research Letters, 6(4). doi:10.1088/1748-9326/6/4/045509

Nyström, M., Holmgren, J., & Olsson, H. (2012). Prediction of tree biomass in the forest-tundra ecotone using airborne laser scanning. Remote Sensing of Environment, 123, 271–279. doi:10.1016/j.rse.2012.03.008

Olsoy, P. J., Glenn, N. F., Clark, P. E., & Derryberry, D. R. (2014). Aboveground total and green biomass of dryland shrub derived from terrestrial laser scanning. ISPRS Journal of Photogrammetry and Remote Sensing, 88, 166–173. doi:10.1016/j.isprsjprs.2013.12.006

Pajunen, A. M., Oksanen, J., & Virtanen, R. (2011). Impact of shrub canopies on understorey vegetation in western Eurasian tundra. Journal of Vegetation Science, 22(5), 837–846. doi:10.1111/j.1654-1103.2011.01285.x

Pfennigbauer, M. (2010). Improving quality of laser scanning data acquisition through calibrated amplitude and pulse deviation measurement. Proceedings of SPIE, 7684, 76841F–76841F–10.

R Core Team. 2015. “R: A Language and Environment for Statistical Computing.” R Foundation for Statistical Computing. Vienna, Austria. URL http://www.R-Project.org/. http://www.r-project.org.

Reese, H., Nyström, M., Nordkvist, K., & Olsson, H. (2014). Combining airborne laser scanning data and optical satellite data for classification of alpine vegetation. International Journal of Applied Earth Observation and Geoinformation, 27, 81–90. doi:10.1016/j.jag.2013.05.003

Riaño, D., Chuvieco, E., Ustin, S. L., Salas, J., Rodríguez-Pérez, J. R., Ribeiro, L. M., … Fernández, H. (2007). Estimation of shrub height for fuel-type mapping combining airborne LiDAR and simultaneous color infrared ortho imaging. International Journal of Wildland Fire, 16(3), 341. doi:10.1071/WF06003

Rich, M. E., Gough, L., & Boelman, N. T. (2013). Arctic arthropod assemblages in habitats of differing shrub dominance. Ecography, 36(December 2012). doi:10.1111/j.1600-0587.2012.00078.x

Schimel, J. P., Bilbrough, C., & Welker, J. M. (2004). Increased snow depth affects microbial activity and nitrogen mineralization in two Arctic tundra communities. Soil Biology and Biochemistry, 36(2), 217–227. doi:10.1016/j.soilbio.2003.09.008

Selkowitz, D. J. (2010). A comparison of multi-spectral, multi-angular, and multi-temporal remote sensing datasets for fractional shrub canopy mapping in Arctic Alaska. Remote Sensing of Environment, 114(7), 1338–1352. doi:10.1016/j.rse.2010.01.012

Shaver, G. R., Rastetter, E. B., Salmon, V., Street, L. E., van de Weg, M. J., Rocha, A., … Williams, M. (2013). Pan-Arctic modelling of net ecosystem exchange of CO2. Philosophical Transactions of the Royal Society B-Biological Sciences, 368(1624).

Simms, É., & Ward, H. (2013). Multisensor NDVI-based monitoring of the tundra-taiga interface (Mealy Mountains, Labrador, Canada). Remote Sensing, 5(3), 1066–1090. doi:10.3390/rs5031066

Sistla, S. A., Moore, J. C., Simpson, R. T., Gough, L., Shaver, G. R., & Schimel, J. P. (2013). Long-term warming restructures Arctic tundra without changing net soil carbon storage. Nature, 1–5. doi:10.1038/nature12129

Stage, A. R., & Crookston, N. L. (2007). Partitioning error components for accuracy-assessment of near-neighbor methods of imputation. Forest Science, 53(1).

Stow, D. A., Hope, A., McGuire, D., Verbyla, D., Gamon, J., Huemmrich, F., … Myneni, R. (2004). Remote sensing of vegetation and land-cover change in Arctic Tundra Ecosystems. Remote Sensing of Environment, 89(3), 281–308. doi:10.1016/j.rse.2003.10.018

Street, L. E., Shaver, G. R., Williams, M., & Van Wijk, M. T. (2007). What is the relationship between changes in canopy leaf area and changes in photosynthetic CO2 flux in arctic ecosystems? Journal of Ecology, 95(1), 139–150. doi:10.1111/j.1365-2745.2006.01187.x

Streutker, D. R., & Glenn, N. F. (2006). LiDAR measurement of sagebrush steppe vegetation heights. Remote Sensing of Environment, 102(1-2), 135–145. doi:10.1016/j.rse.2006.02.011

Sturm, M., Racine, C., Tape, K., Cronin, T. W., Caldwell, R. L., & Marshall, J. (2001). Increasing shrub abundance in the Arctic. Nature, 411(May), 2001–2002.

Tao, S., Guo, Q., Li, L., Xue, B., Kelly, M., Li, W., … Su, Y. (2014). Airborne Lidar-derived volume metrics for aboveground biomass estimation: A comparative assessment for conifer stands. Agricultural and Forest Meteorology, 198-199, 24–32. doi:10.1016/j.agrformet.2014.07.008

Tape, K. D., Lord, R., Marshall, H. P., & Ruess, R. W. (2010). Snow-mediated ptarmigan browsing and shrub expansion in Arctic Alaska. Ecoscience, 17(2), 186–193. doi:10.2980/17-2-3323

Tucker, C. (1979). Red and photographic infrared linear combinations for monitoring vegetation. Remote Sensing of Environment, 8(2), 127–150.

Van der Zande, D., Jonckheere, I., Stuckens, J., Verstraeten, W. W., & Coppin, P. (2008). Sampling design of ground-based lidar measurements of forest canopy structure and its effect on shadowing. Canadian Journal of Remote Sensing, 34(6), 526–538.

Verhoef, W. (1984). Light-scattering by leaf layers with application to canopy reflectance modeling - the SAIL model. Remote Sensing of Environment, 16(2), 125–141.

Vierling, L. A., Deering, D. W., & Eck, T. F. (1997). Differences in Arctic tundra vegetation type and phenology as seen using bidirectional radiometry in the early growing season. Remote Sensing of Environment, 4257(96), 71–82.

Vierling, L. A., Xu, Y., Eitel, J. U. H., & Oldow, J. S. (2012). Shrub characterization using terrestrial laser scanning and implications for airborne LiDAR assessment. Canadian Journal of Remote Sensing, 38(6), 709–722.

Walker, D. A., Auerbach, N. A., & Shippert, M. M. (1995). NDVI, biomass, and landscape evolution of glaciated terrain in northern Alaska. Polar Record, 31(177), 169–178.

Walker, D. A., Jia, G. J., Epstein, H. E., Raynolds, M. K., Chapin, F. S. I., Copass, C., … Romanovsky, V. E. (2003). Vegetation-soil-thaw-depth relationships along a low-Arctic bioclimate gradient , Alaska: synthesis of information from the ATLAS studies. Permafrost and Periglacial Processes, 14(April), 103–123. doi:10.1002/ppp.452

Widlowski, J., Côté, J., & Béland, M. (2014). Abstract tree crowns in 3D radiative transfer models: Impact on simulated open-canopy reflectances. Remote Sensing of Environment, 142, 155–175. doi:10.1016/j.rse.2013.11.016

Zhao, F., Yang, X., Schull, M. A., Román-Colón, M. O., Yao, T., Wang, Z., … Strahler, A. H. (2011). Measuring effective leaf area index, foliage profile, and stand height in New England forest stands using a full-waveform ground-based lidar. Remote Sensing of Environment, 115(11), 2954–2964. doi:10.1016/j.rse.2010.08.030

Zolkos, S. G., Goetz, S. J., & Dubayah, R. (2013). A meta-analysis of terrestrial aboveground biomass estimation using lidar remote sensing. Remote Sensing of Environment, 128, 289–298. doi:10.1016/j.rse.2012.10.017

CHAPTER 2: APPLYING TERRESTRIAL LIDAR FOR EVALUATION AND CALIBRATION OF AIRBORNE LIDAR-DERIVED SHRUB BIOMASS ESTIMATES IN ARCTIC TUNDRA

Greaves, H.E., Vierling, L.A., Eitel, J.U.H., Boelman, N.T., Magney, T.S., Prager, C.M., and Griffin, K.L. "Applying terrestrial lidar for evaluation and calibration of airborne lidar-derived shrub biomass estimates in Arctic tundra". *Remote Sensing Letters* (8:2), 2017, pp. 175-184.

Abstract

Monitoring of climate-driven expansion of low-stature shrubs in Arctic tundra can be improved through application of high-resolution remote sensing. However, the destructive nature of harvest sampling that is usually performed for validation of these data is resource intensive and can limit future comparisons by destroying benchmark measurements. We compared aboveground shrub biomass estimates derived from terrestrial laser scanning (TLS) and airborne laser scanning (ALS) with the goal of determining whether TLS data can be used to accurately calibrate ALS estimates of shrub biomass in Arctic tundra. We used a leave-one-out cross-validation calibration of canopy volume against harvested shrub biomass to establish predictive relationships between TLS canopy volume and harvested shrub biomass, and between ALS canopy volume and TLS-derived shrub biomass estimates. TLS produced more accurate predictions of shrub biomass (R^2 = 0.78; root mean square deviation [RMSD] = 102 g) than did ALS, but the accuracy of ALS-derived shrub biomass predictions was the same whether they were calibrated directly against harvest biomass or against TLS-derived estimates of biomass (R^2 = 0.62; RMSD = 140 g). Our results suggest that once the initial TLS-harvest relationship is known, TLS can provide valid ground reference data for calibration of ALS-derived estimates of shrub biomass without the need for additional destructive harvest.

1. Introduction

Across the Arctic tundra, deciduous shrubs are expanding in response to rapid climatic warming, with ramifications for the entire ecosystem (Myers-Smith et al., 2011). However, quantifying baseline vegetation to permit change detection at a scale relevant to the stature and heterogeneity of tundra vegetation communities is challenging (Selkowitz, 2010). Airborne lidar (i.e. airborne laser scanning or ALS) provides three-dimensional (3D) vegetation structural data at high resolution (1-30+ points/m^2) that could be valuable for identifying changes in tundra vegetation structure, although such datasets are still rare in Arctic tundra regions (Greaves et al., 2016; Jones et al., 2013).

Traditionally, ALS data are calibrated against field data for estimation of vegetation traits like aboveground biomass. For biomass calibration, destructive harvesting is a simple calibration method (e.g. Olsoy et al. 2014), but destructive harvesting precludes multitemporal sampling—an especially important consideration in change-detection studies. Terrestrial lidar, or terrestrial laser scanning (TLS), provides a potential alternative solution for calibration of ALS data. TLS has been used in forested systems to improve ALS estimates of understory vegetation characteristics and leaf area (Hilker et al., 2010; Hopkinson et al., 2013), while in a dryland shrub system, Li et al. (2015) showed that TLS data could be used in a hierarchical scaling framework to improve sagebrush biomass estimates derived from relatively sparse (5 points/m^2) ALS data. The tripod-mounted viewpoint of TLS makes it especially useful for identifying shrubs (Lee A Vierling et al., 2013) and estimating shrub biomass (Olsoy et al., 2014). Previous work (Greaves et al., 2015) has shown that TLS-derived canopy volume, which incorporates both horizontal and vertical aspects of vegetation canopy structure, provides a robust proxy for shrub biomass in Arctic tundra.

By developing known relationships between TLS-derived canopy volume and tundra shrub biomass, TLS-to-ALS calibration could permit repeated estimates of tundra vegetation canopy volume and shrub biomass based on rapid TLS data collection without destructive harvest. Our objective was to quantify the accuracy of ALS-derived shrub biomass estimates when calibrated against TLS-derived shrub biomass estimates. We also compare the accuracy of these TLS-calibrated shrub biomass estimates to ALS estimates calibrated directly against harvest data, using the same calibration procedure.

2. Methods

2.1. Study area

Data were collected near Toolik Lake (68°38’ N, 149°36’ W) in the northern foothills of the Brooks Range, Alaska, USA (Figure 2.1). The landscape is topographically complex and underlain by continuous permafrost, with broad hillslopes of tussock tundra dominated by tussock cottongrass (*Eriophorum vaginatum* L.) and other sedges (especially *Carex* spp.) and mosses (especially *Sphagnum* spp.), along with low-stature (generally <1 m) deciduous shrubs (e.g. *Betula nana* L. and *Salix* spp.). Growing-season temperatures average 10°C and mean precipitation is approximately 300 mm, half of which falls as winter snow.

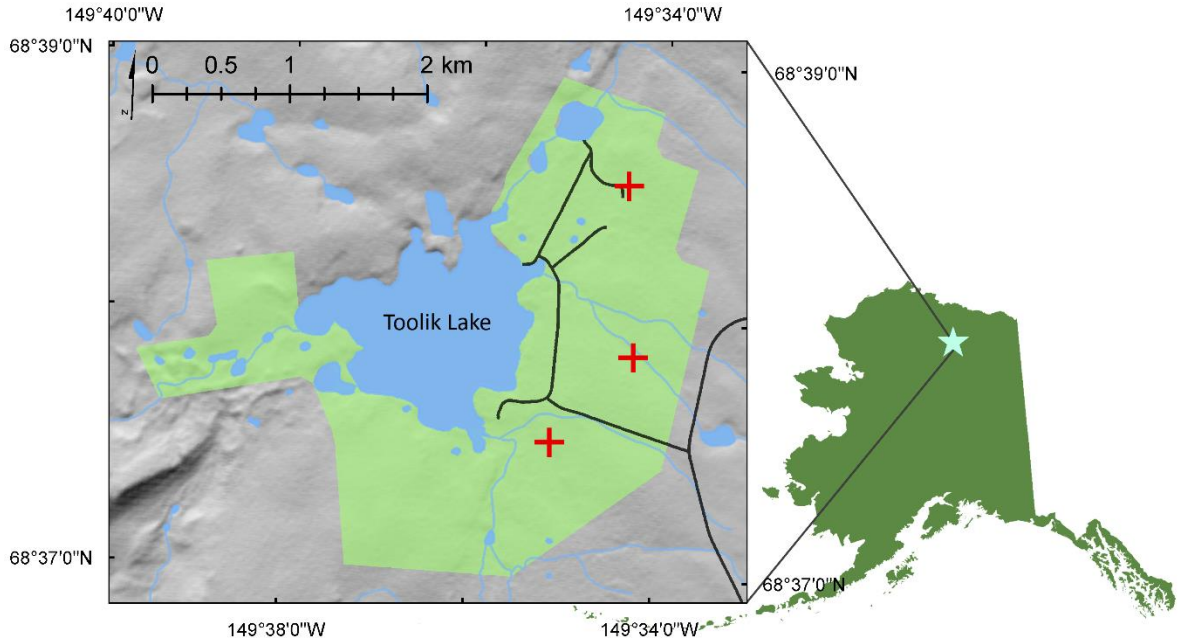

Figure 2.1. Study area in northern Alaska. Detail map shows airborne laser scanning (ALS) collection footprint in pale green. Red crosses indicate locations of the three terrestrial laser scanning (TLS) plots within the western ALS footprint.

2.2. Data collection

2.2.1. Airborne lidar collection

ALS data were collected August 1st, 2013 using a Riegl VQ-480i sensor mounted on a small aircraft (Figure 2.1; see Table 2.1 for instrument and collection specifications). Nominal return density was 13.5 points/m^2, and flight lines were 60% overlapped to achieve an average final density of 27 points/m^2. The commercial lidar vendor performed standard pre-processing of the airborne lidar data, including ground control georectification and aircraft attitude adjustments. We included all return numbers, return intensities, and scan angles in analyses.

2.2.2. Terrestrial lidar collection

In July 2013, we established three circular 25 m radius TLS field plots within the ALS collection footprint (Figure 2.1; see Table 2.1 for TLS instrument and collection specifications). Plot 1 was near the foot of a small stream/watertrack on a shallow west-facing hillslope; Plot 2 was situated adjacent to a larger valley-bottom watertrack on a relatively protected north-facing slope; Plot 3 was located on a drier and more exposed south-facing shelf. Plots 1 and 2 were in tussock tundra, the most common plant community in the vicinity, while Plot 3 was located adjacent to tussock tundra in a rocky moss-shrub community. Plot size and shape were chosen to optimize TLS data detail and extent. Terrestrial laser scans were performed using a Riegl VZ-400 from either four or five exterior scan positions surrounding each circular plot, depending on terrain complexity, as

well as from one position at the centre of each plot. See Figure 2.2 for a representative example of TLS and ALS data.

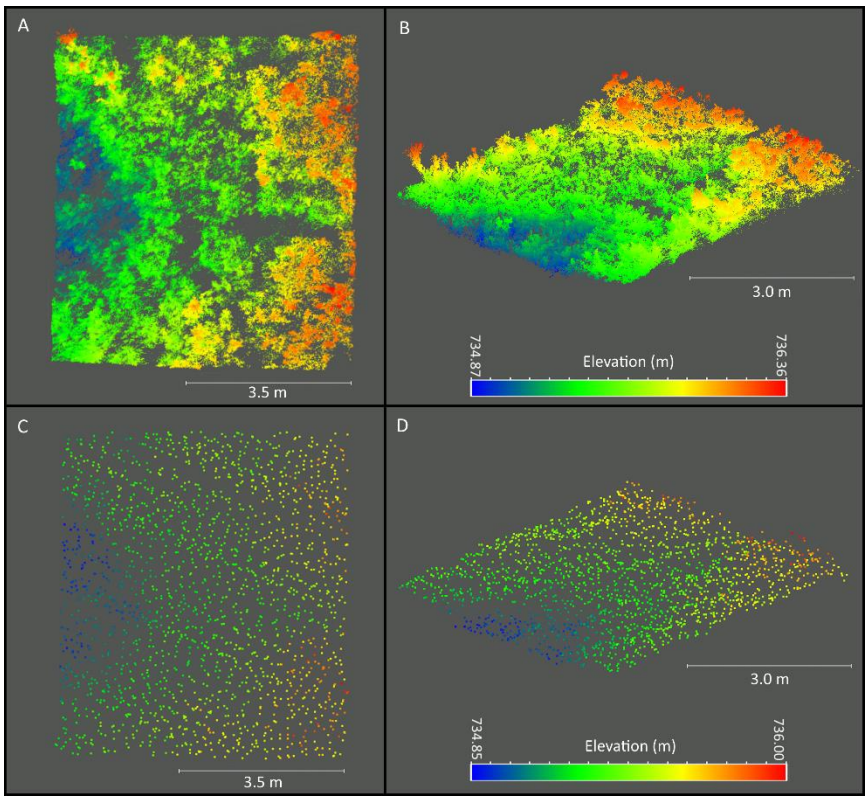

Figure 2.2. Representative detail of TLS (A, B) and ALS (C, D) datasets, showing nadir (A, C) and oblique (B, D) views of the same small area. Colour scales show absolute return elevation for TLS (B) and ALS (D) in meters. Point size is set for best visibility (not to scale).

Table 2.1. ALS and TLS instrument and collection specifications.

ALS	
Instrument	Riegl VQ-480i
Scanner type	Onboard waveform processing, multiple returns
Wavelength	1550 nm
Beam divergence	0.3 milliradians
Flight altitude	365 m above ground level
Vertical accuracy	8-10 cm
Horizontal accuracy	~10 cm
Spot size (laser beam ground footprint)	11 cm
Nominal flight line return density	13.5 points/m^2
Nominal aggregated return density	27 points/m^2
TLS	
Instrument	Riegl VZ-400
Scanner type	Onboard waveform processing, multiple returns
Wavelength	1550 nm
Beam divergence	0.35 milliradians
Repeatability	3 mm
Weight	9.6 kg
Spot size (minimum beam footprint)	0.02 m
Angular scan step (central scan)	0.7 milliradians (spacing = 2 cm at 30 m)
Angular scan step (exterior scan)	0.3 milliradians (spacing = 1 cm at 30 m)

2.2.3. Aboveground shrub biomass harvests

We visited the three TLS scan plots in July 2014 and conducted a total of 60 shrub biomass harvests within them (20 shrub harvest subplots per TLS plot). Harvest subplots were chosen to capture a range of shrub biomass, density, and species. Harvest subplot centre coordinates were measured with a TopCon GR-3 survey grade GPS system running in real time kinematic (RTK) mode (nominal accuracy ~4 cm). At each harvest subplot, we placed a 0.64 m^2 ring and identified woody stems within it greater than 5 cm height. Woody stems originating within the ring but projecting beyond it were clipped so that only the portion within the ring was included in the harvest; similarly, portions of woody stems originating outside the ring but projecting into the ring were included. Stems were clipped to the moss layer and oven-dried at 50°C until their mass measurements stabilized (generally at least 48 hours), then weighed to the nearest tenth of a gram. Dry shrub biomass included stem and leaf material. All shrub species were pooled for analysis, but visual

assessment suggested that species contributing the majority of biomass included *Salix pulchra* Cham., *S. richardsonii* Hook., *S. glauca* L., *Betula nana* L., and *Vaccinium uliginosum* L.

2.3. TLS pre-processing

For each of the three TLS scan plots (containing all shrub biomass harvest subplots), we co-registered and merged all TLS plot scans using RiScan Pro (RIEGL Laser Measurement Systems GmbH, Austria) to form a single point cloud per plot. To reduce noise in the data, we filtered the point clouds based on deviation (a unitless Riegl point quality metric; Pfennigbauer, 2010) retaining only returns with deviation less than 200 (see Greaves et al., 2015).

2.4. Calibration of TLS canopy volume

First, we built a large set of potential canopy volume surfaces by iteratively varying parameters used to identify and rasterize the lowest and highest laser returns across the plots, largely following Greaves et al. (2015) and described below in Section 2.4.1. Table 2.2 shows the parameter values included in the calculation of potential canopy volume surfaces. The circular 0.64 m^2 harvest subplots were clipped from canopy volume surfaces using the subplot GPS locations. We then identified the canopy volume surface that best predicted shrub biomass by employing a leave-one-out cross-validation (LOOCV) procedure, described below in section 2.4.2. All algorithms were scripted using the open-source software package R version 3.0.1 (R Core Team, 2015; scripts available from the authors).

Table 2.2. Values of processing parameters included in canopy volume optimization. Bracketed values [ ] were only used in processing 'lowest' returns.

Processing step	Parameter values included
Filter TLS returns by grid	Grid cell size (m) 0.02, 0.04, 0.05, 0.06, 0.08, 0.10, [0.12, 0.14, 0.15, 0.16, 0.18, 0.20]
[Filter to lowest point in neighbourhood]	[Number of neighbours 4, 8, 12, 16, 20, 24]
Rasterize canopy volume raster	Raster resolution (m) 0.05, 0.10, 0.15, 0.20

2.4.1. Creating potential TLS canopy volume surfaces

The highest TLS returns were identified using a single-pass grid filter that retained only the point with highest elevation (largest *z* value) in each grid cell. Lowest points were identified using a double-pass filter: in the first pass, a grid filter was applied that retained only the point with the smallest *z* value in each grid cell. In the second pass, a nearest-neighbour algorithm was applied that identified the nearest neighbours of each point and retained only the lowest point from among those neighbours (see Table 2.2 for grid cell and neighbourhood sizes considered).

Following identification of lowest and highest points for each combination of parameters, we rasterized these sets of points using the las2dem tool in LAStools (Isenburg, 2017). Then for each combination of parameters, a canopy volume surface was calculated by subtracting the 'lowest' raster from the 'highest' raster and multiplying the result by the square of the raster resolution. Since it was unclear what resolution was appropriate, a range of resolutions (Table 2.2) was included in the optimization procedure. Canopy volume for individual harvest subplots was calculated by summing canopy volume values over the pixels comprising each subplot.

2.4.2. Selecting the best TLS canopy volume surface with LOOCV

Each combination of parameters produced a unique potential canopy volume for each harvest subplot. To protect against overfitting our final model, one-third (n = 20) of harvest subplots were selected using a biomass-stratified random sample and entirely withheld from LOOCV to be used as a test dataset. With the remaining training dataset (n = 40), we performed LOOCV using a simple linear regression of harvested shrub biomass against canopy volume. The optimized (best) canopy volume surface was the one that yielded the lowest cross-validation error. We characterized the strength of the optimized relationship using the coefficient of determination (R^2) and root mean square error (RMSE). To evaluate the predictive strength of this model, we applied it to the test dataset and evaluated the results using R^2, intercept, slope, bias, and root mean square deviation (RMSD; Piñeiro et al., 2008). This model provided us with a TLS-derived shrub biomass estimate ('TLS biomass') that we used as 'truth' for subsequent calibration of ALS data.

2.5. Calibrating ALS canopy volume against TLS-derived biomass

We calibrated ALS canopy volume surfaces against TLS biomass using the same procedure described above in Sections 2.4.1 and 2.4.2 (Figure S2.1 shows the processing relationships among all datasets). All potential parameter values included in the TLS surface-building process were retained for creation of potential ALS canopy volume surfaces, and the same subset of samples was withheld as a test dataset to evaluate the prediction relationship found using LOOCV. The resulting TLS-calibrated ALS biomass model ("TLS-ALS biomass") was evaluated against both TLS biomass and harvested biomass for the test dataset. We performed the LOOCV procedure again to calibrate ALS canopy volume directly against harvested biomass, so that we could also compare the accuracy and calibration behaviour of harvest-calibrated ALS biomass ("Harvest-ALS biomass") against TLS-ALS biomass.

3. Results and Discussion

3.1. Canopy volume surface parameters

Parameter values that identified the lowest and highest returns necessary to create optimal canopy volume were remarkably similar for TLS and ALS (Table 2.3), which was surprising given the differences between TLS and ALS instrument and collection specifications. For example, laser beam diameters of TLS instruments are much smaller than for ALS instruments (~2 cm for TLS vs. ~11 cm for ALS in this study) and TLS operates at much higher point collection densities. This leads to better discrimination of canopy elements with TLS (especially small leaves and branches at the top of a sparse shrub canopy), as well as a superior ability to retrieve returns from ground beneath dense canopies (Figure 2.2). The magnitude of canopy volumes measured in each dataset demonstrates this effect: maximum canopy volumes for subplots in the TLS data were approximately twice the maximum canopy volumes found for the same subplots in the ALS data (~0.4 m^3 vs ~0.2 m^3; compare Figure 2.3A and Figure 2.4A and 2.4C). The underestimation of canopy size by ALS datasets visible in Figure 2.2 is a common problem in shrub ecosystems, where the resulting error can be as much as 50% of the total canopy height (Streutker and Glenn, 2006). Conversely, ALS data are more regularly spaced and less susceptible to the 'shadowing' caused by oblique collection angles of TLS data; this can be seen in several areas of Figure 2.2, where low-lying areas are obscured by vegetation in the TLS data but not in the ALS data. Still, the correspondence between the optimization parameters of TLS and ALS suggest a practical similarity between the two datasets in this case. This was likely due to the relatively high density of the ALS collection (~ 27 points/m^2) and the extremely low stature of the vegetation (<1 m), which led to the TLS instrument collecting data from above the canopy—somewhat more like ALS than in tall shrub or forest environments.

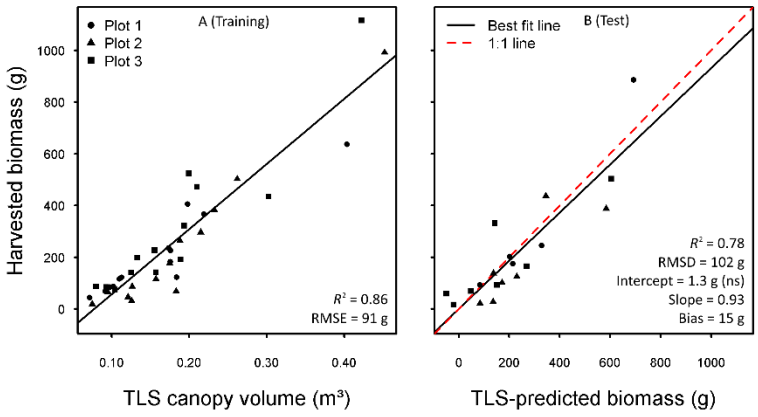

Figure 2.3. Training model (A) and test dataset results (B) for calibrating TLS-derived canopy volume against shrub biomass harvests. 'ns' means not significant at p = 0.05.

Table 2.3. Strongest parameter sets for calibration of canopy volume to biomass for each data source.

	Grid cell size, highest returns (m)	Grid cell size, lowest returns (m)	Neighbourhood size (No. of neighbours)	Canopy volume raster resolution (m)
Harvest-calibrated TLS	0.02	0.15	24	0.05
TLS-calibrated ALS	0.04	0.15	24	0.15
Harvest-calibrated ALS	0.04	0.15	24	0.15

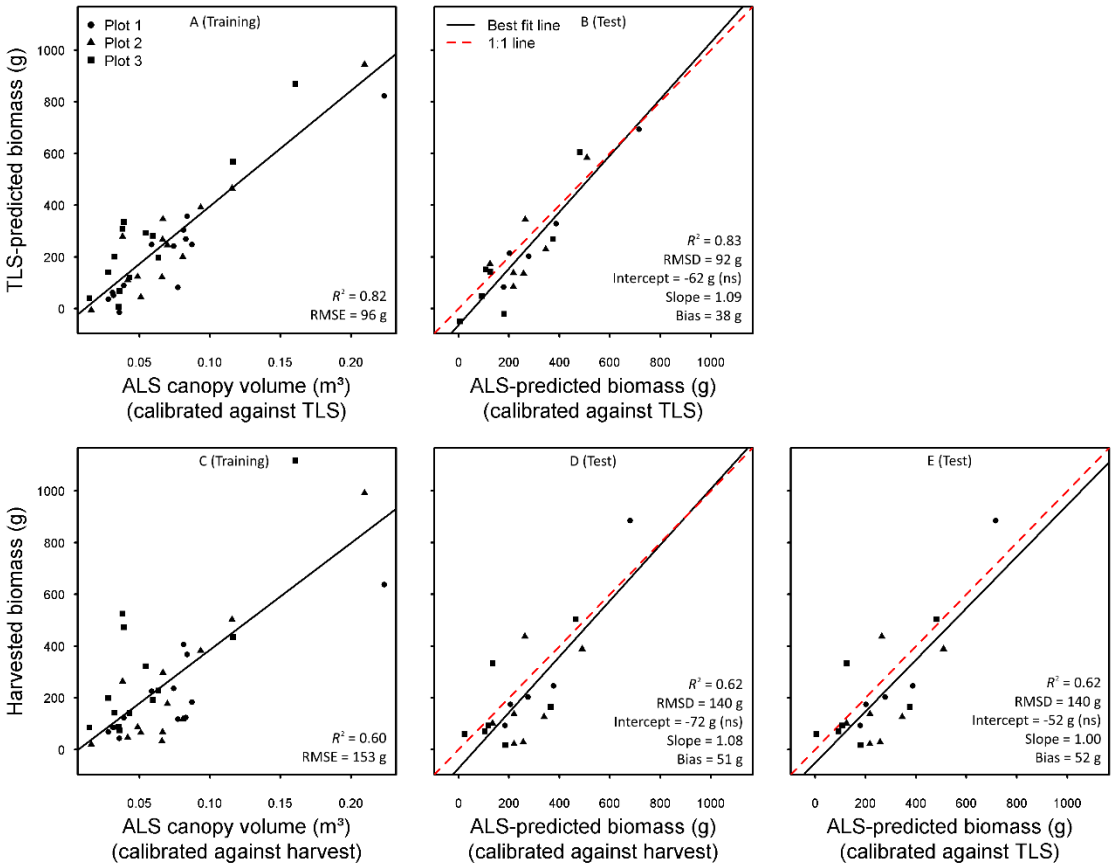

Figure 2.4. First row shows training model (A) and test dataset results (B) for calibrating ALS-derived canopy volume against TLS-derived shrub biomass estimates. Second row shows training model (C) and test dataset results (D) for calibrating ALS-derived canopy volume directly against shrub biomass harvest, and permits comparison between the accuracy of harvest-calibrated ALS biomass estimates (D) and TLS-calibrated ALS biomass estimates (E). 'ns' means not significant at p = 0.05.

The only optimal canopy volume parameter that differed substantially between TLS and ALS datasets was the resolution of the optimized canopy volume raster (0.05 and 0.15 m, respectively). This difference likely reflects the inherent resolution of the TLS and ALS datasets, including both point-spacing and beam size differences. Indeed, the optimal resolution for each dataset

corresponded closely to the laser beam diameters of those datasets (~0.02 m for TLS and ~0.11 m for ALS).

3.2. Biomass training and validation models

TLS-derived canopy volumes produced very accurate aboveground shrub biomass estimates: the TLS biomass training model had an R^2 of 0.86 and RMSE of 91 g (Figure 2.3A); for the test dataset, R^2 was 0.78, with an RMSD of 102 g (Figure 2.3B). This accuracy was expected based on previous work with shrubs in Arctic tundra (Greaves et al., 2015) and sagebrush systems (Olsoy et al., 2014). Some relatively large variations in biomass for a given canopy volume (for example around 0.20 m^3 canopy volume in Figure 2.3A) may be related to differing vegetation canopy density, which is assumed to be constant in a canopy volume-biomass model, but which may vary in reality; for example, two approximately 0.20 m^3 subplots that fall noticeably above the line of best fit in Figure 2.3A are from Plot 3, where the exposed terrain tended to host denser, lower-lying banks of shrubs than the other two plots. This indicates the necessity of acquiring representative harvest samples from areas of interest.

When these TLS biomass estimates were used as 'truth' for calibration of ALS-derived canopy volume (Figure 2.4A and 2.4B), the relationship between the TLS-calibrated ALS canopy volume and TLS biomass was strong (R^2 = 0.82, RMSE = 96 g) and the test regression showed that the TLS-ALS biomass estimates could predict TLS biomass with an R^2 of 0.83 and RMSD of 92 g. When compared to harvested biomass (Figure 2.4E), TLS-ALS biomass estimates were still robust, with an R^2 of 0.62 and RMSD of 140 g. This represents, essentially, the actual accuracy that could be expected when calibrating ALS canopy volume against TLS-derived biomass estimates.

Most striking, however, was that these TLS-ALS biomass estimates (Figure 2.4E) were essentially identical (mean difference 1.25 g) to the Harvest-ALS biomass estimates, which were derived from direct calibration of ALS against harvest data (Figure 2.4D). The similarity arises from the selection of the same potential ALS canopy volume surfaces during both TLS-ALS optimization and Harvest-ALS optimization (Table 2.3), and implies that there was no loss of accuracy caused by calibrating ALS data against TLS data, rather than calibrating directly against harvest data. This suggests that if there is a known relationship between TLS canopy volume and aboveground shrub biomass for a study area, TLS-derived shrub biomass estimates can be used to calibrate ALS-derived estimates without the need for additional harvests. This would be an advantage any time that performing destructive harvests is undesirable—such as in ecosystems that are slow to regenerate

or legally protected, in studies of vegetation change over time, or for research in long-term monitoring plots.

As a final note, in addition to describing the potential for using TLS to calibrate ALS data, our results permit comparison of the absolute accuracy that can be achieved with TLS and ALS datasets using this approach. The uncertainties (RMSD) were not especially large for either the TLS or ALS shrub biomass estimates (92 g and 140 g, respectively), relative to the range of harvested shrub biomass sampled (16 g – 1100 g; mean 238 g), but TLS data represented the biomass (Figure 2.3) and the fine details (Figure 2.2) of the shrub canopy much more accurately than ALS. Given the slow growth of tundra vegetation and the short timescales of most research efforts, relying on the greater accuracy and sensitivity of TLS data whenever possible may prove important for successful change detection and monitoring as this challenging landscape continues to respond to dramatic changes in climate.

Acknowledgements

Field assistance from Moyo Ajayi, Rebecca Gibson, and Libby Fortin was invaluable. The authors are also thankful for the support of the staff and greater research community of Toolik Field Station, Institute of Arctic Biology, University of Alaska Fairbanks, with special thanks to Jason Stuckey, Randy Fulweber, and Jorge Noguera of Toolik GIS for assistance with ALS ground control and GPS. Airborne lidar data were collected by Kodiak Mapping, Inc., Palmer, AK, www.kodiakmapping.com. This work was supported by NASA Terrestrial Ecology grant NNX12AK83G (LAV, PI), NASA Earth Science Fellowship NNX15AP04H awarded to HEG, and NASA Idaho Space Grant Fellowship NNX10AM75H awarded to TSM. Riegl VZ-400 and accessories were provided by the UNAVCO Facility with support from NSF and NASA under NSF Cooperative Agreement No. EAR-0735156.

References

Greaves, Heather E, Lee A Vierling, Jan U H Eitel, Natalie T Boelman, Troy S Magney, Case M Prager, and Kevin L Griffin. 2016. “High-Resolution Mapping of Aboveground Shrub Biomass in Arctic Tundra Using Airborne Lidar and Imagery.” Remote Sensing of Environment 184: 361–373. doi:10.1016/j.rse.2016.07.026.

Greaves, Heather E., Lee A. Vierling, Jan U.H. Eitel, Natalie T. Boelman, Troy S. Magney, Case M. Prager, and Kevin L. Griffin. 2015. “Estimating Aboveground Biomass and Leaf Area of Low-Stature Arctic Shrubs with Terrestrial LiDAR.” Remote Sensing of Environment 164: 26–35. doi:10.1016/j.rse.2015.02.023.

Hilker, Thomas, Martin van Leeuwen, Nicholas C. Coops, Michael A. Wulder, Glenn J. Newnham, David L B Jupp, and Darius S. Culvenor. 2010. “Comparing Canopy Metrics Derived from Terrestrial and Airborne Laser Scanning in a Douglas-Fir Dominated Forest Stand.” Trees - Structure and Function 24 (5): 819–832. doi:10.1007/s00468-010-0452-7.

Hopkinson, Chris, Jenny Lovell, Laura Chasmer, David Jupp, Natascha Kljun, and Eva van Gorsel. 2013. “Integrating Terrestrial and Airborne Lidar to Calibrate a 3D Canopy Model of Effective Leaf Area Index.” Remote Sensing of Environment 136 (September): 301–314. doi:10.1016/j.rse.2013.05.012.

Isenburg, Martin. 2015. “LAStools - Efficient Tools for Lidar Processing. Version 140329. Http://lastools.org.”

Jones, Benjamin M, Jason M Stoker, Ann E Gibbs, Guido Grosse, Vladimir E Romanovsky, Thomas A Douglas, Nicole E M Kinsman, and Bruce M Richmond. 2013. “Quantifying Landscape Change in an Arctic Coastal Lowland Using Repeat Airborne LiDAR.” Environmental Research Letters 8 (4) (December 1): 045025. doi:10.1088/1748-9326/8/4/045025.

Li, Aihua, Nancy F. Glenn, Peter J. Olsoy, Jessica J. Mitchell, and Rupesh Shrestha. 2015. “Aboveground Biomass Estimates of Sagebrush Using Terrestrial and Airborne LiDAR Data in a Dryland Ecosystem.” Agricultural and Forest Meteorology 213: 138–147. doi:10.1016/j.agrformet.2015.06.005.

Myers-Smith, Isla H, Bruce C Forbes, Martin Wilmking, Martin Hallinger, Trevor Lantz, Daan Blok, Ken D Tape, et al. 2011. “Shrub Expansion in Tundra Ecosystems: Dynamics, Impacts and Research Priorities.” Environmental Research Letters 6 (4) (December 1). doi:10.1088/1748-9326/6/4/045509.

Olsoy, Peter J., Nancy F. Glenn, Patrick E. Clark, and DeWayne R. Derryberry. 2014. “Aboveground Total and Green Biomass of Dryland Shrub Derived from Terrestrial Laser Scanning.” ISPRS Journal of Photogrammetry and Remote Sensing 88 (February): 166–173. doi:10.1016/j.isprsjprs.2013.12.006.

Pfennigbauer, Martin. 2010. “Improving Quality of Laser Scanning Data Acquisition through Calibrated Amplitude and Pulse Deviation Measurement.” Proceedings of SPIE 7684: 76841F–76841F–10.

Pineiro, Gervasio, Susana Perelman, Juan P Guerschman, and Jose M Paruelo. 2008. “How to Evaluate Models: Observed vs. Predicted or Predicted vs. Observed?” Ecological Modelling 216: 316–322. doi:10.1016/j.ecolmodel.2008.05.06.

R Core Team. 2015. “R: A Language and Environment for Statistical Computing.” R Foundation for Statistical Computing. Vienna, Austria. URL http://www.R-Project.org/. http://www.r-project.org.

Selkowitz, David J. 2010. “A Comparison of Multi-Spectral, Multi-Angular, and Multi-Temporal Remote Sensing Datasets for Fractional Shrub Canopy Mapping in Arctic Alaska.” Remote Sensing of Environment 114 (7) (July): 1338–1352. doi:10.1016/j.rse.2010.01.012.

Streutker, David R., and Nancy F. Glenn. 2006. “LiDAR Measurement of Sagebrush Steppe Vegetation Heights.” Remote Sensing of Environment 102 (1-2) (May): 135–145. doi:10.1016/j.rse.2006.02.011.

Vierling, Lee A, Yanyin Xu, Jan U H Eitel, and John S Oldow. 2012. “Shrub Characterization Using Terrestrial Laser Scanning and Implications for Airborne LiDAR Assessment.” Canadian Journal of Remote Sensing 38 (6): 709–722.

Supplemental Data

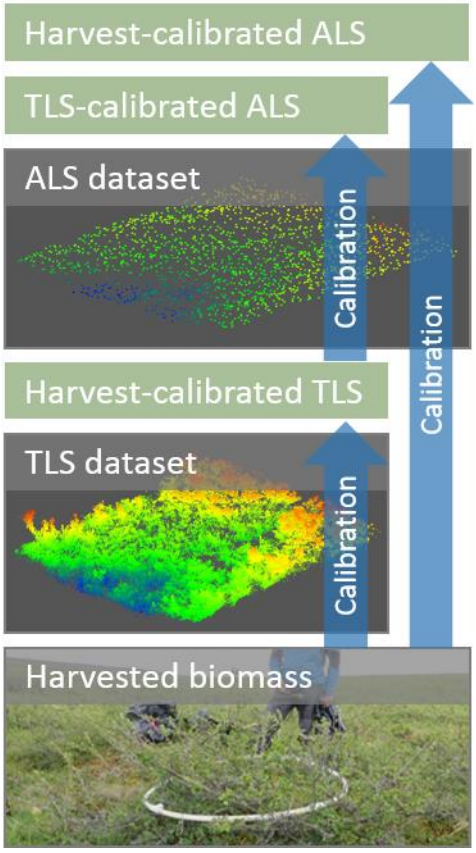

Figure S2.1. Conceptual diagram showing the derivation of aboveground shrub biomass estimates in the study. Harvested biomass was used to calibrate TLS-derived estimates of shrub biomass, which were subsequently used to calibrate ALS-derived estimates. Harvested biomass was also used to calibrate ALS-derived estimates directly.

CHAPTER 3: HIGH-RESOLUTION MAPPING OF ABOVEGROUND SHRUB BIOMASS IN ARCTIC TUNDRA USING AIRBORNE LIDAR AND IMAGERY

Greaves, H.E., Vierling, L.A., Eitel, J.U.H., Boelman, N.T., Magney, T.S., Prager, C.M., and Griffin, K.L. "High-resolution mapping of aboveground shrub biomass in Arctic tundra using airborne lidar and imagery". *Remote Sensing of Environment* (184), 2016, pp. 361-373.

Abstract

Accurate monitoring of climate-driven expansion of low-stature shrubs in Arctic tundra requires high-resolution maps of shrub biomass that can accurately quantify the current baseline over relevant spatial and temporal extents. In this study, our goal was to use airborne lidar and imagery to build accurate high-resolution shrub biomass maps for an important research landscape in the American Arctic. In a leave-one-out cross-validation analysis, optimized lidar-derived canopy volume was a good single predictor of harvested shrub biomass (R^2 = 0.62; RMSD = 219 g m^{-2}; slope = 1.08). However, model accuracy was improved by incorporating additional lidar-derived canopy metrics and airborne spectral metrics in a Random Forest regression approach (pseudo R^2 = 0.71; RMSD = 197 g m^{-2}; slope = 1.02). The best Random Forest model was used to map shrub biomass at 0.80 m resolution across three lidar collection footprints (~12.5 km^2 total) near Toolik Field Station on Alaska's North Slope. We characterized model uncertainty by creating corresponding maps of the coefficient of variation in Random Forest shrub biomass estimates. We also explore potential benefits of incorporating lidar-derived topographic metrics, and consider tradeoffs inherent in employing different data sources for high-resolution vegetation mapping efforts. This study yielded maps that provide valuable, high-resolution spatial estimates of aboveground shrub biomass and canopy volume in a rapidly changing tundra ecosystem.

1. Introduction

Accelerating climate warming in Arctic regions appears to be stimulating an increase in abundance, size, and range of deciduous tundra shrubs—mostly willow (*Salix* spp.), birch (*Betula* spp.) and alder (*Alnus* spp.) (Myers-Smith et al., 2015, 2011; Naito and Cairns, 2015; Tape et al., 2006). This shift in tundra vegetation communities is expected to impact wildlife habitat and trophic interactions (Boelman et al., 2014; Rich, Gough, & Boelman, 2013), alter carbon and nutrient storage and cycling (Mack et al., 2004; Schimel et al., 2004), influence hydrology and permafrost dynamics (Blok et al., 2010; Lawrence and Swenson, 2011), and may contribute to additional warming (Chapin et al., 2005; Loranty and Goetz, 2012). To permit accurate accounting of these ecological changes,

and to facilitate modeling and prediction of landscape trajectories as climate continues to warm, researchers and managers require spatial models (maps) of tundra vegetation structure and biomass. However, the fine spatial heterogeneity and low stature of tundra vegetation communities present a daunting challenge for conventional methods of mapping aboveground vegetation biomass.

Owing to the considerable extent of the Arctic tundra biome, maps of tundra vegetation attributes often cover large areas at coarse resolution (e.g. the Circumpolar Arctic Vegetation Map [CAVM]; Walker et al., 2005). Moderate resolution (20+ m pixel) vegetation maps exist for some tundra regions: in Alaska, for example, the North Slope, and especially the Dalton Highway corridor stretching from Prudhoe Bay to the Brooks Range, is one of the best-studied and best-mapped regions of the American Arctic. Multiple efforts have been made in that region to characterize coarse- and moderate-scale land cover (Ducks Unlimited, 2013; Muller et al., 1999; Raynolds et al., 2005; Walker et al., 2005; www.arcticatlas.org; Walker and Maier, 2007) and total aboveground biomass (Raynolds et al., 2012; Shippert et al., 1995; Simms and Ward, 2013; Walker et al., 2005), but there have been relatively few attempts to describe existing shrub characteristics in better detail or higher resolution.

The shortage of high-resolution maps (<20 m pixel) represents a significant data gap, since these maps are necessary for characterizing spatial heterogeneity of tundra vegetation (Lantz et al., 2010; Naito and Cairns, 2015; Raynolds et al., 2008), calibrating and validating coarser maps (Stow et al., 2004), and estimating related fine-scale ecological function such as wildlife habitat suitability (Boelman et al., 2014). These considerations are especially important in tundra ecosystems, where vegetation communities can be heterogeneous at extremely fine spatial scales (e.g. <1 m; M. D. Walker, Walker, & Auerbach, 1994), rendering moderate-resolution maps inadequate (Lantz et al., 2010; Stow et al., 2004). Additionally, although shrubs are the tallest common vegetation on the treeless tundra landscape, their height rarely exceeds 2 m except in deeply thawed riparian areas; generally, tundra shrubs are less than 1 m in height and occur in slow-growing, irregular patches or dispersed among other tundra vegetation. Such low-stature, heterogeneous vegetation is especially difficult to identify and quantify using coarse- and moderate-resolution passive satellite-based remote-sensing approaches.

Maps that focus on characteristics of shrub canopies are especially uncommon. Active satellite-based data such as synthetic aperture radar (SAR) show promise for mapping shrub attributes at moderate resolution (Duguay et al., 2015), although so far such approaches are

relatively rare. Selkowitz (2010) explored the potential strengths of different passive satellite data sources for moderate-resolution fractional shrub cover mapping over a swath of northern Alaska; Beck et al. (2011) used a selection of high-resolution commercial satellite imagery (IKONOS and SPOT, 1-5 m pixel) to train a model that estimated fractional cover of total and 'tall' (>1 m) shrubs at 30 m resolution across the entire North Slope of Alaska. While these moderate-resolution maps represent valuable baselines for understanding shrub cover over a large and ecologically important area, their resolution limits their applicability and poses challenges for verification in local areas. For example, in Beck et al. (2011), validation could only be performed against existing maps of similar or coarser resolution, and against relatively few (24) visual cover estimates by field observers, rather than against quantitative *in situ* measurements or higher resolution validated maps. Further, these maps (necessarily for their resolution) quantify percent shrub cover per area, a metric that obscures gradients in shrub structure and spatial patterns of distribution and constrains applications that depend on understanding these properties. Higher resolution maps are likely necessary to provide baselines against which incremental changes in heterogeneous shrub cover can be evaluated, especially in topographically complex landscapes (e.g. Naito and Cairns, 2015; Raynolds et al., 2008). Accurately identifying and monitoring vegetation changes, and understanding and quantifying landscape processes and function occurring at such fine scales requires high-resolution maps that can capture fine-grained heterogeneity and gradients in low-stature vegetation at a spatial scale relevant to the vegetation. Although such high-resolution maps would necessarily be limited in extent, coverage of even a few important landscapes would provide outsized informational value to researchers and managers working across the biome.

Challenges inherent in mapping heterogeneous low-stature vegetation highlight the importance of airborne and surface-based remote sensing approaches. Airborne lidar (light detection and ranging) has proven to be a powerful tool for quantifying structure-related attributes in ecosystems as diverse as forests (Dubayah and Drake, 2000; Hudak et al., 2012), Mediterranean woodlands (Estornell et al., 2012), salt marshes (Hladik et al., 2013), rangelands (Ritchie et al., 2001; Streutker and Glenn, 2006; Lee A Vierling et al., 2013), and agricultural fields (Eitel et al., 2014a). Airborne lidar can be collected over small to moderate spatial extents and at a high spatial resolution (generally 1-30 data points per square meter). Lidar provides three-dimensional (3D) structural information that is difficult to quantify from passive optical data, making it especially relevant to the challenges of quantifying subtle variations in vegetation structure.

Although the high resolution and three-dimensionality of lidar make it a strong and flexible tool, using lidar to quantify vegetation metrics in low-stature ecosystems remains challenging. Methods for using lidar data to derive biomass estimates for shrubs (Estornell et al., 2011; Greaves et al., 2015; Olsoy et al., 2014) generally differ from methods established in forest systems, due to the severely abbreviated height range of shrub canopies. Low vegetation stature is often further exaggerated in lidar data, because airborne lidar tends to significantly underestimate vegetation heights in shrub systems. This may occur because of threshold limitations of the laser sensor, or because a laser pulse may miss the highest branch of a sparse shrub or fail to reach the ground through dense shrub canopies. These difficulties can make it impossible to accurately retrieve ground or canopy surfaces (and therefore canopy height) in areas of dense shrub cover. Depending on the density of the canopy and of the lidar data collection, the resulting error in vegetation height estimates can represent up to 50% of total shrub height (Streutker and Glenn, 2006).

Despite these difficulties, previous research with terrestrial (ground-based) lidar has shown that lidar-derived canopy volume can provide a good proxy for aboveground biomass in Arctic tundra (Greaves et al., 2015), as well as in dry sagebrush systems (Olsoy et al., 2014) and agricultural settings (Eitel et al., 2014a). Quantifying canopy volume provides a direct, continuous metric of canopy structure that can encompass both horizontal and vertical components of vegetation, especially when measured at high spatial resolution. Given the problems inherent in using lidar to identify ground and canopy surfaces in shrub systems, lidar-derived shrub canopy volumes are unlikely to be correct in an absolute sense; however, they provide meaningful data when well calibrated against *in situ* vegetation sampling (Greaves et al., 2015; Olsoy et al., 2014). And although canopy volume is less commonly used than other airborne lidar metrics (but see e.g. Kim et al., 2009; Tao et al., 2014), the previous success of volumetric approaches with terrestrial lidar suggests that such methods may also be successful with airborne lidar data. This may be particularly true in very low-stature ecosystems like Arctic tundra, where both terrestrial and airborne lidar data are acquired from above the canopy, making such datasets more similar to each other than they might be otherwise.

In this study, we investigate the potential for mapping shrub biomass estimates using lidar-derived canopy volume in a simple linear regression model. Such a parsimonious model would be less susceptible to overfitting of training data than a more complex model, and detecting changes across multiple datasets collected over time would be fairly straightforward (e.g. Jones et al., 2013)—especially because lidar datasets are somewhat more repeatable than aerial photography or

even satellite data, which are more susceptible to variations caused by sun-sensor geometry and atmospheric effects (see Bater et al., 2011 for a discussion of lidar data stability over multiple data collections).

Although such a simple model is attractive, fusing lidar with spectral data has yielded improved estimates of vegetation biomass in a range of ecosystems (Zolkos et al., 2013); for example this approach has enhanced sagebrush mapping (Mundt et al., 2006), tree species classification (Dalponte et al., 2008), and quantification of tree structure (Hyde et al., 2006). This complementarity of lidar and spectral data is logical, since lidar measures the 3D structure of vegetation, while spectral data suggest its species and physiological state. For example, Reese et al. (2014) found that combining lidar and spectral data improved classification of alpine vegetation types, because spectral data improved differentiation among vegetation types that have similar vertical structure but different spectral properties, while lidar data improved differentiation among vegetation types with similar spectral properties but different vertical structure.

Combining lidar with high-resolution spectral data is an especially powerful technique for characterizing shrubs in low-stature ecosystems (Estornell et al., 2012; Mundt et al., 2006; Riaño et al., 2007), suggesting that the potential for improved mapping accuracy may outweigh a preference for a simple model. In the Arctic, high-resolution photography has been especially important in illuminating ongoing changes in vegetation communities (Naito and Cairns, 2015; Tape et al., 2006), as it has historically been the only technique that permits detection of individual Arctic shrubs at the hillslope scale. However, few studies in Arctic tundra have combined lidar with high-resolution spectral data (Goswami et al., 2011; Rees, 2007), and the authors are aware of no prior studies using this approach to estimate shrub biomass or distribution in the Alaskan Arctic.

In this study, our goal was to create accurate, high-resolution maps of shrub biomass for an important research landscape on the North Slope of Alaska. Our specific objectives were 1) to investigate the potential for using lidar-derived canopy volume as a single predictor in a simple shrub biomass regression model, and 2) to compare the accuracy of this simple model to a more complex model incorporating both lidar and high-resolution spectral data. By comparing these approaches and exploring the implications of each, we sought to illuminate the relative strengths of lidar- and spectral- derived metrics for predicting Arctic shrub biomass, potentially informing future investigations into this challenging research field.

2. Methods

2.1. Study area

The study area is near Toolik Lake (68°38’ N latitude, 149°36’ W longitude) in the northern foothills of the Brooks Range, Alaska, USA (Figure 3.1). The tundra landscape is underlain by continuous permafrost, with expansive rolling hills of tussock tundra dominated by tussock cottongrass (*Eriophorum vaginatum* L.) and other sedges (especially *Carex* spp.), along with mosses (frequently *Sphagnum* spp.) and low-stature (generally <1 m) deciduous shrubs (mainly *Betula nana* L. and *Salix* spp.). Tussocks, hummocks, and glacial features create a complex topographic patchwork at fine (<1 m) to moderate (50 m) scales. Mean precipitation in the area is approximately 300 mm, roughly half of which falls as winter snow, and growing-season temperatures average 10°C.

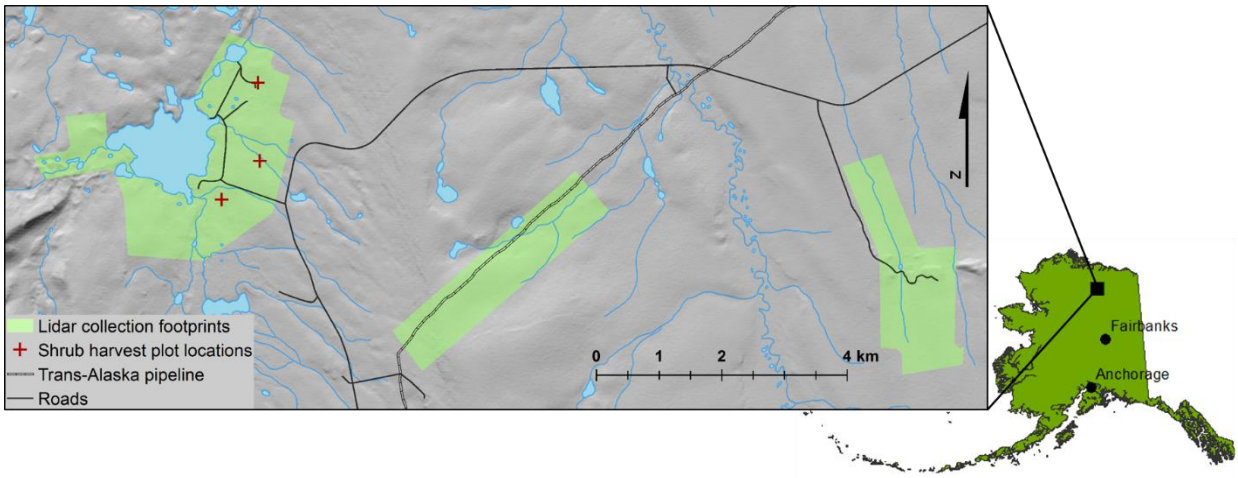

Figure 3.1. Location of study area in northern Alaska. Detail view shows three lidar collection footprints in pale green (from left to right: Toolik, Pipeline Ridge, Imnavait). Red crosses indicate locations of shrub harvest areas within the Toolik lidar footprint.

2.2. Data collection

2.2.1. Aboveground shrub biomass harvests

We conducted 60 shrub biomass harvests—20 within each of three 25 m radius circular areas near Toolik Field Station (Figure 3.1). Harvest plot placement was chosen subjectively to capture a range of shrub species, biomass, density, and structure. Harvest plot center coordinates were measured with a TopCon GR-3 survey grade GPS system running in real time kinematic (RTK) mode (nominal accuracy ~4 cm). At each harvest plot, we placed a 0.64 m^2 ring and identified all woody stems within it greater than 5 cm height. These woody stems were clipped to the moss layer and oven-dried at 50°C until their mass measurements stabilized (generally >48 hours), then weighed to the nearest tenth of a gram to determine total dry shrub biomass per plot. Dry shrub

biomass included both stem and leaf material. All shrub species were pooled for analysis, but visual assessment suggested that species contributing the majority of biomass included *Salix pulchra* Cham., *S. richardsonii* Hook., *S. glauca* L., *Betula nana* L., and *Vaccinium uliginosum* L.

2.2.2. Airborne lidar and imagery collection

Airborne lidar data and digital imagery were collected August 1st, 2013, in three separate footprints near Toolik Lake totaling 12.5 km^2 (Figure 3.1; Vierling et al., 2013a, 2013b). The largest collection footprint (hereafter referred to as 'Toolik', ~6 km^2) wraps around Toolik Lake from the northeast to southwest. The other two collection footprints are each ~3 km^2; one is situated along the Trans-Alaska Pipeline where it crosses the high moraine ridge ~3 km east of Toolik Lake ('Pipeline Ridge') and the other covers much of the research area along Imnavait Creek, ~10 km east of Toolik Lake ('Imnavait'). The areas covered by these three footprints have different glacial histories but similar vegetation communities. Lidar collection parameters are shown in Table 3.1. The lidar vendor performed standard pre-processing of the airborne lidar data, including aircraft attitude adjustments and ground control georectification. For this study, all laser returns were included in analyses (i.e. we did not filter data based on return numbers, return intensities, or scan angles). Simultaneous 4-band digital imagery (RGB and near infrared, hereafter 'RGB-NIR') was collected with a Leica RCD30 60MP camera mounted to the aircraft, and was processed and orthorectified by the lidar vendor to create orthoimagery mosaics with a pixel resolution of 4.25 cm. A GPS spot-check of 40 stationary objects distributed across the Toolik data collection footprint suggested that the imagery was accurately orthorectified to within 10 cm.

Table 3.1. Lidar collection specifications.

Instrument	Riegl VQ-480i
Scanner type	Onboard waveform processing yielding multiple discrete returns
Wavelength	1550 nm
Beam divergence	0.3 milliradians
Flight altitude	365 m above ground level
Vertical accuracy	8-10 cm
Horizontal accuracy	~10 cm
Spot size (laser beam ground footprint)	11 cm
Nominal flight line return density	13.5 points m^{-2}
Nominal aggregated return density	27 points m^{-2}

2.3. Lidar canopy volume processing

We created a rasterized canopy volume map using an optimization algorithm based on previous work with terrestrial lidar (Greaves et al., 2015). The algorithm was written in the R statistical language (R Core Team, 2017) and is available from the authors. To produce canopy volume, the algorithm iteratively alters search parameters that are used to classify and rasterize laser returns. The optimal parameter set was the one that produced canopy volume with the lowest cross-validation error in a leave-one-out cross validation (LOOCV) regression against harvested shrub biomass. To identify 'ground' (lowest) laser returns, a double-pass search algorithm first applies a grid to the complete point cloud and identifies the lowest return within each grid cell (optimized grid cell size for this study was 15 cm); remaining returns are further thinned on a second pass that examines the nearest neighbors of each return and eliminates all but the lowest return in each neighborhood (optimized neighborhood size for this study was 24 neighbors). 'Top-of-canopy' (highest) laser returns are identified in a single-pass grid search of the complete point cloud for the highest laser returns in each cell (optimized grid cell size in this study was 4 cm). These lowest and highest laser returns are then interpolated and rasterized at an optimized resolution (15 cm in this study) and the volume between them is calculated. Optimized parameter values were similar (e.g. within ~4 cm for grid cell sizes) to parameters similarly optimized for terrestrial lidar scans of a different set of shrubs in this study area (Greaves et al., 2015), suggesting the general transferability of the method within this vegetation community. Canopy volume rasters were subsequently aggregated to 0.80 m resolution to match the area of the shrub harvest plots.

We characterized the strength of the relationship between optimized canopy volume and harvested shrub biomass using the coefficient of determination (R^2) and root mean squared error (RMSE). To evaluate the predictive strength of this simple model, we applied the model to predict biomass for a stratified-random sample of harvested shrubs that had been withheld from the optimization algorithm (i.e. a test dataset, n = 20). We then regressed the observed harvested shrub biomass values against predicted shrub biomass and calculated the intercept, slope, bias, R^2, and root mean squared deviation (RMSD) to evaluate the performance of the model. Employing LOOCV and evaluating the resulting model on a subsample of withheld data minimized overfitting and allowed a more accurate assessment of model prediction strength. Note that when used to describe the relationship between observed and predicted values, R^2 indicates what proportion of the variation in observed values is explained by variation in the predicted values. Also, while RMSE and RMSD are similar, RMSE is a regression fit metric calculated as the square root of the mean of the

summed squared regression residuals, and describes the variation around the best-fit regression line. RMSD is a prediction strength metric calculated as the square root of the mean of the summed squared differences between predicted and observed values, and describes the variation around the 1:1 line. See Pineiro et al. (2008) for a discussion of model evaluation tools, including R^2, RMSE, and RMSD.

The optimized set of classification parameters was applied to all lidar returns to create wall-to-wall canopy volume rasters for the three lidar footprints. As discussed in the introduction, above, we recognize that these canopy volumes are unlikely to be accurate in absolute terms because of the difficulty in identifying bare earth and canopy surfaces in shrubby areas. In the Arctic tundra of northern Alaska, retrieving terrain and canopy information from lidar is further complicated by the unique tundra vegetation: in many places the 'ground' is a continuous carpet of deep mosses and densely spaced tussocks, not soil (Figure 3.2). This presents an additional conundrum for ground-finding—namely, in these areas, there are no data that can be reasonably interpreted as bare earth. Given these complications, and because our goal was to estimate shrub biomass, and not to create accurate digital models of terrain or canopy surfaces (a separate research goal beyond the scope of this study), we did not characterize the absolute error in our canopy volume layers or the optimized ground and top-of-canopy surfaces used to derive them. To avoid implying otherwise, we refrain from using standard terminology such as 'digital terrain model' when referring to these optimized surfaces or their derivatives.

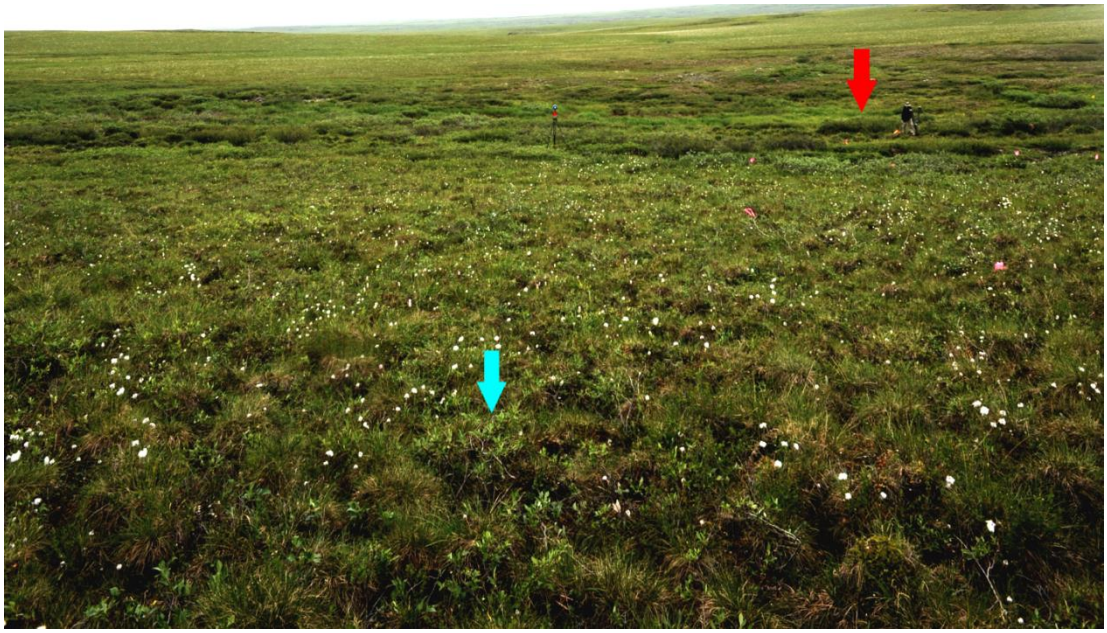

Figure 3.2. Example of complex tundra microtopography and absence of 'bare earth' showing low-stature shrubs (~0.25 m; example indicated with blue arrow) growing among cottongrass tussocks and moss in the foreground, and hummocks with larger shrubs (~0.80-1 m; example indicated with red arrow) in the middle distance. Photo was taken near the detail image shown in Figure 5B-E. A reflective target at the upper center (tripod with red circle, ~2 m tall) and a person near the red arrow provide scale.

2.4. Additional lidar canopy metrics

We used the optimized ground points to pseudo-normalize vegetation return heights in LAStools (Isenburg, 2015; we use the term 'pseudo-normalize' to acknowledge the shortcomings of using the optimized surfaces for this purpose). These height-normalized point clouds were further processed in LAStools to create layers representing maximum estimated canopy height, vegetation density, and standard deviation of maximum heights (Table 3.2). These layers were produced at 0.80 m resolution using a 0.05 m vegetation height threshold, to match the area and harvest protocol of our shrub harvest plots. Each statistical metric was calculated using the 'raster' R package (Hijmans, 2015) over a 3x3 pixel (i.e. 2.4 m) moving window to ensure sufficient lidar return data for reasonable statistics.

Table 3.2. Input groups and individual variables included Random Forest variable selection.

Metric	Description	Data source
Lidar-derived canopy metrics		
Canopy volume	Volume contained between lowest and highest lidar-derived surfaces	Optimized canopy volume raster
Vegetation density	Ratio of vegetation points to ground points	Height-normalized point cloud
Maximum canopy height	Estimated maximum height of top-of-canopy surface	Height-normalized point cloud
Standard deviation of max height	Standard deviation of canopy height; indicates canopy roughness	Height-normalized point cloud
Lidar-derived topographic metrics		
Topographic position index (TPI)	Distinguishes local topographic features like knobs and watertracks	Optimized ground surface, 100 m radius
Hillshade	Generalized directional topographic exposure	Optimized ground surface, 180° azimuth, 30° zenith
SAGA wetness index (SWI)	Potential soil moisture	Optimized ground surface
Morphometric protection index (MPI)	Local topographic relief or openness	Optimized ground surface
Spectral metrics		
Maximum NDVI (2.4 m)	Maximum value of NDVI in neighborhood	Aerial RGB-NIR orthoimagery, 2.4 m moving window
Mean NDVI (2.4 m)	Mean value of NDVI in neighborhood	Aerial RGB-NIR orthoimagery, 2.4 m moving window
NDVI (0.8 m)	Value of NDVI at harvest plot scale	Aerial RGB-NIR orthoimagery, 0.8 m
Maximum 2GRBi (2.4 m)	Maximum value of 2GRBi in neighborhood	Aerial RGB-NIR orthoimagery, 2.4 m moving window
Mean 2GRBi (2.4 m)	Mean value of 2GRBi in neighborhood	Aerial RGB-NIR orthoimagery, 2.4 m moving window
2GRBi (0.8 m)	Value of 2GRBi at harvest plot scale	Aerial RGB-NIR orthoimagery, 0.8 m

2.5. Lidar-derived topographic metrics

We derived estimated topographic metrics (Table 3.2) from optimized ground surfaces using ArcGIS (version 10.1; ESRI, Redlands, CA) and SAGA GIS (System for Automated Geoscientific Analyses version 2.1.4, http://www.saga-gis.org). Topographic position index (TPI) is the elevation of a ground pixel relative to the pixels within a radius (we used a 100 m radius to incorporate

topographic variability at that scale); larger values indicate local ridges and high points, which in the tundra may be more wind-scoured and well-drained, while smaller values reflect low spots that may be comparatively protected and water-saturated (Walker et al., 1994). Hillshade is a standard ArcGIS tool meant to represent topographic shadowing, here calculated with an azimuth angle of 180° and a zenith of 30° to approximate cumulative exposure to prevailing southerly winds and higher, warmer southern sun angles. The SAGA Wetness Index (SWI) is similar to the Topographic Wetness Index (TWI) but uses a different catchment area calculation; it has previously been helpful in predicting vegetation type in alpine systems (Reese et al., 2014). Morphometric Protection Index (MPI; Yokoyama, Shirasawa, & Pike, 2002) is a measure of how the surrounding terrain protects the location of a given pixel from exposure; it was calculated with a radius of 50 m.

2.6. Spectral metrics

Maximum and mean values for both NDVI and 2GRBi ('excess greenness', Richardson et al., 2007) were calculated from the aerial RGB-NIR images at 0.80 m resolution, and then using 2.4 m moving windows to incorporate information from surrounding vegetation. NDVI is highly correlated with aboveground biomass in tundra ecosystems, at least at moderate and coarse scales (Raynolds et al., 2012; Shippert et al., 1995). 2GRBi, although less commonly used, shows promise as a vegetation index that requires only commonly available RGB bands; additionally, preliminary analysis suggested that 2GRBi may be more sensitive than NDVI to the presence of particular tundra shrub species that reflect strongly across the visible range (e.g. *S. richardsonii*, *S. alaxensis*) and therefore produce a weak NDVI signal despite potentially large biomass. However, it is worth noting that 2GRBi is not a normalized index, and since the aerial imagery was not radiometrically calibrated, it would potentially be difficult to compare 2GRBi values across datasets. NDVI and 2GRBi were calculated as:

$$NDVI = (NIR - Red)/(NIR + Red)$$

$$2GRBi = 2 * (Green) - (Red + Blue)$$

where *NIR*, *Red*, *Green*, and *Blue* represent the absolute brightness of the near infrared, red, green, and blue channels, respectively.

2.7. Building complex models with Random Forest

Random Forest (Breiman, 2001) is a classification and regression tree approach that uses ensembles ('forests') of classification or regression trees, with each tree selecting and permuting randomized subsets of predictor variables. The iteration and randomization procedure reduces overfitting, improves the strength of predictions, and has proven useful in ecological research (e.g.

Evans and Cushman, 2009; Martinuzzi et al., 2009; Reese et al., 2014), likely because Random Forest is comparatively (though not perfectly; Dormann et al., 2013) robust to the collinearity often seen among ecological variables.

We used the R package 'randomForest' (Liaw and Wiener, 2002) to build six shrub biomass models that incorporated different combinations (sets) of input data groups (Table 3.3). To ensure that our final models were as parsimonious as possible, we reduced the number of variables included in each model by employing the model selection tool in the R package 'rfUtilities' (Murphy et al., 2010), which examines the relative importance (model improvement ratio, or MIR) of each variable in a Random Forest regression and selects a subset of the most important variables. To reduce uncertainty among collinear variables in this model selection process, we first confirmed that input variables for each model were not highly correlated (Pearson's correlation coefficient < 0.90). Because the stochastic nature of Random Forest can give different results with each execution of the algorithm, we ran the model selection tool 1000 times for each model, and only included predictors in the final Random Forest models if they were chosen in a majority of the variable selection runs. Performance of the final Random Forest regression models was evaluated using the RMSD of the out-of-bag (OOB) training samples and randomForest's 'pseudo R^2', which is a calculation of the percent variance explained by the regression trees (Liaw and Wiener, 2015).

Table 3.3. Predictor sets included in Random Forest variable selection.

Model name	Set(s) of predictors included in model
Canopy only	Lidar-derived canopy metrics
Canopy + spectral	Lidar-derived canopy metrics, spectral metrics
Canopy + topo	Lidar-derived canopy metrics, lidar-derived topographic metrics
Spectral only	Spectral metrics
Spectral + topo	Spectral metrics, lidar-derived topographic metrics
Canopy + spectral + topo	Lidar-derived canopy metrics, spectral metrics, lidar-derived topographic metrics

2.8. Biomass and uncertainty mapping

Biomass predictor rasters were processed using the R package 'raster', and biomass was mapped at 0.80 m across the lidar footprints using the AsciiGridPredict tool in the R package 'yaImpute' (Crookston and Finley, 2007). Because the focus of map production was to identify shrub biomass (even very low-stature shrub biomass) in uneven terrain, we performed no filtering to identify 'unnatural' ground slopes or to mask non-vegetation objects other than roads and large

gravel pads; consequently, the maps contain spurious values for objects on the landscape such as boardwalks and research equipment (e.g. greenhouses and eddy covariance towers). However, these objects are generally recognizable to the human eye based on their linearity or improbable height or position, and can be manually masked in areas of interest if necessary.

We quantified uncertainty in the final shrub biomass map by producing a separate map showing the coefficient of variation (CV) of the Random Forest map estimates. In the final shrub biomass map, the shrub biomass estimate for a given pixel is the mean of all estimates produced by all regression trees for that pixel. By retaining the individual pixel estimates from all trees, we were also able to calculate the standard deviation of each pixel estimate across all trees. Normalizing this per-pixel standard deviation by the per-pixel mean gives the per-pixel coefficient of variation. The resulting CV map spatially illustrates the variation of the model estimates, represented as a percentage of the estimated shrub biomass in each pixel.

3. Results

3.1. The simple model: predicting shrub biomass from lidar-derived canopy volume

Optimized lidar-derived canopy volume was a moderately good single predictor of aboveground shrub biomass. Training model R^2 was 0.60 with an RMSE of 239.5 g m^{-2} (Figure 3.3A). Applying the model to the withheld test dataset gave similar results, producing an R^2 of 0.62 for observed and predicted values, an RMSD of 218.9 g m^{-2}, and a slope and intercept of 1.08 and -71.9 g, respectively (Figure 3.3B).

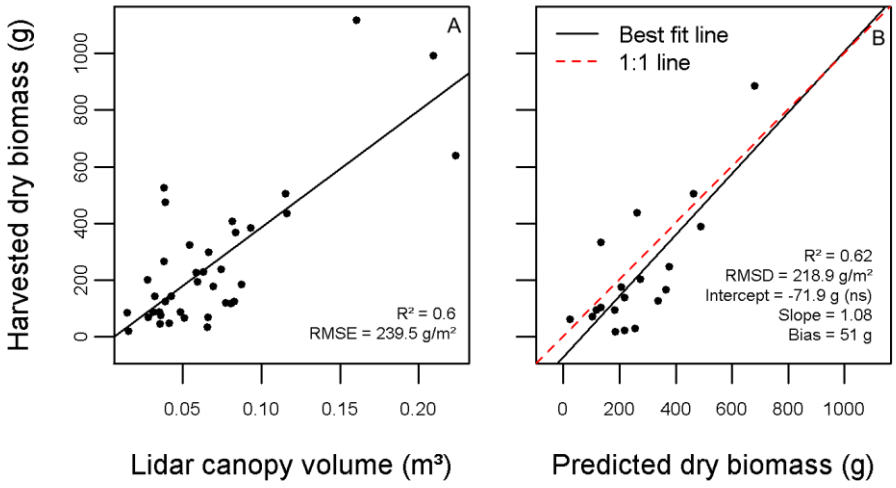

Figure 3.3. Training (A) and test (B) models for aboveground shrub biomass derived from optimized lidar canopy volume. 'ns' means not statistically significant at p = 0.05.

3.2. The complex model: Random Forest regression

3.2.1. Variable selection

The individual predictors selected as important varied depending on the composition of the initial variable set, although there were notable trends (Table 3.4). Lidar-derived optimized canopy volume, maximum canopy height, and mean NDVI aggregated at 2.4 m were selected as important predictors in all models where they were considered. Conversely, several predictors were never identified as important, including vegetation density, topographic hillshade, mean 2GRBi at 2.4 m, and NDVI at 0.8 m. For two of the models—*canopy + topo* and *spectral + topo*—there were predictors selected exactly 50% of the time. This outcome could have been avoided by running the model selection tool an odd number of times; however, then the tie-break would have been entirely arbitrary. Closer examination showed that in the *canopy + topo* model selection, the selected variables always included the same three lidar variables plus *either* SWI *or* MPI. Since it was clearly important to retain one of these two topographic metrics, but it was not clear which, both were retained in the final *canopy + topo* model. On the other hand, in the *spectral + topo* variable selection, the chosen model nearly always included the same set of five predictors, but 50% of the time it also included *both* maximum NDVI at 2.4 m *and* 2GRBI at 0.8 m. Since these two predictors complicated the model but were only considered important 50% of the time, neither was retained in the final predictor set. Interestingly, the predictors selected the majority of the time for the *canopy + spectral + topo* model (the full model) were the same predictors selected for the *canopy + spectral* model: canopy volume, maximum canopy height, standard deviation of maximum height, and mean NDVI at 2.4 m resolution. The only other predictor sometimes selected for the full model was SWI, which was chosen in 44.5% of model selection runs.

Table 3.4. Percent of the time each predictor was selected for each potential Random Forest model, based on 1000 runs of the model selection tool in the R package 'rfUtilities'. Dashes indicate that a predictor was not being considered for a model. Bolded values indicate predictors included in final models.

	Canopy only	*Canopy + spectral*	*Canopy + topo*	*Spectral only*	*Spectral + topo*	*Canopy + spectral + topo*
Canopy volume	**100**	**100**	**100**	-	-	**100**
Vegetation density	0	0	0	-	-	0
Maximum canopy height	**100**	**100**	**100**	-	-	**100**
Standard deviation of height	0	**100**	**100**	-	-	**100**
Maximum NDVI (2.4 m)	-	0	-	**100**	50	0
Mean NDVI (2.4 m)	-	**100**	-	**100**	**100**	**66.7**
NDVI (0.8 m)	-	0	-	0	0	0
Maximum 2GRBI (2.4 m)	-	0	-	**100**	**99.9**	0
Mean 2GRBI (2.4 m)	-	0	-	0	0	0
2GRBI (0.8 m)	-	0	-	**100**	50	0
Topographic position index (TPI)	-	-	0	-	**100**	0
Hillshade	-	-	0	-	0	0
SAGA wetness index (SWI)	-	-	**50**	-	**100**	44.5
Morphometric protection index (MPI)	-	-	**50**	-	**100**	0

3.2.2. Performance of complex models

The best-performing model was *canopy + spectral* (Figure 3.4). Random Forest pseudo R^2 for the best model was 0.71, with RMSD = 197 g m^{-2}. *Canopy + topo* performed nearly as well, with pseudo R^2 = 0.70 and RMSD = 203 g m^{-2}. The *spectral only* model performed worst, with a pseudo R^2 of 0.17 and RMSD of 340 g m^{-2}. Adding topographic predictors to the spectral model improved it slightly: for the *spectral + topo* model, pseudo R^2 was 0.29 and RMSE was 308 g m^{-2}. Slope values were near 1 and absolute bias was 9 g or less for all models except the *spectral only* model, which had a slope of 0.69. Standard deviation of the Random Forest estimates tended to increase with biomass for all models, and was especially large for estimates in the *spectral only* and *spectral + topo* models.

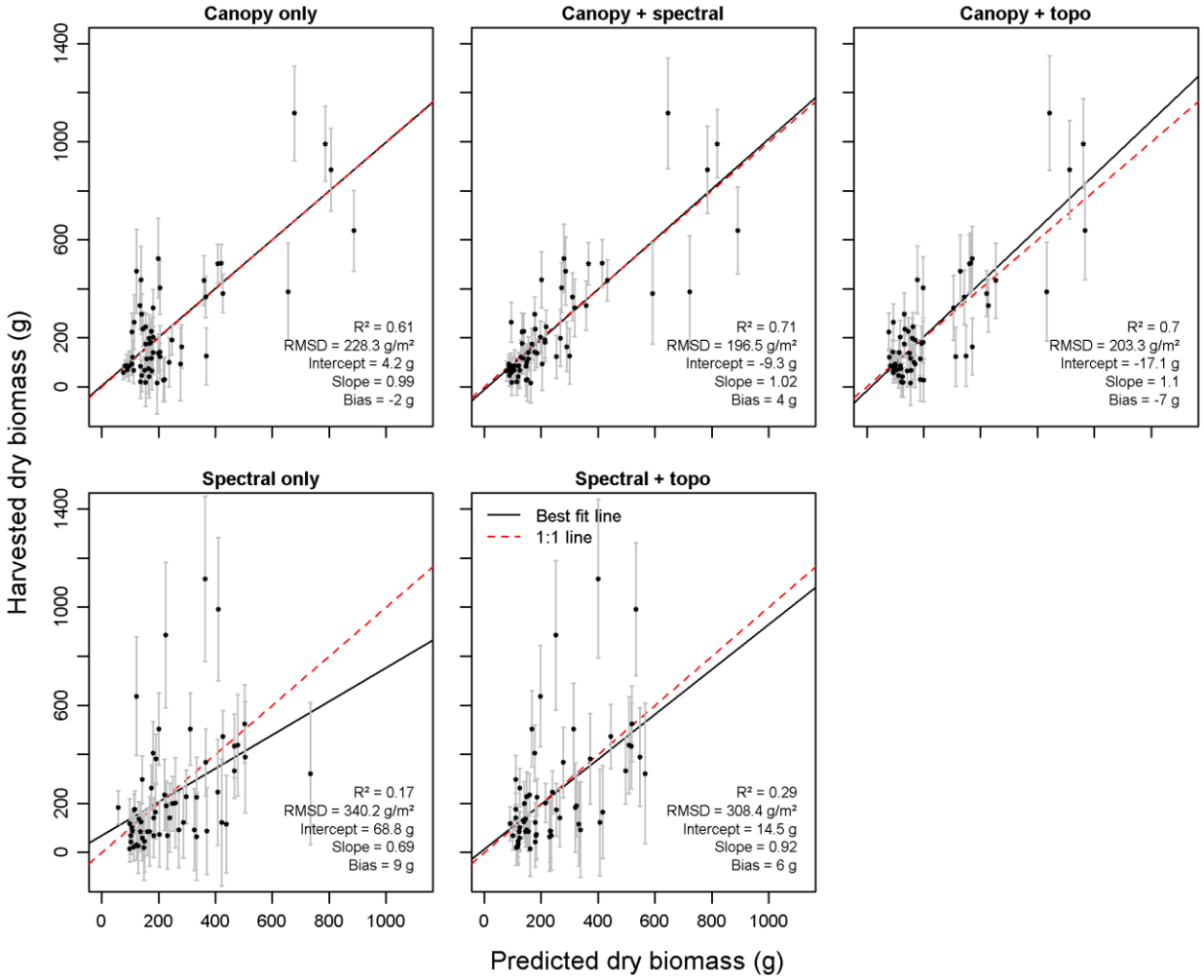

Figure 3.4. Random Forest regression results for models with different predictor sets. Solid black lines are best fit; dotted red lines are 1:1 line. Grey bars are ± one standard deviation. See Table 3.3 for predictors included in each model. The full model (canopy + spectral + topo) is omitted because its selected variables were identical to the canopy + spectral model.

3.3. Aboveground shrub biomass and uncertainty mapping

We used the best Random Forest model, *canopy + spectral*, to map biomass across the three lidar collection footprints. Coarse-scale overview and fine-scale enlarged detail maps of aboveground shrub biomass and two major predictors (lidar-derived canopy volume and NDVI) are shown in Figure 3.5, along with the corresponding detail orthoimage for reference. Lidar-derived canopy volume accurately identifies the largest shrubs in the shrubby watertrack crossing the right-hand side of the detail area, and distinguishes them from surrounding tussocky and heathy areas (Figure 3.5D). NDVI identifies low-volume shrubs such as the 'fringe' of *B. nana* growing on the edges of the watertrack (Figure 3.5E). The final shrub biomass detail map (Figure 3.5C) captures

increasing shrub presence from the heathy upslope area (lower left) to the shrubby downslope watertrack.

Figure 3.6 shows the final shrub biomass map (Figure 3.6A) and the corresponding CV map (Figure 3.6B) for Toolik, the largest lidar collection footprint. As expected, most areas of the landscape have low estimated shrub biomass (Figure 3.6A; Figure 3.7A); standard deviation of shrub biomass tended to increase with shrub biomass up to ~900 g m^{-2}, and then declined (Figure 3.8A). However, coefficient of variation (CV) maps showed that relative to the estimated biomass, uncertainty tended to be highest in areas of low to medium shrub biomass, and low in areas of high shrub biomass (Figure 3.6B; Figure 3.8B). Areas of low shrub biomass also showed the greatest range of uncertainty values (Figure 3.8B). In Figure 3.6A, riparian areas and watertracks are clearly delineated by their high shrub biomass, while low-biomass rocky areas and scoured ridgetops can be differentiated from hillslopes with moderate shrub biomass. In Figure 3.6B, riparian areas and watertracks are similarly visible as areas of very low relative uncertainty, while areas of high uncertainty tend to be concentrated on the hillslope areas with low to medium shrub biomass.

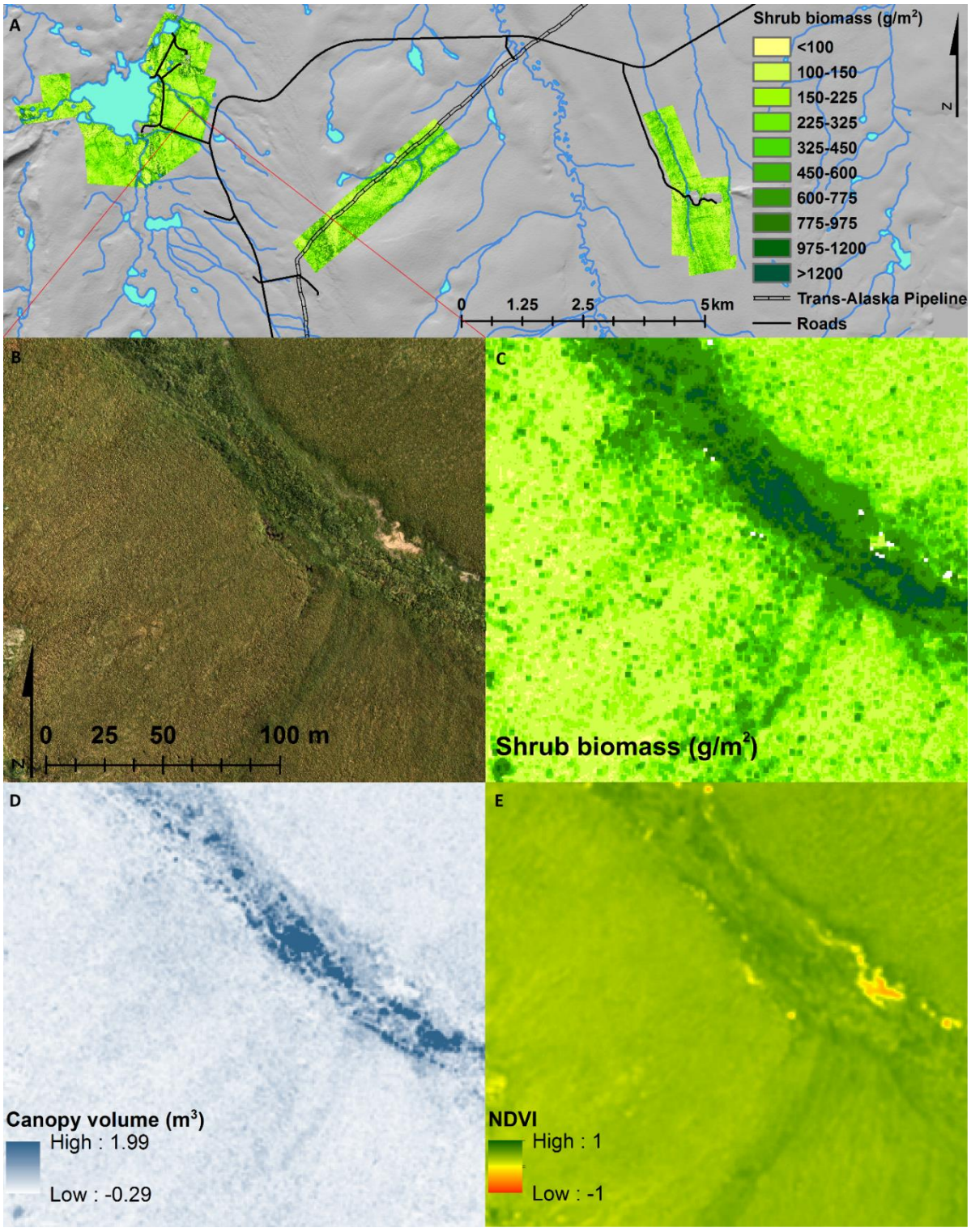

Figure 3.5. A: Overview of shrub biomass maps for the three lidar collection footprints (note biomass color scale is nonlinear). B-E: Enlarged detail view of a representative area showing RGB orthoimage for reference (B), final shrub biomass map (C; color scale is the same as for A), lidar-derived canopy volume (D; shown at native resolution of 0.15 m), and NDVI (E; shown at native resolution of 0.043 m).

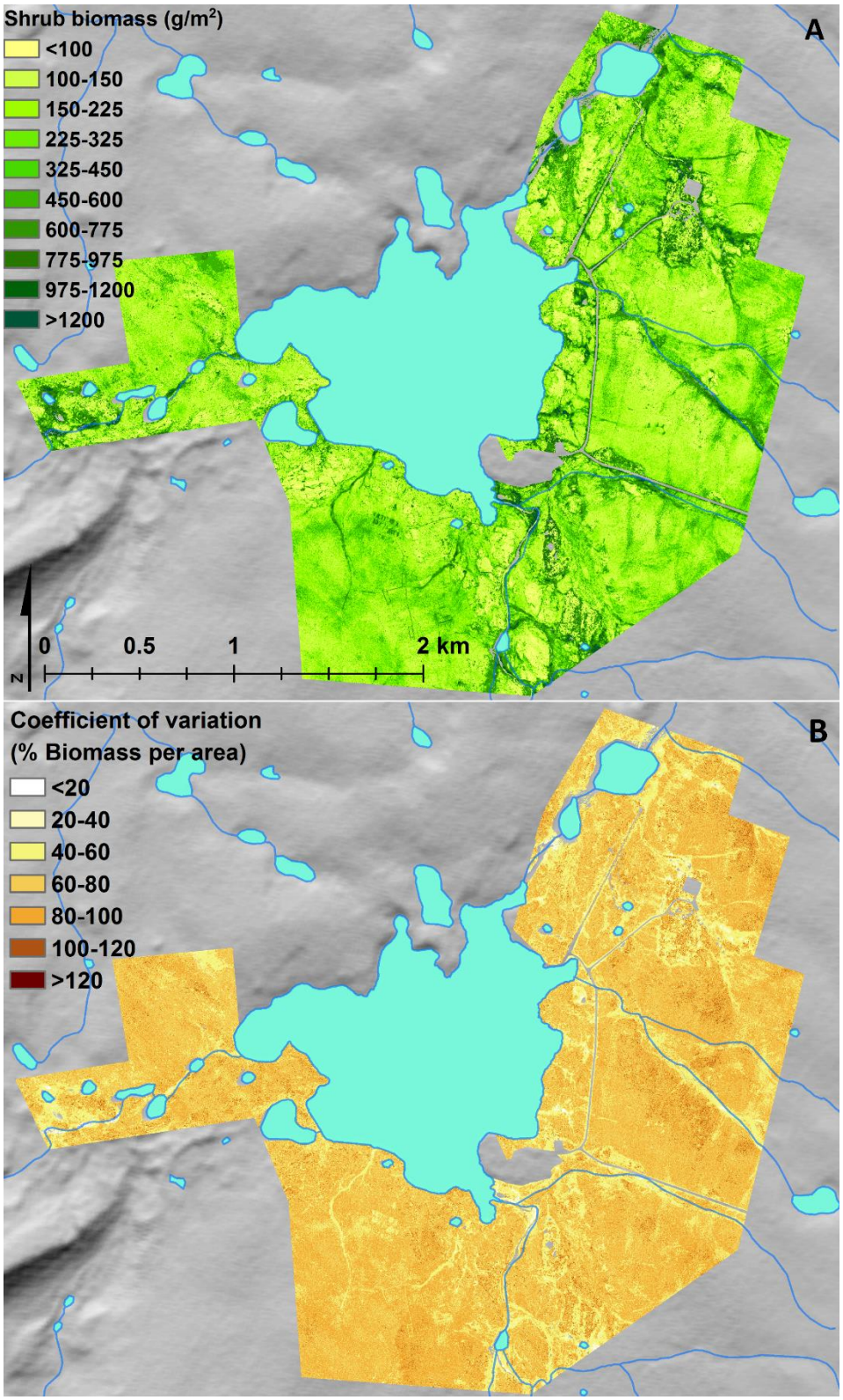

Figure 3.6. Shrub biomass estimates (A) and coefficient of variation of shrub biomass estimates (B) for the Toolik collection footprint.

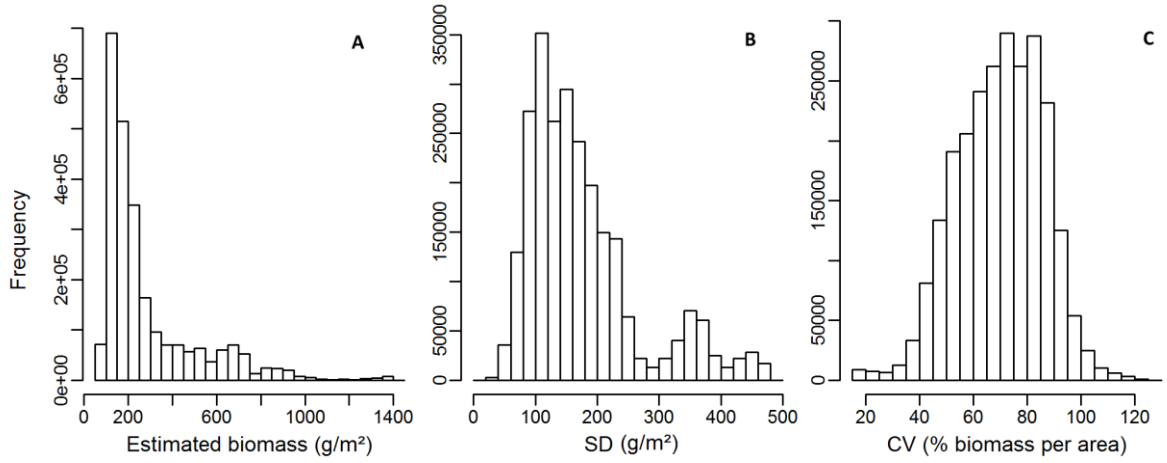

Figure 3.7. Histograms for the Toolik map (see Figure 3.6A) describing the frequency distribution of estimated shrub biomass values (A), standard deviation of shrub biomass estimates (B), and coefficient of variation of shrub biomass estimates (C). Histogram data represent randomly selected pixel locations comprising 10 % of all pixels in the Toolik map (n = 2480184).

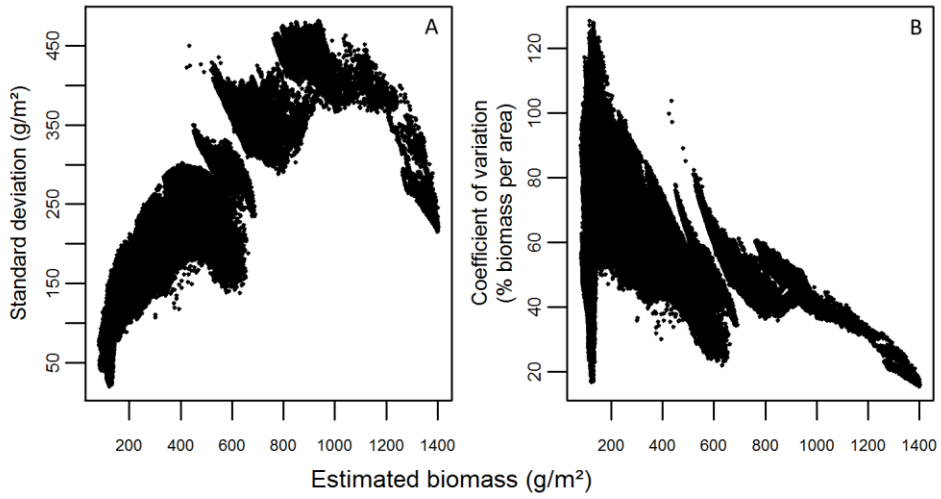

Figure 3.8. Scatterplots for the Toolik map (see Figure 3.6A) showing the relationship between estimated shrub biomass values and the standard deviation (A) and coefficient of variation (B) for those estimates. Scatterplot data represent randomly selected pixel locations comprising 10 % of all pixels in the Toolik map (n = 2480184).

4. Discussion

4.1. Simple vs. complex models for predicting shrub biomass

There are advantages to using canopy volume alone to estimate shrub biomass in a single-predictor regression approach (Figure 3.3), notably the elegance of a single-variable prediction model. Naturally there are also limitations to this simple approach. First, all volumetric approaches to estimating aboveground biomass make the assumption that biomass density is constant—that is,

that a particular volume of canopy always contains a particular quantity of shrub biomass (Greaves et al., 2015; Olsoy et al., 2014). Clearly this assumption is not always accurate; for example in the tundra, windswept rocky areas may host dense banks of shrubs settled in microtopographic hollows—these would fall above the line of best fit in Figure 3.3, with relatively high biomass but low volume. Also, reference data only included harvested biomass of shrubs >5 cm height, ignoring all shorter shrub stems, as well as graminoids and forbs that occurred in these plots—even if these were taller than 5 cm—which somewhat confounds shrub biomass density calculations. But despite these limitations, the simple canopy volume regression approach produced acceptable estimates of shrub biomass in a challenging low-stature tundra landscape. Furthermore, if shrubs continue to increase in height and abundance in the tundra, high-resolution lidar-derived canopy volume may prove to be a vegetation metric sensitive enough to detect and measure such changes.

In addition to canopy volume, the best Random Forest model (*canopy + spectral*) also included maximum canopy height, standard deviation of maximum canopy height, and NDVI. Although the Random Forest variable selection procedure always indicated that the two additional lidar-derived canopy metrics (maximum canopy height and standard deviation of maximum canopy height) were important, they did not improve the model much by themselves. This can be seen by comparing the single-predictor model (Figure 3.3) and results for the *canopy only* Random Forest model (Figure 3.4): adding these two lidar canopy metrics to the single-predictor canopy volume model produced virtually no change (and potentially a slight worsening) in the resulting R^2 (0.62 vs 0.61) and RMSD (219 g m^{-2} vs. 228 g m^{-2}). This suggests that these canopy variables may have been retained in the Random Forest variable selection only because they were too highly correlated to be separated, despite our precautions. For simplicity in future model-building, a stricter correlation threshold could be employed.

Conversely, adding spectral predictors clearly improved estimates of shrub biomass, decreasing RMSD by ~30 g m^{-2} and increasing R^2 by ~ 0.10 (Figure 3.4), which broadly agrees with results found in other low-stature ecosystems. For example, Riaño et al. (2007) found that incorporating an NDVI-based correction into lidar-derived estimates of shrub height improved model R^2 from 0.48 to 0.65. Similarly, Estornell et al. (2012) compared models for estimating shrub biomass and found that adding spectral metrics to lidar improved R^2 from 0.67 to 0.79. By incorporating greenness in our model, the NDVI metric likely improved biomass estimates in high-biomass, low-lying shrub banks, which may have low volume but display high greenness. Furthermore, the addition of the NDVI spectral predictor appears to especially improve shrub

biomass estimates in plots with low to medium shrub biomass (i.e. harvest plots with less than ~400 g harvested biomass; compare *canopy only* and *canopy + spectral* in Figure 3.4). Because vegetation communities with low shrub biomass are widespread on tundra landscapes, it seems warranted to use the more complicated model for the sake of improved accuracy in these areas.

4.2. Spectral metrics: implications for scale and change detection

We were somewhat surprised to find that NDVI was only an important predictor of shrub biomass when it was aggregated over a coarser resolution (2.4 m) than the lidar data (0.80 m pixel). This may have been due to simple georegistration error, although GPS spot-checks we performed suggested that the lidar and imagery datasets were accurately co-registered to within approximately 10 cm. Still, together with the relatively poor performance of the *spectral only* model (even with four spectral predictors retained), this suggests that the value of NDVI as a predictor may be limited in very high-resolution (~1 m pixel) applications. At moderate to coarse resolution, NDVI is a very strong predictor of aboveground biomass in tundra (e.g. Raynolds et al., 2012; R^2 = 0.94 for 1+ km pixels), but previous work does suggest that this relationship can break down at higher resolutions (an effect not limited to NDVI; see e.g. Costanza and Maxwell, 1994). For example, Shippert et al. (1995) found that field- and satellite-derived NDVI predicted biomass very well across tundra vegetation groups if those groups were very broadly defined (e.g. wet, dry, shrub), but was a relatively poor predictor when those groups were separated into their component communities, or into the individual samples for those communities. This poor performance may indicate localized saturation of NDVI values, reflectance from woody stems diluting NDVI signals for large shrubs (Boelman et al., 2011), or species-specific variation in NDVI response (as we noticed during preliminary analysis, discussed in section 2.6.); additional investigation might clarify the mechanisms at work.

Still, the importance of spectral data for improving estimates of shrub biomass in our study reinforces the complementary nature of structural (lidar) and spectral datasets. The benefits of including airborne imagery datasets likely overbalance the challenges posed by varying environmental and technical collection specifications that make these datasets less repeatable, and make comparison across multiple datasets challenging. Satellite imagery data, although more susceptible to atmospheric variations than airborne data (e.g. opportunistic data acquisitions during clear skies are not possible), are also subject to more standardized correction and calibration algorithms that render them more comparable over time. However, high-resolution imagery (~ 2 m pixel or less) tends to be expensive, whether acquired from airborne or commercial satellite sources.

(We note that lidar acquisitions are also quite expensive.) Still, we hope that continuing advances in remote sensing technologies may soon permit widespread access to very high-resolution satellite datasets that can improve vegetation mapping in highly heterogeneous ecosystems like Arctic tundra.

Our second-best model, *canopy + topo*, was nearly as good as the *canopy + spectral* model, which suggests that the spectral and topographic data contributed similar information—especially given that adding topographic data to the spectral data (in the *spectral + topo* model) only somewhat improved the *spectral only* model (Figure 3.4). Reese et al. (2014) found that certain individual Random Forest predictors (e.g. NDVI, SWI, 95th percentile lidar heights) were important for predicting the presence of individual alpine vegetation types; in our case, a similar effect may be occurring in which both spectral and topographic data improve prediction in areas with low shrub biomass, while lidar-derived canopy metrics are uniquely able to capture the structural signature of larger high-biomass vegetation. Topographic metrics may also contribute underlying information regarding ecological niches in which particular species occur: for example, Martinuzzi et al. (2009) found that a topographic metric representing exposure was important for predicting the presence of understory shrubs in a temperate forest system. In any case, the strong performance of the *canopy + topo* model suggests that at least in tundra ecosystems, lidar-derived topographic data may be sufficient to improve lidar-derived aboveground biomass estimates if adequate spectral data are unavailable.

4.3. Shrub biomass maps

The shrub biomass maps created in this study represent high-resolution estimates of current aboveground shrub biomass across a widely studied research landscape in the American Arctic. We have also provided a means to assess the accuracy and validity of these maps by performing leave-one-out cross-validation for our main predictor and testing the resulting prediction relationship against a withheld dataset, and by providing out-of-bag error estimates and uncertainty maps for our final model. The estimates of shrub biomass on the final shrub biomass map tended to be of similar range but slightly lower than previous mapped estimates of total biomass found in maps by Shippert et al. (1995) and Walker and Maier (2007), which is reasonable given that our estimates only include shrub biomass and exclude biomass of mosses, forbs, and graminoids. If anything, the range of shrub biomass values on our maps seems somewhat compressed, with fewer very low or very high mapped values than might be expected, which may reflect limitations in our harvest plot selection. Indeed, our harvest plots did not include samples of the largest common shrub species

(*Salix alaxensis*), partly because previous research suggests that such large shrub species occupy less than 3% of the overall tundra landscape (Beck et al., 2011). On the other hand, our shrub biomass maps capture a wider gradient of shrub cover and structure relative to previous work in this ecosystem. Space-based spectral techniques have been used to distinguish between tall riparian shrubs (>1m) with LAI $\geq$ 1 (e.g. *S. alaxensis*) and short stature (<0.5 m) dwarf shrubs in tussock tundra with lower LAI (Beck et al., 2011; Selkowitz, 2010), but those techniques have not permitted mapping variation in shrub stature beyond these two discrete groups.

The optimized canopy volume map (Figure 3.5D), in addition to being an important predictor for shrub biomass, is itself a valuable high-resolution (0.15 m) spatial record of vegetation canopy structure within the three footprints of the lidar data collection. It also has the advantage of being a more direct, physically based representation of the landscape than the Random Forest-derived shrub biomass map, and consequently may indeed prove more valuable for change detection and monitoring over time than estimates of shrub biomass derived from more complex models.

5. Conclusions

This study presents a robust approach for using airborne lidar data and high-resolution airborne imagery to accurately map low-stature shrub biomass in Arctic tundra. Simple lidar-derived canopy volume produced reasonable predictions of shrub biomass, but the accuracy of predictions was improved by including additional predictors (particularly NDVI) alongside lidar-derived canopy volume in a Random Forest regression approach. The high-resolution shrub biomass maps produced in this study are a valuable baseline reference that will be useful to researchers seeking to understand tundra vegetation dynamics, or to improve estimates of carbon flux, nutrient cycling, and wildlife habitat in the rapidly changing tundra biome.

Acknowledgements

This work was supported by NASA Terrestrial Ecology grant NNX12AK83G, NASA Earth Science Fellowship NNX15AP04H awarded to HEG, and NASA Idaho Space Grant Fellowship NNX10AM75H awarded to TSM. Airborne lidar and imagery data were collected by Kodiak Mapping, Inc., Palmer, AK, www.kodiakmapping.com. Field assistance from Moyo Ajayi, Rebecca Gibson, and Elizabeth Fortin was greatly appreciated. The authors are also grateful for the support of the staff and greater research community of Toolik Field Station, Institute of Arctic Biology, University of Alaska Fairbanks, with special thanks to Jason Stuckey, Randy Fulweber, and Jorge Noguera of Toolik

GIS for assistance with GPS and lidar ground control. This manuscript was improved by constructive comments from three anonymous reviewers.

References

Bater, C. W., Wulder, M. A., Coops, N. C., Nelson, R. F., Hilker, T., & Næsset, E. (2011). Stability of sample-based scanning-LiDAR-derived vegetation metrics for forest monitoring. IEEE Transactions on Geoscience and Remote Sensing, 49(6 PART 2), 2385–2392. doi:10.1109/TGRS.2010.2099232

Beck, P. S. A., Horning, N., Goetz, S. J., Loranty, M. M., & Tape, K. D. (2011). Shrub cover on the North Slope of Alaska: a circa 2000 baseline map. Arctic, Antarctic, and Alpine Research, 43(3), 355–363. doi:10.1657/1938-4246-43.3.355

Blok, D., Heijmans, M. M. P. D., Schaepman-Strub, G., Kononov, A. V., Maximov, T. C., & Berendse, F. (2010). Shrub expansion may reduce summer permafrost thaw in Siberian tundra. Global Change Biology, 16, 1296–1305. doi:10.1111/j.1365-2486.2009.02110.x

Boelman, N., Gough, L., Wingfield, J., Goetz, S. J., Asmus, A., Chmura, H., … Guay, K. (2014). Greater shrub dominance alters breeding habitat and food resources for migratory songbirds in Alaskan arctic tundra. Global Change Biology. doi:10.1111/gcb.12761

Boelman, N. T., Gough, L., McLaren, J. R., & Greaves, H. (2011). Does NDVI reflect variation in the structural attributes associated with increasing shrub dominance in arctic tundra? Environmental Research Letters, 6(3), 035501. doi:10.1088/1748-9326/6/3/035501

Breiman, L. (2001). Random forests. Machine Learning, 45, 5–32. doi:10.1023/A:1010933404324

Chapin, F. S. I., Sturm, M., Serreze, M. C., McFadden, J. P., Key, J. R., Lloyd, A. H., … Welker, J. M. (2005). Role of land-surface changes in arctic summer warming. Science, 310, 657–60. doi:10.1126/science.1117368

Costanza, R., & Maxwell, T. (1994). Resolution and predictability: An approach to the scaling problem. Landscape Ecology, 9(1), 47–57. doi:10.1007/BF00135078

Crookston, N. L., & Finley, A. O. (2007). yaImpute: An R Package for k-NN Imputation. Journal of Statistical Software, 23(10), 1–16.

Dalponte, M., Bruzzone, L., & Gianelle, D. (2008). Fusion of Hyperspectral and LIDAR Remote Sensing Data for Classification of Complex Forest Areas. IEEE Transactions on Geoscience and Remote Sensing, 46(5), 1416–1427. doi:10.1109/TGRS.2008.916480

Dormann, C. F., Elith, J., Bacher, S., Buchmann, C., Carl, G., Carré, G., … Lautenbach, S. (2013). Collinearity: A review of methods to deal with it and a simulation study evaluating their performance. Ecography, 36(1), 027–046. doi:10.1111/j.1600-0587.2012.07348.x

Dubayah, R. O., & Drake, J. B. (2000). Lidar remote sensing for forestry. Journal of Forestry, 98(6), 44–46.

Ducks Unlimited. (2013). North Slope Science Initiative Landcover Mapping Summary Report.

Duguay, Y., Bernier, M., Lévesque, E., & Tremblay, B. (2015). Potential of C and X Band SAR for Shrub Growth Monitoring in Sub-Arctic Environments. Remote Sensing, 7(7), 9410–9430. doi:10.3390/rs70709410

Eitel, J. U. H., Magney, T. S., Vierling, L. A., Brown, T. T., & Huggins, D. R. (2014). LiDAR based biomass and crop nitrogen estimates for rapid, non-destructive assessment of wheat nitrogen status. Field Crops Research, 159, 21–32. doi:10.1016/j.fcr.2014.01.008

Estornell, J., Ruiz, L. A., Velázquez-Martí, B., & Fernández-Sarría, A. (2011). Estimation of shrub biomass by airborne LiDAR data in small forest stands. Forest Ecology and Management, 262(9), 1697–1703. doi:10.1016/j.foreco.2011.07.026

Estornell, J., Ruiz, L. A., Velazquez-Marti, B., & Hermosilla, T. (2012). Estimation of biomass and volume of shrub vegetation using LiDAR and spectral data in a Mediterranean environment. Biomass and Bioenergy, 46, 710–721. doi:10.1016/j.biombioe.2012.06.023

Evans, J. S., & Cushman, S. A. (2009). Gradient modeling of conifer species using random forests. Landscape Ecology, 24(5), 673–683. doi:10.1007/s10980-009-9341-0

Goswami, S., Gamon, J. A., & Tweedie, C. E. (2011). Surface hydrology of an arctic ecosystem: Multiscale analysis of a flooding and draining experiment using spectral reflectance. Journal of Geophysical Research, 116(January), G00I07. doi:10.1029/2010JG001346

Greaves, H. E., Vierling, L. A., Eitel, J. U. H., Boelman, N. T., Magney, T. S., Prager, C. M., & Griffin, K. L. (2015). Estimating aboveground biomass and leaf area of low-stature Arctic shrubs with terrestrial LiDAR. Remote Sensing of Environment, 164, 26–35. doi:10.1016/j.rse.2015.02.023

Hijmans, R. J. (2015). raster: Geographic Data Analysis and Modeling. R package version 2.3-40. http://CRAN.R-project.org/package=raster.

Hladik, C., Schalles, J., & Alber, M. (2013). Salt marsh elevation and habitat mapping using hyperspectral and LIDAR data. Remote Sensing of Environment, 139, 318–330. doi:10.1016/j.rse.2013.08.003

Hudak, A. T., Strand, E. K., Vierling, L. A., Byrne, J. C., Eitel, J. U. H., Martinuzzi, S., & Falkowski, M. J. (2012). Quantifying aboveground forest carbon pools and fluxes from repeat LiDAR surveys. Remote Sensing of Environment, 123, 25–40. doi:10.1016/j.rse.2012.02.023

Hyde, P., Dubayah, R., Walker, W., Blair, J. B., Hofton, M., & Hunsaker, C. (2006). Mapping forest structure for wildlife habitat analysis using multi-sensor (LiDAR, SAR/InSAR, ETM+, Quickbird) synergy. Remote Sensing of Environment, 102, 63–73. doi:10.1016/j.rse.2006.01.021

Isenburg, M. (2015). LAStools - Efficient tools for lidar processing. Version 140329. http://lastools.org.

Jones, B. M., Stoker, J. M., Gibbs, A. E., Grosse, G., Romanovsky, V. E., Douglas, T. A., … Richmond, B. M. (2013). Quantifying landscape change in an arctic coastal lowland using repeat airborne LiDAR. Environmental Research Letters, 8(4), 045025. doi:10.1088/1748-9326/8/4/045025

Kim, Y., Yang, Z., Cohen, W. B., Pflugmacher, D., Lauver, C. L., & Vankat, J. L. (2009). Distinguishing between live and dead standing tree biomass on the North Rim of Grand Canyon National Park, USA using small-footprint lidar data. Remote Sensing of Environment, 113(11), 2499–2510. doi:10.1016/j.rse.2009.07.010

Lantz, T. C., Gergel, S. E., & Kokelj, S. V. (2010). Spatial Heterogeneity in the Shrub Tundra Ecotone in the Mackenzie Delta Region, Northwest Territories: Implications for Arctic Environmental Change. Ecosystems, 13(2), 194–204. doi:10.1007/s10021-009-9310-0

Lawrence, D. M., & Swenson, S. C. (2011). Permafrost response to increasing Arctic shrub abundance depends on the relative influence of shrubs on local soil cooling versus large-scale climate warming. Environmental Research Letters, 6(4). doi:10.1088/1748-9326/6/4/045504

Liaw, A., & Wiener, M. (2002). Classification and Regression by randomForest. R News, 2(December), 18–22. doi:10.1177/154405910408300516

Liaw, A., & Wiener, M. (2015). R Package “randomForest”: Breiman and Cutler’s Random Forests for Classification and Regression. Retrieved January 1, 2016, from https://cran.r-project.org/web/packages/randomForest/randomForest.pdf

Loranty, M. M., & Goetz, S. J. (2012). Shrub expansion and climate feedbacks in Arctic tundra. Environmental Research Letters, 7(1). doi:10.1088/1748-9326/7/1/011005

Mack, M. C., Schuur, E. A. G., Bret-Harte, M. S., Shaver, G. R., & Chapin, F. S. (2004). Ecosystem carbon storage in arctic tundra reduced by long-term nutrient fertilization. Nature, 431(7007), 440–3. doi:10.1038/nature02887

Martinuzzi, S., Vierling, L. A., Gould, W. A., Falkowski, M. J., Evans, J. S., Hudak, A. T., & Vierling, K. T. (2009). Mapping snags and understory shrubs for a LiDAR-based assessment of wildlife habitat suitability. Remote Sensing of Environment, 113(12), 2533–2546. doi:10.1016/j.rse.2009.07.002

Muller, S. V., Racoviteanu, A. E., & Walker, D. A. (1999). Landsat MSS-derived land-cover map of northern Alaska: Extrapolation methods and a comparison with photo-interpreted and AVHRR-derived maps. International Journal of Remote Sensing, 20(15-16), 2921–2946. doi:10.1080/014311699211543

Mundt, J. T., Streutker, D. R., & Glenn, N. F. (2006). Mapping Sagebrush Distribution Using Fusion of Hyperspectral and Lidar Classifications. Photogrammetric Engineering Remote Sensing, 72(1), 47–54. doi:10.14358/PERS.72.1.47

Murphy, M. A., Evans, J. S., & Storfer, A. (2010). Quantifying Bufo boreas connectivity in Yellowstone National Park with landscape genetics. Ecology, 91(1), 252–261. doi:10.1890/08-0879.1

Myers-Smith, I. H., Elmendorf, S. C., Beck, P. S. a., Wilmking, M., Hallinger, M., Blok, D., … Vellend, M. (2015). Climate sensitivity of shrub growth across the tundra biome. Nature Climate Change, (July). doi:10.1038/nclimate2697

Myers-Smith, I. H., Forbes, B. C., Wilmking, M., Hallinger, M., Lantz, T., Blok, D., … Hik, D. S. (2011). Shrub expansion in tundra ecosystems: dynamics, impacts and research priorities. Environmental Research Letters, 6(4). doi:10.1088/1748-9326/6/4/045509

Naito, A. T., & Cairns, D. M. (2015). Patterns of shrub expansion in Alaskan arctic river corridors suggest phase transition. Ecology and Evolution, 5(1), 87–101. doi:10.1002/ece3.1341

Olsoy, P. J., Glenn, N. F., Clark, P. E., & Derryberry, D. R. (2014). Aboveground total and green biomass of dryland shrub derived from terrestrial laser scanning. ISPRS Journal of Photogrammetry and Remote Sensing, 88, 166–173. doi:10.1016/j.isprsjprs.2013.12.006

Pineiro, G., Perelman, S., Guerschman, J. P., & Paruelo, J. M. (2008). How to evaluate models: Observed vs. predicted or predicted vs. observed? Ecological Modelling, 216, 316–322. doi:10.1016/j.ecolmodel.2008.05.06

R Core Team. (2015). R: A language and environment for statistical computing. R Foundation for Statistical Computing. Vienna, Austria. URL http://www.R-Project.org/.

Raynolds, M. K., Walker, D. A., Epstein, H. E., Pinzon, J. E., & Tucker, C. J. (2012). A new estimate of tundra-biome phytomass from trans-Arctic field data and AVHRR NDVI. Remote Sensing Letters, 3(5), 403–411. doi:10.1080/01431161.2011.609188

Raynolds, M. K., Walker, D. a., & Maier, H. a. (2005). Plant community-level mapping of arctic Alaska based on the circumpolar arctic vegetation map. Phytocoenologia, 35(4), 821–848. doi:10.1127/0340-269X/2005/0035-0821

Raynolds, M. K., Walker, D. A., Munger, C. A., Vonlanthen, C. M., & Kade, A. N. (2008). A map analysis of patterned-ground along a North American Arctic Transect. Journal of Geophysical Research: Biogeosciences, 113(G3), G03S03. doi:10.1029/2007JG000512

Rees, W. (2007). Characterisation of Arctic treelines by LiDAR and multispectral imagery. Polar Record, 43(227), 345–352. doi:10.1017/S0032247407006511

Reese, H., Nyström, M., Nordkvist, K., & Olsson, H. (2014). Combining airborne laser scanning data and optical satellite data for classification of alpine vegetation. International Journal of Applied Earth Observation and Geoinformation, 27, 81–90. doi:10.1016/j.jag.2013.05.003

Riaño, D., Chuvieco, E., Ustin, S. L., Salas, J., Rodríguez-Pérez, J. R., Ribeiro, L. M., … Fernández, H. (2007). Estimation of shrub height for fuel-type mapping combining airborne LiDAR and simultaneous color infrared ortho imaging. International Journal of Wildland Fire, 16(3), 341. doi:10.1071/WF06003

Rich, M. E., Gough, L., & Boelman, N. T. (2013). Arctic arthropod assemblages in habitats of differing shrub dominance. Ecography, 36(December 2012). doi:10.1111/j.1600-0587.2012.00078.x

Richardson, A. D., Jenkins, J. P., Braswell, B. H., Hollinger, D. Y., Ollinger, S. V., & Smith, M. L. (2007). Use of digital webcam images to track spring green-up in a deciduous broadleaf forest. Oecologia, 152, 323–334. doi:10.1007/s00442-006-0657-z

Ritchie, J. C., Seyfried, M. S., Chopping, M. J., & Pachepsky, Y. (2001). Airborne LASER technology for measuring rangeland conditions. Journal of Range Management, 54, A8–A21.

Schimel, J. P., Bilbrough, C., & Welker, J. M. (2004). Increased snow depth affects microbial activity and nitrogen mineralization in two Arctic tundra communities. Soil Biology and Biochemistry, 36(2), 217–227. doi:10.1016/j.soilbio.2003.09.008

Selkowitz, D. J. (2010). A comparison of multi-spectral, multi-angular, and multi-temporal remote sensing datasets for fractional shrub canopy mapping in Arctic Alaska. Remote Sensing of Environment, 114(7), 1338–1352. doi:10.1016/j.rse.2010.01.012

Shippert, M. M., Walker, D. A., Auerbach, N. A., & Lewis, B. E. (1995). Biomass and leaf-area index maps derived from SPOT images for Toolik Lake and Imnavait Creek areas, Alaska. Polar Record, 31(177), 147–154.

Simms, É., & Ward, H. (2013). Multisensor NDVI-based monitoring of the tundra-taiga interface (Mealy Mountains, Labrador, Canada). Remote Sensing, 5(3), 1066–1090. doi:10.3390/rs5031066

Stow, D. A., Hope, A., McGuire, D., Verbyla, D., Gamon, J., Huemmrich, F., … Myneni, R. (2004). Remote sensing of vegetation and land-cover change in Arctic Tundra Ecosystems. Remote Sensing of Environment, 89(3), 281–308. doi:10.1016/j.rse.2003.10.018

Streutker, D. R., & Glenn, N. F. (2006). LiDAR measurement of sagebrush steppe vegetation heights. Remote Sensing of Environment, 102(1-2), 135–145. doi:10.1016/j.rse.2006.02.011

Tao, S., Guo, Q., Li, L., Xue, B., Kelly, M., Li, W., … Su, Y. (2014). Airborne Lidar-derived volume metrics for aboveground biomass estimation: A comparative assessment for conifer stands. Agricultural and Forest Meteorology, 198-199, 24–32. doi:10.1016/j.agrformet.2014.07.008

Tape, K., Sturm, M., & Racine, C. (2006). The evidence for shrub expansion in Northern Alaska and the Pan-Arctic. Global Change Biology, 12(4), 686–702. doi:10.1111/j.1365-2486.2006.01128.x

Vierling, L. A., Eitel, J. U. H., Boelman, N. T., Griffin, K. L., Greaves, H., Magney, T. S., … Gibson, R. (2013a). Bare earth LiDAR dataset for Toolik Field Station, AK, and nearby field sites along Dalton Highway. doi:10.7923/G4057CV5.

Vierling, L. A., Eitel, J. U. H., Boelman, N. T., Griffin, K. L., Greaves, H., Magney, T. S., … Gibson, R. (2013b). Four-band, 5cm resolution orthophotographs of Toolik Field Station, AK, and nearby field sites along Dalton Highway. Doi: 10.7923/G4VD6WCW.

Vierling, L. A., Xu, Y., Eitel, J. U. H., & Oldow, J. S. (2012). Shrub characterization using terrestrial laser scanning and implications for airborne LiDAR assessment. Canadian Journal of Remote Sensing, 38(6), 709–722.

Walker, D. A., & Maier, H. A. (2007). Geobotanical maps in the vicinity of the Toolik Lake Field Station, Alaska. Institute of Arctic Biology, Biological Papers of the University of Alaska, No. 27.

Walker, D. A., Raynolds, M. K., Daniëls, F. J., Einarsson, E., Elvebakk, A., Gould, W. A., … CAVM Team. (2005). The Circumpolar Arctic vegetation map. Journal of Vegetation Science, 16, 267–282.

Walker, M. D., Walker, D. A., & Auerbach, N. A. (1994). Plant communities of a tussock tundra landscape in the Brooks Range foothills, Alaska. Journal of Vegetation Science, 5(6), 843–866.

Yokoyama, R., Shirasawa, M., & Pike, R. (2002). Visualizing topography by openness: A new application of image processing to digital elevation models. Photogrammetric Engineering and Remote Sensing, 68(3), 257–266.

Zolkos, S. G., Goetz, S. J., & Dubayah, R. (2013). A meta-analysis of terrestrial aboveground biomass estimation using lidar remote sensing. Remote Sensing of Environment, 128, 289–298. doi:10.1016/j.rse.2012.10.017

CHAPTER 4: MAPPING ARCTIC TUNDRA VEGETATION AT SUB-METER RESOLUTION WITH AIRBORNE LIDAR AND MULTISPECTRAL IMAGERY

Abstract

Multi-scale landcover maps are necessary to support research into the ongoing impacts of climate change in Arctic regions. Commonly available coarse-scale, broad extent maps provide valuable general descriptions of landcover, but accurately depicting the heterogeneous nature of tundra vegetation communities requires very high resolution raster maps, ideally with 5 m pixel size or less. Such high-resolution maps provide valuable local information for validation of coarser maps, as well as permitting characterization of fine scale landscape phenomena like songbird habitat suitability. In this study, we used 33 predictor layers derived from airborne lidar and high-resolution (~5 cm) 4-band airborne imagery to build vegetation community maps at 20 cm resolution for three landscapes (12.5 km^2 total) near the Toolik Lake research area in the Alaskan Low Arctic. The maps were predicted from a Random Forest model that was trained and tested on 800 ground reference plots, with classes derived from the commonly used legends on the hierarchy of polygon-based maps available from the Alaska Geobotany Center. Withheld test plots had a balanced accuracy of 0.57, kappa of 0.47, and weighted (fuzzy) kappa of 0.65. With training plots included, balanced accuracy was 0.89, kappa was 0.85, and weighted kappa was 0.89. These maps represent valuable, validated, very high resolution information that can serve as baseline data for vegetation monitoring and change detection as well as valuable reference data for researchers working in the area.

1. Introduction

As the Arctic continues to warm rapidly (ACIA, 2005), research efforts seeking to improve understanding of potential impacts on human, animal, and vegetation communities are becoming increasingly urgent. At the root of many remaining uncertainties is a need to understand the distribution of some feature across the landscape—for example, to understand how much area is covered by lakes and wetlands that may be releasing increasing quantities of methane (Walter et al., 2007), or which permafrost slopes might be at risk for unexpected thaw, potentially impacting local and downstream terrestrial and aquatic communities and releasing ancient soil carbon to the atmosphere (Osterkamp, 2005). Some of these uncertainties involve ecological interactions at very fine scales, such as understanding the area of suitable nesting habitat for a migratory songbird that requires open, dry hillsides (Boelman et al., 2014).

Remote sensing has enabled mapping of Arctic landscapes (Stow et al., 2004) at a range of resolutions and extents. Broad extent, coarse to moderate resolution maps provide valuable general information to researchers about surface features (e.g. Beck et al., 2011; Walker et al., 2005), and can be important inputs to regional and global climate models (Oechel et al., 2000), but the coarse- to moderate spatial resolution of these mainly satellite-data-derived maps cannot describe the heterogeneity of Arctic landscapes accurately enough to provide information on fine-scale ecological phenomena like songbird habitat (Boelman et al., 2014). Capturing the natural variability of Arctic tundra surfaces across complex environmental gradients requires surface mapping at very high resolution, generally 5 m or less (Atkinson and Treitz, 2012; Davidson et al., 2016; Langford et al., 2016).

In this project, we sought to create very high resolution vegetation classification maps for important research areas near Toolik Lake, in the Alaskan Low Arctic. This area has benefited from previous mapping efforts, in particular by the Alaska Geobotany Center at the University of Alaska, Fairbanks, which has produced a spatially hierarchical series of maps for the area depicting multiple surface features, including vegetation maps (http://www.arcticatlas.org), which provided a valuable benchmark for this project. Vegetation classes on the maps were determined using the Braun-Blanquet classification approach (Braun-Blanquet, 1965; Walker et al., 1994), in which species associations are grouped into a hierarchy of successively broader units. The classification system has the potential to precisely describe the finely heterogeneous vegetation of the Toolik Lake area, but the maps are polygon-based, with variable minimum mapping units (the small-extent maps have the smallest minimum mapping units, 2.5 m^2) and therefore tend to blur and oversimplify the distribution and arrangement of vegetation patches on the landscape.

Using predictor layers derived from airborne lidar and imagery, we trained a Random Forest model to predict vegetation communities across three research areas near Toolik Lake (12.5 km^2 total) at 20 cm resolution. We believe these maps will provide valuable support to researchers working in the area who require detailed information on vegetation distribution or habitat suitability, as well as researchers seeking to validate coarser maps or plan future research efforts.

2. Methods

2.1. Study area

The study was conducted near the Arctic Long Term Ecological Research site at Toolik Lake (Alaska, USA, 68°38’ N latitude, 149°36’ W longitude; Figure 4.1). Located on continuous permafrost tundra in the northern foothills of the Brooks Range, the Toolik area has been an important site for

North American Low Arctic research since the 1970s. The region is characterized by cold winters (mean coldest month temperature -30°C) and mild summers (mean warmest month temperature 13°C), with roughly 300 mm of precipitation annually (Huryn and Hobbie, 2012). Complex topography, glacial features, and prevailing weather patterns (notably scouring southerly winds) generate a complex mosaic of microenvironmental gradients of parent material, exposure, and drainage, which in turn host a finely heterogeneous patchwork of tundra vegetation communities. The dominant vegetation is graminoid tundra (especially *Eriophorum vaginatum* and *Carex Bigelowii*) with abundant *Sphagnum* mosses and erect deciduous shrubs, mainly *Betula nana* and *Salix* species.

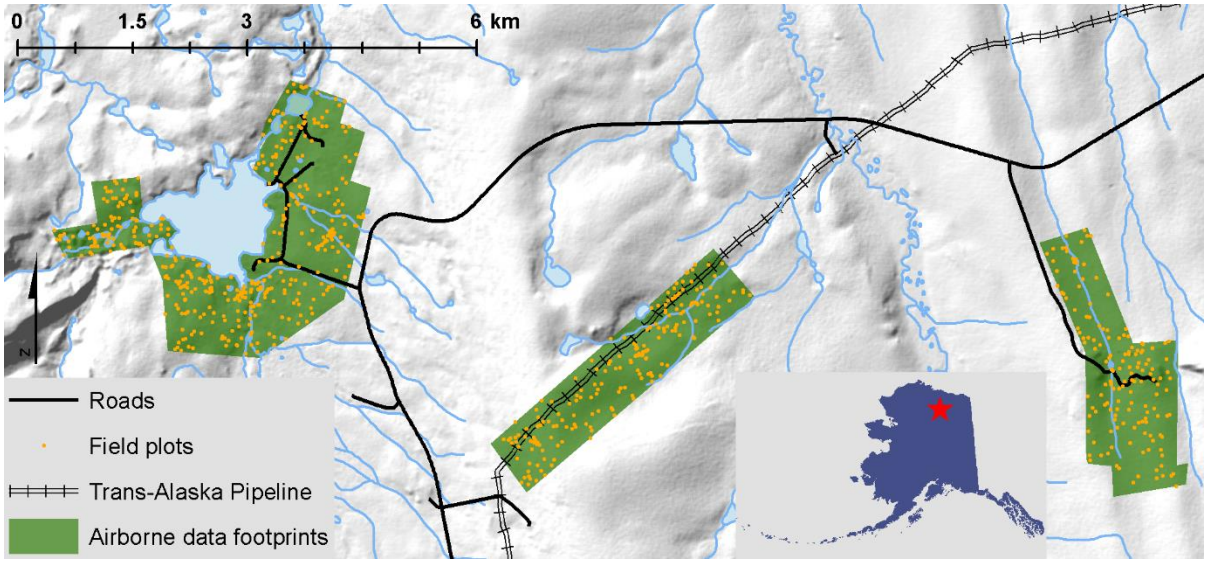

Figure 4.1. Airborne data collection footprints (in green; from left: Toolik, Pipeline, Imnavait) and locations of reference plots (orange dots). Inset map shows the general location of the study area in Alaska.

2.2. Data collection

2.2.1. Airborne data collection

Airborne lidar and high-resolution digital imagery were collected August 1st, 2013. Data were collected in three discrete footprints totaling 12.5 km^2 (Figure 4.1; Vierling et al., 2013a, 2013b). The largest and westernmost footprint (hereafter 'Toolik', ~6 km^2) covers research areas near Toolik Field Station at Toolik Lake. The other two footprints are each roughly 3 km^2: the 'Pipeline' footprint (~3 km east of Toolik Lake) follows a stretch of the Trans-Alaska Pipeline from a high moraine ridge down a sloping drainage toward the Kuparuk River; the 'Imnavait' footprint includes research areas along Imnavait Creek, roughly 10 km east of Toolik Lake. Lidar collection specifications are shown in Table 4.1. The vendor performed pre-processing of the lidar data,

including aircraft attitude adjustments and ground control georectification. Simultaneous 4-band digital imagery (RGB and near infrared, hereafter 'RGBN') was collected by a Leica RCD30 60MP camera mounted to the aircraft. The imagery was orthorectified by the vendor and delivered as orthoimagery mosaics with a pixel resolution of 4.25 cm. A GPS check of 40 stationary objects distributed across the Toolik footprint suggested that the imagery was accurately orthorectified to within ~10 cm.

Table 4.1. Lidar collection specifications.

Instrument	Riegl VQ-480i
Scanner type	Onboard waveform processing yielding multiple discrete returns
Wavelength	1550 nm
Beam divergence	0.3 milliradians
Flight altitude	365 m above ground level
Vertical / Horizontal accuracy	8-10 cm / ~10 cm
Spot size (laser beam ground footprint)	11 cm
Nominal flight line return density	13.5 points m^{-2}
Nominal aggregated return density	27 points m^{-2}

2.2.2. Reference plot photo collection

Field reference data were collected from across all footprints in summer 2014 and summer 2015. The majority of plot locations (592) were established in advance using a stratified random scheme to ensure inclusion of a full range of slope, aspect, elevation, and glacial history across all footprints. An additional 47 plots were placed subjectively in the course of visiting the pre-placed plots, to capture a wider range of shrub characteristics, and 92 more plots were collected in 2015 to represent additional shrub types and topographic transects. For these 731 total field plots, we took nadir photographs from approximately 1 m height with a standard point-and-shoot digital camera, capturing roughly 1 m x 1.3 m of ground. We also recorded brief notes regarding the plant species and surface features present in the plot and the general area, including vegetation height, thaw depth, and moss/organic soil mat depth. The center coordinates of each plot photo were measured with a TopCon GR-3 survey grade GNSS system operating in real-time kinematic (RTK) mode (nominal accuracy 4 cm).

2.2.3 Reference plot photo classification

Since it was desirable that the final map classes correspond as well as possible with legends used on previous maps, potential classes were created by examining communities described in available maps and literature, especially Walker and Barry (1991), Walker, Walker, and Auerbach (1994), Walker and Walker (1996), Raynolds, Walker, and Maier (2005), and the related hierarchy of maps created by the Alaska Geobotany Center at University of Alaska Fairbanks, especially Walker and Maier (2007). To assign each plot photo (i.e. each plot location) to a plant community, photo order was randomized and each photo was visually examined. Based on plant species and other features visible in the photo, as well as plot notes, each plot location was assigned to the class that best described the center of the photo where the coordinates had been measured. It wasn't yet clear how well we would be able to distinguish vegetation classes in the final maps, so initial class assignments were as granular as possible, to permit more flexible subsequent grouping. Finally, 69 additional plots were identified in the orthophotos to provide more reference data for gravel pads, blockfields (rock), and water – classes that were underrepresented in the field data and could be easily identified in the orthophotos.

2.3. Input data layer processing

A total of 33 input data layers at 20 cm resolution were derived from the airborne lidar and RGBN imagery using a variety of tools (Table 4.2). Most layers fall into three general categories: lidar-derived canopy metrics (e.g. sum and standard deviation of canopy heights), lidar-derived topographic metrics (e.g. topographic position index, SAGA wetness index), and first-order imagery metrics (e.g. NDVI, percent red, standard deviation of hue). Additionally, there is one compound layer, shrub biomass, which was previously derived from lidar canopy metrics and NDVI (Greaves et al., 2016). We also included lidar return intensity (pulse amplitude), which acts as a surface metric (Chust et al., 2008; Lang and McCarty, 2009). The raw intensity of the near-infrared laser return is affected by surface characteristics, especially wetness (water absorbs the laser pulse, leading to low return intensity in wet areas) and surface roughness (relatively smooth areas may reflect the pulse more strongly), making it a potentially valuable predictor of surface features and vegetation distribution (Eitel et al., 2016). Although our intensity data is not radiometrically calibrated or normalized (Yan and Shaker, 2014), the nonparametric nature of the Random Forest modeling approach permits the inclusion of such raw data. All predictor metrics were selected to be ecologically meaningful for arctic vegetation distribution as well as being likely to improve prediction

of vegetation characteristics based on previous work (e.g. Dirnböck et al., 2003; Greaves et al., 2016; Kushida et al., 2015; Naito and Cairns, 2011; Ohmann and Gregory, 2002).

Owing to the large amount of noise present at such a high resolution, most layers were smoothed using a circular mean Focal Statistics filter (Spatial Analyst in ArcGIS, ESRI, Redlands CA). This type of smoothing retains the original spatial resolution, but tends to improve classification predictions (e.g. Gottfried et al., 2014) by decreasing meaningless local variation, instrument noise, and small shadows. Once the layers were prepared, the values of all predictor layers at the location of each reference plot were extracted for model training. We initially processed layers at several smoothing distances (0.5 m, 0.75 m, 1 m, 1.25 m), but retained only layers that appeared important in preliminary models and had a Spearman correlation less than 0.95 for the reference plot locations.

Table 4.2. Input layers.

Variable	Variable type	Description [1]
biomass	Compound	Estimated shrub biomass (Greaves et al., 2016)
cnht_sd	Canopy	Standard deviation of canopy height within 1 m radius of pixel [2]
cnht_sm05	Canopy	Sum of canopy height (corresponds to canopy volume) within 0.5 m [2]
cnht_sm1	Canopy	Sum of canopy height within 1 m radius [2]
dsi_05	Imagery	Deciduous shrub index (Kushida et al., 2015) smoothed at 0.5 m [3]
dsi_1	Imagery	Deciduous shrub index smoothed at 1 m radius [3]
dtm_sd	Topographic	Standard deviation of terrain height within 1 m radius [2]
dtm	Topographic	Absolute terrain height [2]
hli_05	Topographic	Heat load index (McCune and Keon, 2002) [4]
hue_1	Imagery	Hue smoothed at 1 m radius [5]
hue_sd	Imagery	Standard deviation of hue within 1 m radius [5]
int	Surface	Mean raw intensity of lidar pulse return within pixel [6]
int_1	Surface	Raw intensity of lidar pulse return smoothed at 1 m radius [6]
int_sd	Surface	Standard deviation of raw intensity of lidar pulse return within 1 m [6]
ndvi_05	Imagery	NDVI smoothed at 0.5 m radius [3]
ndvi_1	Imagery	NDVI smoothed at 1 m radius [3]
pan_1	Imagery	Panchromatic (R + G + B) smoothed at 1 m radius [3]
pan_sd	Imagery	Standard deviation of panchromatic within 1 m radius [3]
pctb_1	Imagery	Percent blue (B/[R + G + B]) smoothed at 1 m radius [3]
pctr_1	Imagery	Percent red (R/[R + G + B]) smoothed at 1 m radius [3]
site	Topographic	Site name: Toolik Lake, Pipeline Ridge, or Imnavait Creek
swi_05	Topographic	SAGA Wetness Index (Boehner et al., 2002) smoothed at 0.5 m [7]
swi_1	Topographic	SAGA Wetness Index smoothed at 1 m radius [7]
tpi_5	Topographic	Topographic Position Index calculated at 5 m radius [4]
tpi_10	Topographic	Topographic Position Index calculated at 10 m radius [4]
tpi_25	Topographic	Topographic Position Index calculated at 25 m radius [4]
tpi_50	Topographic	Topographic Position Index calculated at 50 m radius [4]
tpi_100	Topographic	Topographic Position Index calculated at 100 m radius [4]
tpi_250	Topographic	Topographic Position Index calculated at 250 m radius [4]
ws_05	Topographic	SAGA wind shelter (Plattner et al., 2004) smoothed at 0.5 m radius [7]
ws_1	Topographic	SAGA wind shelter smoothed at 1 m radius [7]
2grbi_05	Imagery	Excess greenness index (Richardson et al., 2007) smoothed at 0.5 m [3]
2grbi_1	Imagery	Excess greenness index smoothed at 0.5 m radius [3]

[1] Smoothing, summing, and standard deviations performed using ArcGIS (ESRI, Redlands, CA) Focal Statistics in Spatial Analyst via arcpy in Python (Python Software Foundation version 2.7, www.python.org)

[2] Canopy and terrain heights estimated from lidar as described in Greaves et al. (2017)

[3] Calculated from RGBN imagery via the 'raster' package (Hijmans, 2015) in R (R Core Team, 2017)

[4] Implemented using the Geomorphometry and Gradient Analysis Toolbox for ArcGIS (Evans et al., 2014) via arcpy in Python

[5] Hue derived from RGBN imagery via ENVI (Exelis Visual Information Solutions, Boulder, Colorado)

[6] Raw intensity gridded using LAStools (Isenburg, 2017)

[7] Implemented in SAGA GIS (Conrad et al., 2015) via the 'RSAGA' package (Brenning, 2008) in R

2.4. Random Forest modeling

Random Forest (Breiman, 2001) is a machine learning algorithm that uses ensembles ('forests') of classification or regression trees. In a Random Forest, each tree selects and permutes random subsets of predictor variables at each splitting node, which reduces overfitting and improves the strength of predictions. Additionally, Random Forest is non-parametric, naturally models local interactions, and is relatively robust (but not perfectly; Dormann et al., 2013) to the collinearity common to ecological variables, making it an important tool for ecological research (e.g. Evans and Cushman, 2009; Martinuzzi et al., 2009; Reese et al., 2014).

We used the package 'caret' (Kuhn, 2016) with the package 'randomForest' (Liaw and Wiener, 2002) in the R statistical language (R Core Team, 2017) to build and train the Random Forest classification model. Twenty-five percent of the reference data plots (selected proportionally from each class; n = 196 plots total) were withheld from model building to be used as a test dataset; the remaining 75% of the plots (n = 604) were used to train the model.

Since the Random Forest algorithm strives to produce the best overall accuracy, it is susceptible to producing poor accuracy for small classes in imbalanced datasets. Since our input dataset was imbalanced, we used an upsampling algorithm implemented in the caret package to ensure equal weighting of each class (Chen et al., 2004). The model building was an iterative process: we used out-of-bag accuracy and confusion matrices from early models to determine which classes could not realistically be differentiated, then collapsed input classes accordingly (Table S4.1) and retrained the model, seeking the best possible balance between accuracy and retention of informative classes. The final class names and reference plot membership counts are in Table 4.3. We also tuned the number of trees and the number of variables randomly selected for splitting at each tree node (mtry) in the Random Forest model. We found that any number of trees greater than ~500 and any value of mtry less than approximately 6 gave comparable results; the final model used 1001 trees and an mtry of 1.

Table 4.3. Final class names and counts for all reference data.

Class name	Count
Barren	28
Rock	24
Dry exposed tundra	52
Dry Sheltered Tundra	45
Low dense shrub	47
Moist snowbed	61
Tussock tundra	100
Shrubby tussock tundra	57
Moist non-tussock tundra	112
Shrubby moist non-tussock tundra	79
Low to tall moist shrub	84
Tall shrub	17
Raised areas in wet tundra	43
Wet tundra	17
Water	34

2.5. Mapping

After building the final Random Forest model, we applied it across the three data collection footprints using the AsciiGridPredict tool in the R package 'yaImpute' (Crookston and Finley, 2007). In post-processing, pixels in class patches smaller than 25 pixels (i.e. 1 m^2; a queen relationship was allowed) were replaced by the surrounding class majority, making the minimum mapping unit 1 m^2 of area. After extracting the final mapped class for each reference plot location, the map was evaluated using both the withheld test data and the complete reference dataset by examining the overall accuracy, balanced accuracy (i.e. the mean class-wise accuracy), Cohen's kappa, and Cohen's weighted kappa (Cohen, 1968). Like Cohen's kappa, Cohen's weighted kappa quantifies the overall agreement after accounting for agreement by chance, but it additionally permits the investigator to indicate the degree of disagreement present. Since vegetation community classes are discrete labels meant to represent gradients of species abundance and structure, it is reasonable to treat certain disagreements between classes more or less seriously than others. For example, for most applications it would be considerably less serious to confuse Tussock Tundra with Moist Non-Tussock Tundra, or with Shrubby Tussock Tundra, than it would be to confuse it with Dry Exposed Tundra or Tall Shrub. The weights matrix we used to calculate weighted kappa is in Table S4.2.

3. Results and Discussion

3.1. Description of final map classes

These descriptions are intended to aid in interpreting the maps. They include a general description of the surfaces and vegetation in areas covered by the class; comments on other classes that may be confused with the class based on the ecology or geography of the class, as well as its performance in the model confusion matrices (Tables 4.4 and 4.5); the estimated range of canopy heights (for shrubby classes only) based on lidar-derived 2.5^{th} to 97.5^{th} height percentiles for the class; and notes regarding how the class relates to the map legends used in the Alaska Geobotany Center maps. Specific class references are made to the comparatively granular Toolik Lake Grid ('TLG') vegetation map (Walker and Maier, 2007).

Barren – This class contains mainly flat anthropogenic barrens such as roads, gravel pads, and gravel pits, and corresponds to the 'Anthropogenic barren' class on the TLG map.

Rock – Includes blockfields and other areas of exposed lichen-covered rock or bare uneven gravelly soil. This class also tends to capture structures on the landscape, including buildings, greenhouses, vehicles, boardwalks, large equipment installations, and the Trans-Alaska Pipeline. It corresponds to the 'Lichen on rock' and 'Partially vegetated barren' classes in the TLG map. (The anthropogenic structures may be manually separated from this class prior to map publication.)

Dry exposed tundra – Includes dry (well-drained) tundra communities characterized by prostrate shrubs such as (in acidic areas) *Dryas octopetala*, *Arctous alpina*, *Salix phlebophylla*, or *Vaccinium vitis-idaea*, or (in non-acidic areas) *Dryas integrifolia*. These areas are generally level to south-facing and are locally topographically elevated and exposed to sun and wind scour; consequently they have minimal winter snow accumulation and gravelly soils that drain well and thaw rapidly and deeply. This class would tend to intergrade with Barren and Rock classes (at the more exposed extreme) or with the Dry Sheltered Tundra or Low Dense Shrub classes (at the slightly moister and more sheltered extreme). This class includes the classes 'Prostrate dwarf-shrub (acidic)', 'Prostrate dwarf-shrub (*Dryas octopetala*)', and 'Prostrate dwarf-shrub (*Dryas integrifolia*)' from the TLG map.

Dry Sheltered Tundra – This includes well-drained areas that are somewhat more topographically sheltered than Dry Exposed Tundra, such as small depressions on dry ridges and terraces or drier strips of shallow snowbeds in upland tundra classes. Dry Sheltered Tundra may have considerable exposed soil cover but also support graminoids and prostrate- to hemi-prostrate shrubs including *Ledum palustre*, *Vaccinium uliginosum*, or *Empetrum nigrum*, as well as potentially

abundant fruticose lichens, but relatively few mosses. This class intergrades somewhat with the Dry Exposed Tundra class, the Low Dense Shrub class (which has denser, more even shrub cover), and the Moist Snowbed class (which is moister, with more abundant mosses). This class most closely matches the TLG 'Hemi-prostrate dwarf-shrub (snowbed < 1m)' class, but it also includes some more sheltered areas described as one of the 'Prostrate dwarf-shrub' classes on the TLG map.

Low Dense Shrub – This class primarily indicates the presence of dense hemi-prostrate to low-erect shrubs (roughly 5-30 cm in height), characteristic of stable, relatively sheltered locations on warm, well-drained soils. *Betula nana* is the most common dominant, but patches of *Vaccinium uliginosum* and other hemi-prostrate to low-erect species are also included. This class is generally found as small hemi-prostrate patches in sheltered areas amid Dry Exposed Tundra, or as continuous low erect shrubfields on well-drained terraces. In a few moister areas (especially in level areas) there is some class confusion between this class and the Low to Tall Moist Shrub class; differentiation between these classes may not be meaningful in these areas. This class most closely corresponds to the TLG class 'Hemi-prostrate dwarf-shrub (warm snowbed)'.

Moist Snowbed – This class represents topographically well-sheltered areas with good to moderate drainage and moister soils than the Dry Sheltered Tundra class. It includes north-facing areas below well-drained Dry Exposed Tundra or Dry Sheltered Tundra areas, as well as moister strips of shallow snowbeds found in sheltered areas of Tussock Tundra or Moist Non-Tussock Tundra. Moist Snowbeds are characterized by relatively abundant *Cassiope tetragona* along with other hemi-prostrate to low-erect shrub species, and have considerably greater moss cover (and lower bare soil cover) than the Dry Sheltered Tundra class. The Moist Snowbed class is sometimes confused with Dry Exposed Tundra on the drier end of its gradient and with other moist tundra classes (especially Tussock Tundra and Moist Non-Tussock Tundra) on the wetter/more poorly drained end of its gradient. It corresponds most closely with the TLG classes 'Hemi-prostrate dwarf-shrub (acidic)' and 'Hemi-prostrate dwarf-shrub (nonacidic)'.

Tussock Tundra – This class represents communities dominated mostly by *Eriophorum vaginatum*, which are usually moderately drained, moderately sheltered, shallowly sloped areas with stable acidic soils. Naturally, this common class covers a range of 'shrubbiness' and 'tussocky-ness', so it tends to intergrade with other moist upland tundra classes, especially with Shrubby Tussock Tundra, Moist Non-Tussock Tundra, Moist Snowbed, and Shrubby Moist Non-Tussock Tundra. It corresponds to portions of the TLG class 'Tussock-sedge' dominated by *Eriophorum vaginatum*.

Shrubby Tussock Tundra – Indicates areas of tussock tundra with considerable shrub cover (approximately 10-25 cm in height), especially where *Eriophorum vaginatum* may share dominance with erect shrub species *Betula nana* or *Salix pulchra*, but also including *Vaccinium uliginosum*, *Ledum palustre*, or other shrub species. This class is sometimes confused with the other moist upland tundra classes, especially Tussock Tundra and Shrubby Moist Non-Tussock Tundra. It corresponds to the portions of the TLG class 'Tussock-sedge' co-dominated by *Eriophorum vaginatum* and erect deciduous shrubs, and to areas of 'Dwarf to low-shrub' willow and birch subtypes that have a significant *Eriophorum vaginatum* component.

Moist Non-Tussock Tundra – This class includes moderately drained, moderately sheltered areas of sedge-dominated tundra without a dominant *Eriophorum vaginatum* component. In acidic areas, this usually indicates somewhat steeper or otherwise less stable upland areas than areas of Tussock Tundra. It also includes non-acidic sedge-dominated tundra with *Dryas integrifolia*. This class is essentially the ecological 'default' of the upland moist tundra classes, and as such it intergrades and is confused with most other upland moist tundra classes, especially Tussock Tundra (in more stable areas) and Moist Snowbed (in more sheltered areas). It corresponds to portions of the acidic TLG class 'Tussock-sedge' that are not dominated by *Eriophorum vaginatum*, as well as to the non-acidic 'Nontussock-sedge' classes, including the 'horsetail' and '*Cassiope*' subtypes.

Shrubby Moist Non-Tussock Tundra – Includes areas of moderately drained, moderately sheltered moist upland tundra dominated by low (roughly 5-25 cm height) erect shrubs of various species. This class is frequently assigned to shrubbier moist interstripe areas on non-sorted stripes, as well as shrubby moist upland areas not directly associated with watertracks or riparian areas. It is the most frequently confused class, since it naturally intergrades with Moist Non-Tussock Tundra, Shrubby Tussock Tundra, and Low to Tall Moist Shrub. The class most closely corresponds with the areas in the TLG 'Dwarf to low-shrub' birch and willow subtypes that do not have a strong *Eriophorum vaginatum* component.

Low to Tall Moist Shrub – This class describes very moist areas with taller erect shrubs (~10-100 cm height), usually *Betula nana* or *Salix* spp., especially in relation to watertracks and riparian corridors. These areas generally have deep moss cover and abundant *Rubus chamaemorus* with otherwise rare forb species, or significant *Eriophorum angustifolium* (in well-developed watertracks). The class also includes some shrub-adjacent riparian areas that were too small or too poorly represented in the data to be modeled well, such as streamside communities with abundant *Salix chamissonis*, or forbs like *Aconitum delphinifolium* and *Ranunculus* spp. As might be expected,

this class tends to be confused with other shrubby classes, especially Shrubby Moist Non-Tussock Tundra and Low Dense Shrub (especially in level, well-drained riparian areas). It most closely corresponds to the TLG 'Low to tall shrublands' birch, willow, and watertrack subtypes.

Tall Shrub – This class describes areas with especially tall (~30-200+ cm height) deciduous shrubs, often *Salix* spp. in large, well-developed watertracks or riparian areas, or on disturbed gravel areas. It also includes a small grove of poplar trees found on a steep south-facing slope in the extreme western end of the Toolik footprint. The class is sometimes confused with the Low to Tall Moist Shrub class, and corresponds mainly to the TLG class 'Low to tall shrublands (riparian)'.

Raised Areas in Wet Tundra – This class includes mainly hummocks and other near-saturated but somewhat elevated locations, especially poorly drained areas dominated by mosses, with creeping *Salix fuscescens* and other fen-associated species. The hummocky structure of these areas can lead to map confusion with taller moist vegetation, especially Low to Tall Moist Shrub, and they also tend to intergrade with Moist Non-Tussock Tundra and Wet Tundra. This class most closely corresponds with the TLG class 'Sedge-moss tundra (poor fens)', particularly to the 'Hummocks, strangs and raised microsites' subtype.

Wet Tundra – Describes wet sedge tundra, which occurs in low-lying, poorly drained, saturated areas and may be characterized by *Carex aquatilis* and *Eriophorum angustifolium*. Wet Tundra naturally intergrades with Moist Non-Tussock Tundra and Raised Areas in Wet Tundra; it most closely corresponds with the sedge-dominated portions of the TLG 'Sedge-moss tundra' fen and poor fen subtypes.

Water – Includes all areas entirely covered by surface water, including very sparsely vegetated inundated sedge tundra and herbaceous marshes that occur in shallow water on pond and lake margins. This class corresponds to the TLG classes 'Unvegetated water' and 'Herbaceous marsh'.

3.2. Model evaluation

For the withheld test plots, overall accuracy was 0.52, balanced (mean class-wise) accuracy was 0.57, and kappa was 0.47, indicating moderate agreement; however, weighted kappa was considerably higher (0.65), suggesting that many of the disagreements were relatively minor. The confusion matrix (Table 4.4) demonstrates that the main confusion was among shrubby classes (e.g. Shrubby Moist Non-Tussock Tundra and Low to Tall Moist Shrub) and among moist upland classes (e.g. Tussock Tundra and Moist Non-Tussock Tundra), which is unsurprising since these classes tend to grade into each other in reality. User's accuracy was higher overall than producer's accuracy

(mean 0.63 vs 0.57). The confusion matrix also illustrates that although the withheld test data represented 25% of all reference data, the imbalanced class sizes led to quite small withheld sample sizes for some classes (as small as 4 members, mean 13); this makes the accuracy metrics somewhat difficult to interpret, since there were relatively few opportunities to test accuracy in these smaller classes.

Many sources of error potentially contributed to uncertainty in the withheld test plot predictions. For example, the gradient nature of all vegetation communities can make class assignment of an arbitrary plot location ambiguous, since a given location may show characteristics of multiple vegetation communities. This could lead to, for example, two similar plots being assigned to different classes based on a potentially arbitrary metric, such as the relative abundance of *Cassiope tetragona* in a given plot, which could add noise to the training data.

The 20 cm resolution likely also contributed considerably to classification uncertainty, especially in the context of such a finely heterogeneous landscape. At such a high resolution, unavoidable sub-meter errors in data collection and processing become unusually important: small artifacts from imagery stitching and orthorectification; minor spatial variations in lidar ground-control adjustments; centimeter-level errors in GNSS base station location or RTK corrections; and slight mismatches in the location of the reference plot photo and the measurement of the plot coordinates can all easily displace a field reference plot from its proper input layer pixel onto a pixel that may better represent a neighboring vegetation community, introducing additional noise in the training data. Indeed, the noticeable difference between the value for kappa (0.47) and weighted kappa (0.65) suggests that many misclassifications may be attributable to small ecological (gradient-related) or locational variations in the data.

When considering all 800 reference plots (including both training and test data), kappa was 0.86, and weighted kappa was 0.89, indicating a high degree of agreement (Table 4.5). The discrepancy between accuracy values for the withheld and complete datasets suggests some overfitting in the Random Forest model, although the high agreement over the larger dataset still demonstrates that the model could predict accurately over a wide range of input data.

Although the Random Forest approach is valuable for its flexibility and robustness, it provides only limited options for ecological interpretation of results. For example, it is possible to derive variable importance metrics by examining how much the accuracy (class-wise and overall) changes when the model is run iteratively with the values of each variable permuted (i.e. randomly reordered among plots). However, variable importance values become less meaningful when input

variables are highly correlated (Nicodemus et al., 2010), as in this study, so it is probably not advisable to interpret the variable importance rigorously. Nevertheless, some results are interesting (Table S4.3). For example, lidar intensity was important for several classes, with standard deviation of intensity especially important for very wet vegetated classes (Raised Areas in Wet Tundra, Wet Tundra), where the occurrence of intermixed high and low intensity pixels could indicate an area of intermixed vegetation and saturated microsites. Intensity smoothed at 1 m was the variable with the largest impact on the overall Gini purity index, and was especially important for very dry vegetated classes (Dry Exposed Tundra, Dry Sheltered Tundra) where intensity would be high, and for Water, where intensity would be extremely low. Greenness indices (NDVI, DSI, 2GRBI) were unsurprisingly important for predicting all shrubby classes, but coarse-scale topographic position was also important for predicting Shrubby Moist Non-Tussock Tundra and Low to Tall Moist Shrub. It was not surprising that lidar-derived canopy height metrics were important for predicting Tall Shrub, or that heat load index was important for Moist Snowbed, but it was somewhat surprising that percent red appeared so important for predicting wet tundra classes (Wet Tundra, Raised Areas in Wet Tundra) and moist upland tundra classes (Moist snowbed, Tussock Tundra, Moist Non-Tussock Tundra). It was also interesting that the standard deviation of the panchromatic (R + G + B), although not at all important for the majority of classes, was highly important for predicting Tussock Tundra, where high values may have indicated the presence of tussock shadows, as well as Water, where values would be low. Overall, in a list of 15 most important variables per class, all 33 predictors appear for at least one class; in a list of the five most important variables per class, only seven predictors *fail* to appear for at least one class (hue_sd, swi_05, swi_1, ws_05, ws_1, tpi_25, and tpi_50). Although this likely is due in part to the correlated nature of many of the predictor variables, the wide variety of variables appearing as important for different classes also reflects the complicated interrelationships between vegetation communities and their ecological predictors.

Table 4.4. Confusion matrix and accuracy metrics including only withheld test plots.

Mapped \ Reference:	Barren	Rock	Dry exposed tundra	Dry Sheltered Tundra	Low dense shrub	Moist snowbed	Tussock tundra	Shrubby tussock tundra	Moist non-tussock tundra	Shrubby moist non-tussock tundra	Low to tall moist shrub	Tall shrub	Raised areas in wet tundra	Wet tundra	Water	Total plots	User's accuracy
Barren	7	-	-	-	-	-	-	-	-	-	-	-	-	-	-	7	1.00
Rock	-	5	-	-	-	-	-	-	-	-	-	-	-	-	-	5	1.00
Dry exposed tundra	-	1	10	3	-	1	-	-	-	-	-	-	-	-	-	15	0.67
Dry Sheltered Tundra	-	-	2	6	-	-	-	-	1	1	1	-	-	-	-	11	0.55
Low dense shrub	-	-	-	1	5	-	-	-	1	-	2	-	-	-	-	9	0.56
Moist snowbed	-	-	2	-	1	6	-	-	3	-	-	-	-	-	-	12	0.50
Tussock tundra	-	-	-	-	-	2	12	8	6	2	1	-	-	-	-	31	0.39
Shrubby tussock tundra	-	-	-	-	-	-	1	6	-	2	-	-	-	-	-	9	0.67
Moist non-tussock tundra	-	-	-	-	1	4	7	-	14	2	2	-	1	1	-	32	0.44
Shrubby moist non-tussock tundra	-	-	-	1	2	-	4	-	2	5	4	-	1	-	-	19	0.26
Low to tall moist shrub	-	-	-	-	1	1	-	-	1	6	11	2	4	-	-	26	0.42
Tall shrub	-	-	-	-	-	-	-	-	-	-	-	2	-	-	-	2	1.00
Raised areas in wet tundra	-	-	-	-	-	-	1	-	-	1	-	-	3	1	-	6	0.50
Wet tundra	-	-	-	-	-	1	-	-	-	-	-	-	1	2	-	4	0.50
Water	-	-	-	-	-	-	-	-	-	-	-	-	-	-	8	8	1.00
Total plots	7	6	14	11	10	15	25	14	28	19	21	4	10	4	8	196	
Producer's accuracy	1.00	0.83	0.71	0.55	0.50	0.40	0.48	0.43	0.50	0.26	0.52	0.50	0.30	0.50	1.00		

Overall accuracy:	0.52
Balanced accuracy:	0.57
Kappa:	0.47
Weighted Kappa:	0.65

Table 4.5. Confusion matrix and accuracy metrics including all reference plots.

Mapped	Reference: Barren	Rock	Dry exposed tundra	Dry Sheltered Tundra	Low dense shrub	Moist snowbed	Tussock tundra	Shrubby tussock tundra	Moist non-tussock tundra	Shrubby moist non-tussock tundra	Low to tall moist shrub	Tall shrub	Raised areas in wet tundra	Wet tundra	Water	Total plots	User's accuracy
Barren	28	-	-	-	-	-	-	-	-	-	-	-	-	-	-	28	1.00
Rock	-	23	-	-	-	-	-	-	-	-	-	-	-	-	-	23	1.00
Dry exposed tundra	-	1	48	3	-	1	-	-	-	-	-	-	-	-	-	53	0.91
Dry Sheltered Tundra	-	-	2	40	-	-	-	-	1	1	1	-	-	-	-	45	0.89
Low dense shrub	-	-	-	1	42	-	-	-	1	-	3	-	-	-	-	47	0.89
Moist snowbed	-	-	2	-	1	51	-	-	3	-	-	-	-	-	-	57	0.89
Tussock tundra	-	-	-	-	-	2	87	8	8	3	3	-	1	-	-	112	0.78
Shrubby tussock tundra	-	-	-	-	-	-	1	49	-	2	-	-	-	-	-	52	0.94
Moist non-tussock tundra	-	-	-	-	1	5	7	-	96	2	2	-	1	1	-	115	0.83
Shrubby moist non-tussock tundra	-	-	-	1	2	-	4	-	2	62	4	-	1	-	-	76	0.82
Low to tall moist shrub	-	-	-	-	1	1	-	-	1	7	71	2	4	-	-	87	0.82
Tall shrub	-	-	-	-	-	-	-	-	-	-	-	15	-	-	-	15	1.00
Raised areas in wet tundra	-	-	-	-	-	-	1	-	-	2	-	-	35	1	-	39	0.90
Wet tundra	-	-	-	-	-	1	-	-	-	-	-	-	1	15	-	17	0.88
Water	-	-	-	-	-	-	-	-	-	-	-	-	-	-	34	34	1.00
Total plots	28	24	52	45	47	61	100	57	112	79	84	17	43	17	34	800	
Producer's accuracy	1.00	0.96	0.92	0.89	0.89	0.84	0.87	0.86	0.86	0.78	0.85	0.88	0.81	0.88	1.00		

Overall accuracy:	0.87
Balanced accuracy:	0.89
Kappa:	0.86
Weighted Kappa:	0.89

3.3. Mapping

The final maps are 4-bit unsigned integer 20 cm resolution rasters. Figures 4.2, 4.4, and 4.6 show the full extent of the maps for the Toolik, Pipeline, and Imnavait footprints; figures 4.3, 4.5, and 4.7 each show a detail from an area within the larger footprints. Minor flight-line artifacts are visible in a few areas, notably in the southern portion of the Imnavait footprint; these are likely the result of sun-sensor geometry interacting with the vegetation canopy and the slope of the terrain, potentially along with slight inconsistencies in cloud cover between flight overpasses. The effect appears to cause some tussock tundra areas to be classed as Shrubby Moist Non-Tussock Tundra, presumably because the effect increased the apparent greenness and reduced the prominence of tussock shadows at the outer margins of the flight line.

It is difficult to compare the maps directly to the relevant Alaska Geobotany Center maps, which are polygon-based rather than raster-based and have larger minimum mapping units, but the landscape patterns are generally congruent. Unlike the Alaska Geobotany Center maps, our model was unable to distinguish between acidic and non-acidic tundra pixels, which was somewhat surprising since these types can often be distinguished in coarser remote-sensing data. It may be that additional input layers or better attention paid to the reference plot data might permit these types to be differentiated in future efforts.

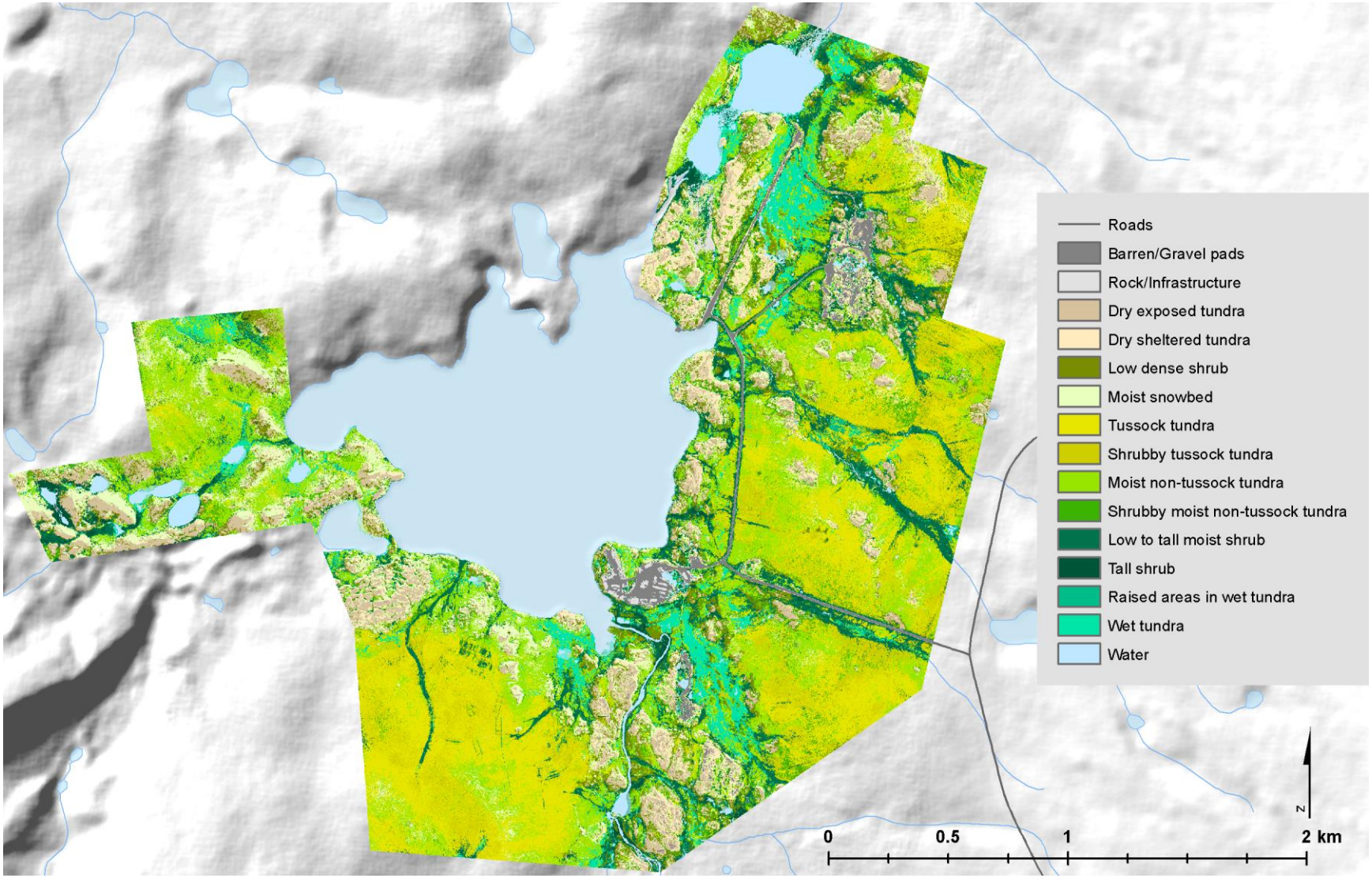

Figure 4.2. Map of vegetation communities for the Toolik footprint shown at 1:25,000 scale.

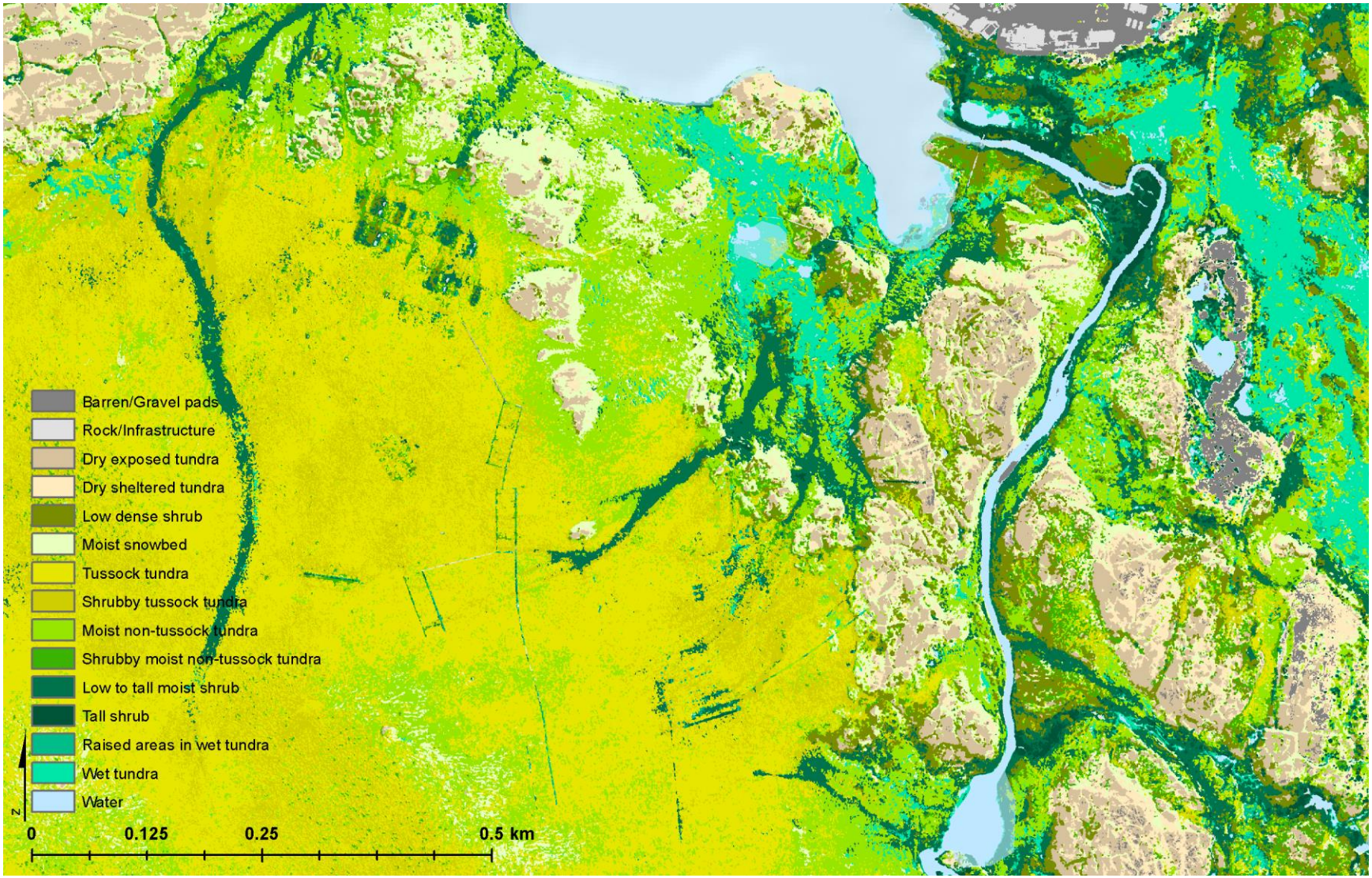

Figure 4.3. 1:6500 scale detail of a well-known research area south of Toolik Field Station (visible at top right), showing the Toolik Lake inlet draining into Toolik Lake, as well as several blocks of research plots, including LTER plots.

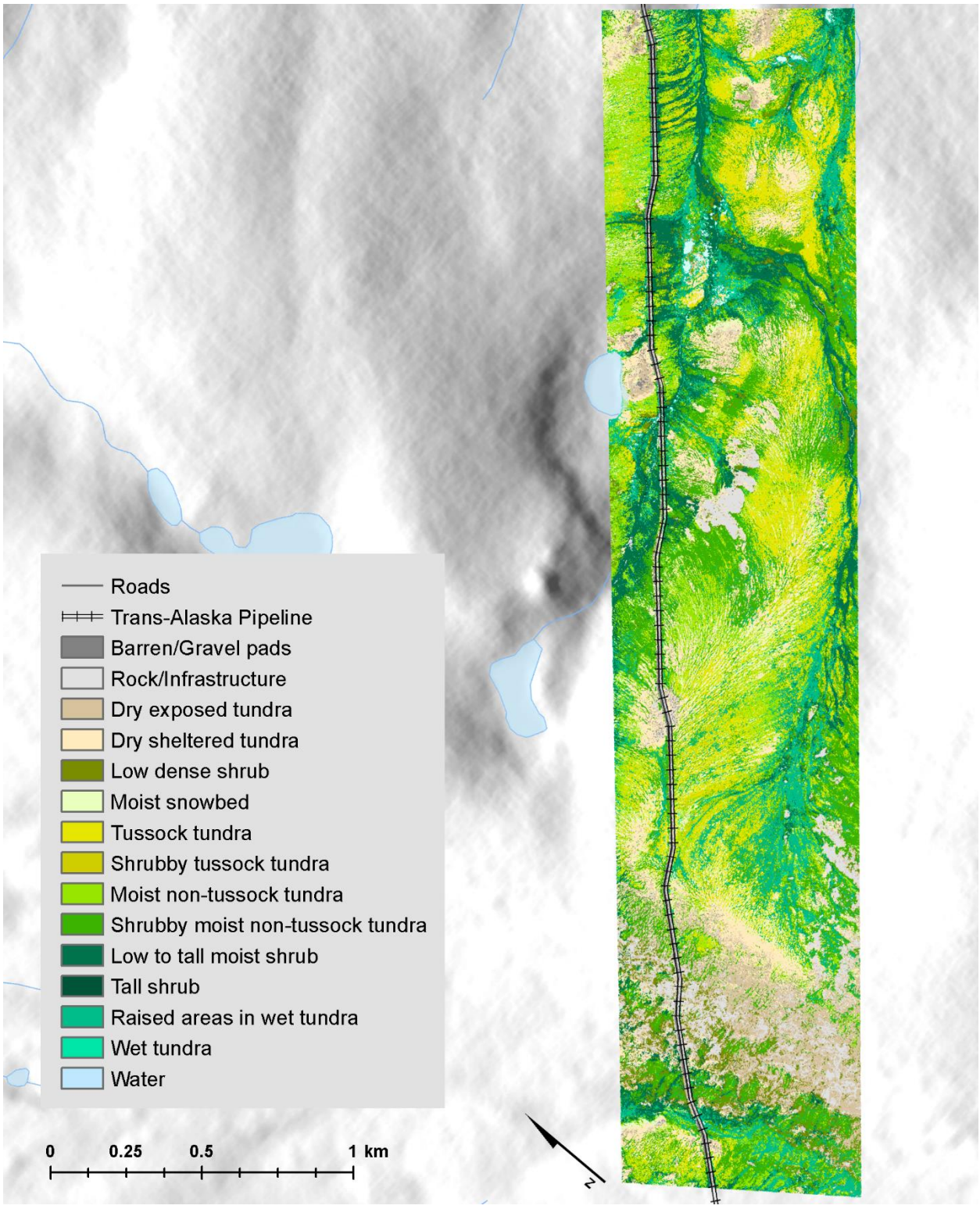

Figure 4.4. Map of vegetation communities for the Pipeline footprint shown at 1:19,500 scale. The footprint is rotated (note the north arrow) to allow a better fit on the page.

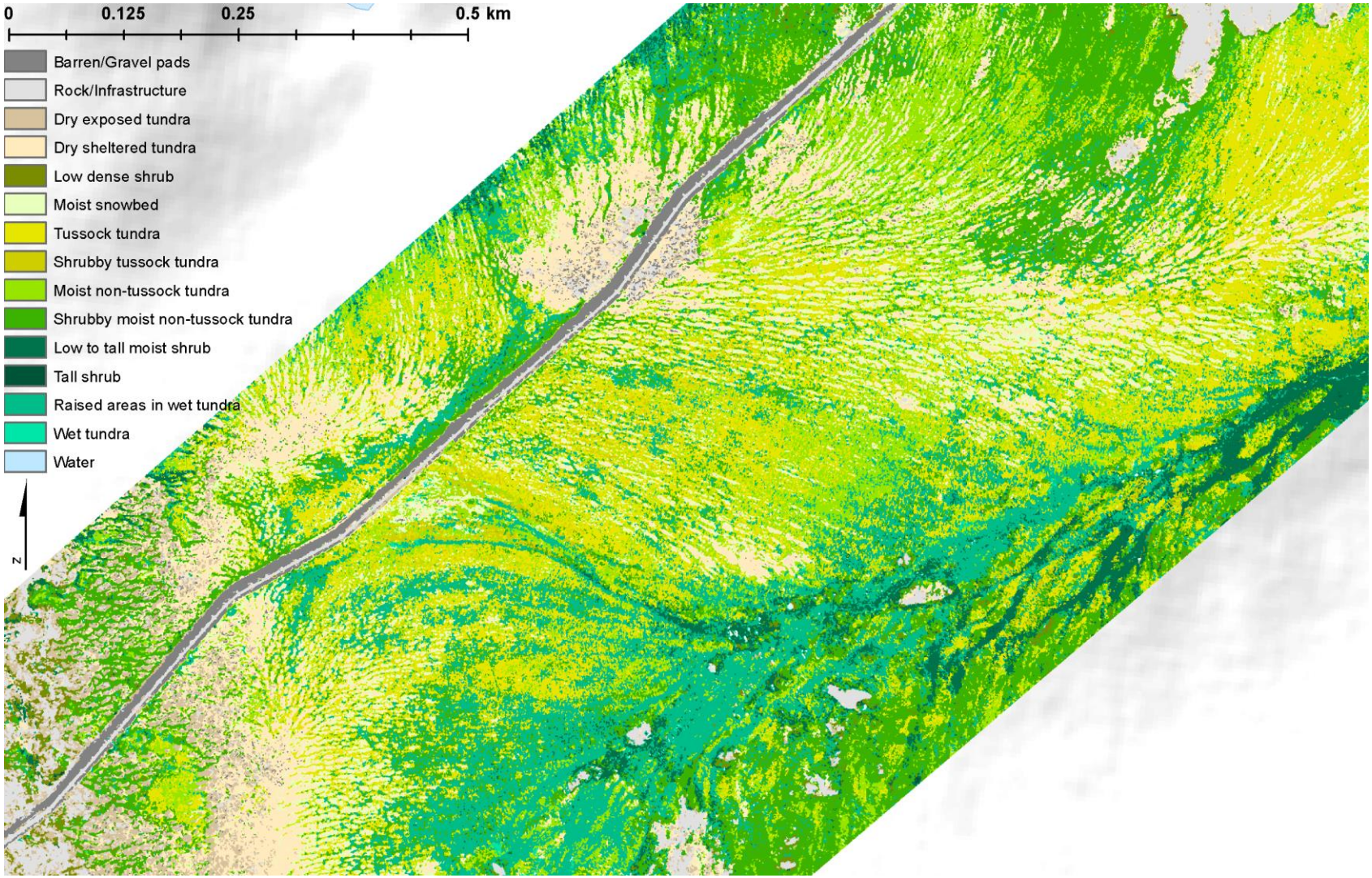

Figure 4.5. 1:6500 scale detail of an area within the Pipeline footprint.

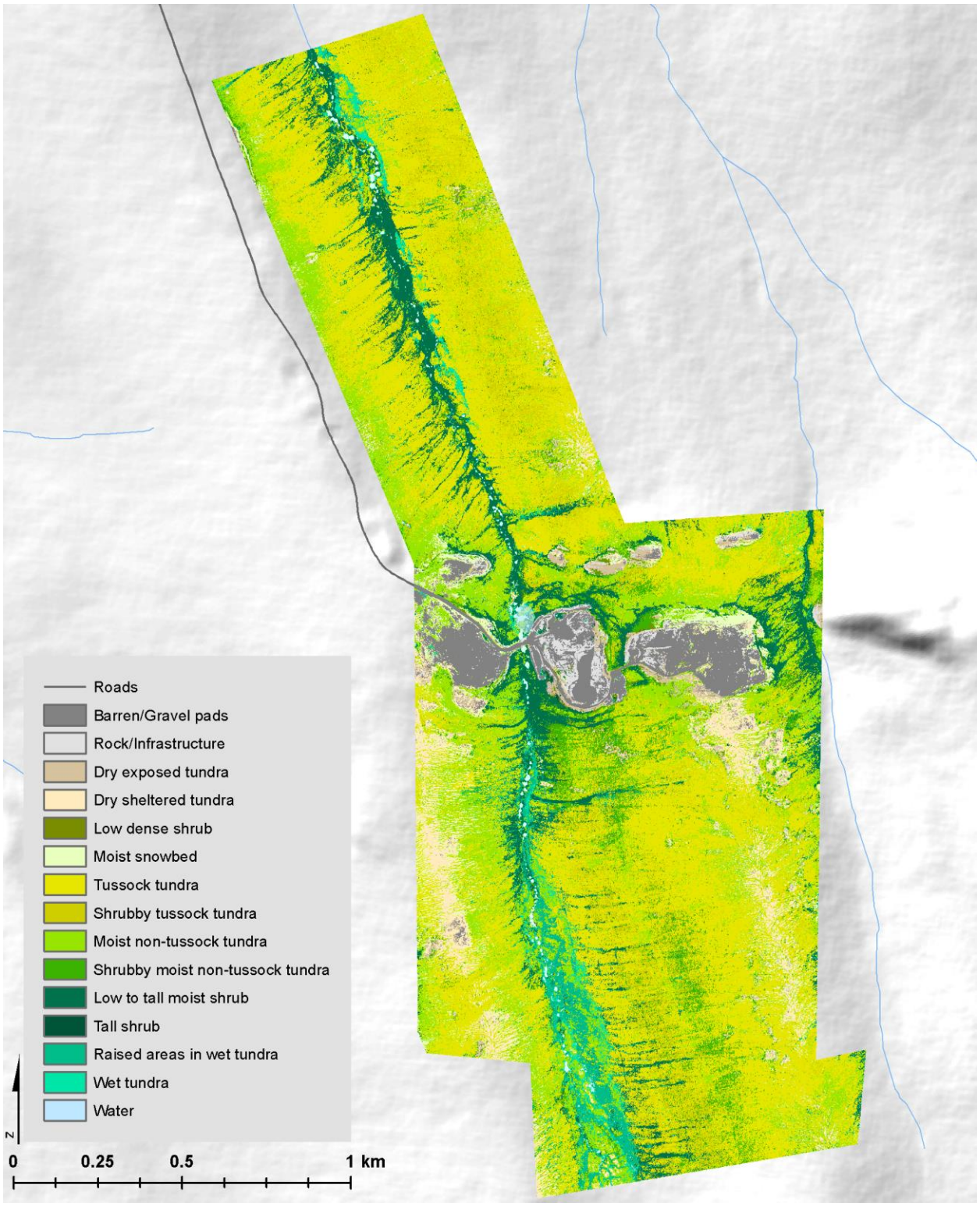

Figure 4.6. Map of vegetation communities for the Imnavait footprint shown at 1:17,500 scale.

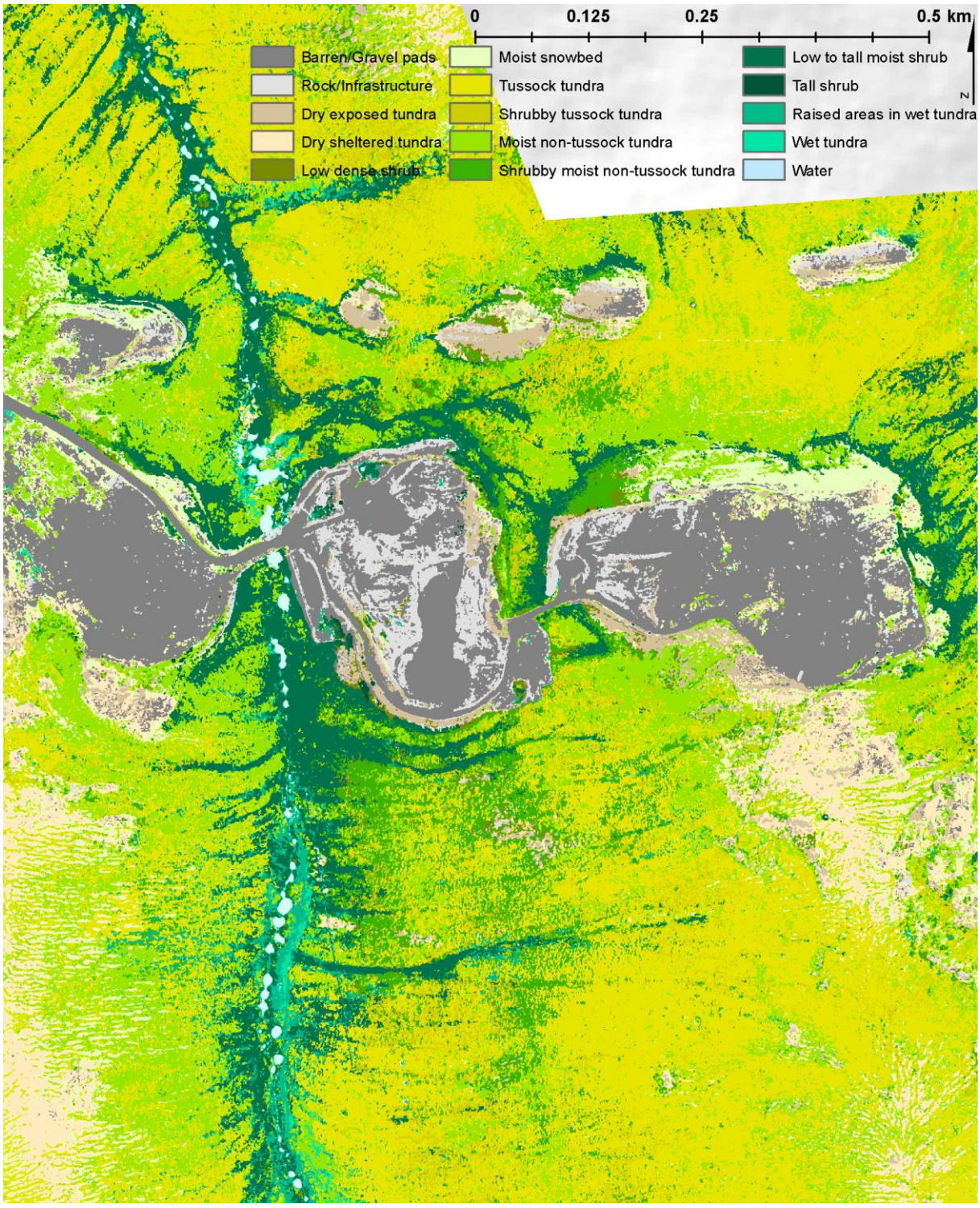

Figure 4.7. 1:6500 scale detail of a well-known research area within the Imnavait footprint.

Acknowledgements

This work was supported by NASA Terrestrial Ecology grant NNX12AK83G awarded to LAV, NASA Earth Science Fellowship NNX15AP04H awarded to HEG, and NASA Idaho Space Grant Fellowship NNX10AM75H awarded to TSM. Airborne lidar and imagery data were collected by Kodiak Mapping, Inc., Palmer, AK, www.kodiakmapping.com. Random Forest modeling was informed and improved by many interesting discussions with Patrick Fekety. Field assistance from Elizabeth Fortin was invaluable, and Skip Walker provided generous feedback and advice on the maps. The authors are also grateful for the support of the staff and greater research community of Toolik Field Station, Institute of Arctic Biology, University of Alaska Fairbanks, with special thanks to Jason Stuckey, Randy Fulweber, and Jorge Noguera of Toolik GIS for assistance with GNSS and lidar ground control.

References

ACIA, 2005. Arctic Climate Impact Assessment. Cambridge University Press, Cambridge, UK.

Atkinson, D.M., Treitz, P., 2012. Arctic ecological classifications derived from vegetation community and satellite spectral data. Remote Sens. 4, 3948–3971. doi:10.3390/rs4123948

Beck, P.S.A., Horning, N., Goetz, S.J., Loranty, M.M., Tape, K.D., 2011. Shrub cover on the North Slope of Alaska: a circa 2000 baseline map. Arctic, Antarct. Alp. Res. 43, 355–363. doi:10.1657/1938-4246-43.3.355

Boehner, J., Koethe, R., Conrad, O., Gross, J., Ringeler, A., Selige, T., 2002. Soil Regionalisation by means of terrain analysis and process parameterisation, in: Micheli, E., Nachtergaele, F., Montanarella, L. (Eds.), Soil Classification 2001. European Soil Bureau, Research Report No. 7, EUR 20398 EN. Luxembourg, pp. 213–222.

Boelman, N., Gough, L., Wingfield, J., Goetz, S.J., Asmus, A., Chmura, H., Krause, J., Jonathan, P., Sweet, S., Guay, K., 2014. Greater shrub dominance alters breeding habitat and food resources for migratory songbirds in Alaskan arctic tundra. Glob. Chang. Biol. doi:10.1111/gcb.12761

Braun-Blanquet, J., 1965. Plant Sociology: The Study of Plant Communities. Hafner Publishing Company.

Breiman, L., 2001. Random forests. Mach. Learn. 45, 5–32. doi:10.1023/A:1010933404324

Brenning, A., 2008. Statistical geocomputing combining R and SAGA: The example of landslide susceptibility analysis with generalized additive models, in: J. Boehner, J., Blaschke, T., Montanarella, L. (Eds.), SAGA - Seconds Out (= Hamburger Beitraege Zur Physischen Geographie Und Landschaftsoekologie, Vol. 19). pp. 23–32.

Chen, C., Liaw, A., Breiman, L., 2004. Using random forest to learn imbalanced data, University of California, Berkeley Statistics Technical Reports. doi:ley.edu/sites/default/files/tech-reports/666.pdf

Chust, G., Galparsoro, I., Borja, Á., Franco, J., Uriarte, A., 2008. Coastal and estuarine habitat mapping, using LIDAR height and intensity and multi-spectral imagery. Estuar. Coast. Shelf Sci. 78, 633–643. doi:10.1016/j.ecss.2008.02.003

Cohen, J., 1968. Weighted Kappa: Nominal scale agreement with provision for scaled disagreement or partial credit. Psychol. Bull. 70, 213–220.

Conrad, O., Bechtel, B., Bock, M., Dietrich, H., Fischer, E., Gerlitz, L., Wehberg, J., Wichmann, V., Böhner, J., 2015. System for Automated Geoscientific Analyses (SAGA) v. 2.1.4. Geosci. Model Dev. 8. doi:10.5194/gmd-8-1991-2015

Crookston, N.L., Finley, A.O., 2007. yaImpute: An R Package for k-NN Imputation. J. Stat. Softw. 23, 1–16.

Davidson, S., Santos, M., Sloan, V., Watts, J., Phoenix, G., Oechel, W., Zona, D., 2016. Mapping Arctic Tundra Vegetation Communities Using Field Spectroscopy and Multispectral Satellite Data in North Alaska, USA. Remote Sens. 8, 978. doi:10.3390/rs8120978

Dirnböck, T., Dullinger, S., Gottfried, M., Ginzler, C., Grabherr, G., 2003. Mapping alpine vegetation based on image analysis, topographic variables and Canonical Correspondence Analysis. Appl. Veg. Sci. 6, 85–96. doi:10.1111/j.1654-109X.2003.tb00567.x

Dormann, C.F., Elith, J., Bacher, S., Buchmann, C., Carl, G., Carré, G., Marquéz, J.R.G., Gruber, B., Lafourcade, B., Leitão, P.J., Münkemüller, T., Mcclean, C., Osborne, P.E., Reineking, B., Schröder, B., Skidmore, A.K., Zurell, D., Lautenbach, S., 2013. Collinearity: A review of methods to deal with it and a simulation study evaluating their performance. Ecography (Cop.). 36, 027–046. doi:10.1111/j.1600-0587.2012.07348.x

Evans, J., Oakleaf, J., Cushman, S., Theobald, D., 2014. An ArcGIS Toolbox for Surface Gradient and Geomorphometric Modeling, version 2.0-0.

Evans, J.S., Cushman, S.A., 2009. Gradient modeling of conifer species using random forests. Landsc. Ecol. 24, 673–683. doi:10.1007/s10980-009-9341-0

Gottfried, M., Pauli, H., Grabherr, G., 2014. Prediction of vegetation patterns at the limits of plant life: A new view of the alpine-nival ecotone. Arct. Alp. Res. 30, 207–221.

Greaves, H.E., Vierling, L.A., Eitel, J.U.H., Boelman, N.T., Magney, T.S., Prager, C.M., Griffin, K.L., 2017. Applying terrestrial lidar for evaluation and calibration of airborne lidar-derived shrub biomass estimates in Arctic tundra. Remote Sens. Lett. 8, 175–184. doi:10.1080/2150704X.2016.1246770

Greaves, H.E., Vierling, L.A., Eitel, J.U.H., Boelman, N.T., Magney, T.S., Prager, C.M., Griffin, K.L., 2016. High-resolution mapping of aboveground shrub biomass in Arctic tundra using airborne lidar and imagery. Remote Sens. Environ. 184, 361–373. doi:10.1016/j.rse.2016.07.026

Hijmans, R.J., 2015. raster: Geographic Data Analysis and Modeling. R package version 2.3-40. http://CRAN.R-project.org/package=raster.

Huryn, A., Hobbie, J., 2012. Land of Extremes: A Natural History of the Arctic North Slope of Alaska. University of Alaska Press, Fairbanks, AK.

Isenburg, M., 2017. LAStools - Efficient tools for lidar processing. Version 170327. http://lastools.org.

Kuhn, M., 2016. caret: Classification and Regression Training. R package version 6.0-73.

Kushida, K., Hobara, S., Tsuyuzaki, S., Kim, Y., Watanabe, M., Setiawan, Y., Harada, K., Shaver, G.R., Fukuda, M., 2015. Spectral indices for remote sensing of phytomass, deciduous shrubs, and productivity in Alaskan Arctic tundra. Int. J. Remote Sens. 36, 4344–4362. doi:10.1080/01431161.2015.1080878

Lang, M.W., McCarty, G.W., 2009. Lidar intensity for improved detection of inundation below the forest canopy. Wetlands 29, 1166–1178. doi:10.1672/08-197.1

Langford, Z., Kumar, J., Hoffman, F., Norby, R., Wullschleger, S., Sloan, V., Iversen, C., 2016. Mapping Arctic Plant Functional Type Distributions in the Barrow Environmental Observatory Using WorldView-2 and LiDAR Datasets. Remote Sens. 8. doi:10.3390/rs8090733

Liaw, A., Wiener, M., 2002. Classification and Regression by randomForest. R news 2, 18–22. doi:10.1177/154405910408300516

Martinuzzi, S., Vierling, L.A., Gould, W.A., Falkowski, M.J., Evans, J.S., Hudak, A.T., Vierling, K.T., 2009. Mapping snags and understory shrubs for a LiDAR-based assessment of wildlife habitat suitability. Remote Sens. Environ. 113, 2533–2546. doi:10.1016/j.rse.2009.07.002

McCune, B., Keon, D., 2002. Equations for potential annual direct incident radiation and heat load. J. Veg. Sci. 13, 603–606. doi:10.1111/j.1654-1103.2002.tb02087.x

Naito, A.T., Cairns, D.M., 2011. Relationships between Arctic shrub dynamics and topographically derived hydrologic characteristics. Environ. Res. Lett. 6, 45506. doi:10.1088/1748-9326/6/4/045506

Nicodemus, K.K., Malley, J.D., Strobl, C., Ziegler, A., 2010. The behaviour of random forest permutation-based variable importance measures under predictor correlation. BMC Bioinformatics 11. doi:10.1186/1471-2105-11-110

Oechel, W.C., Vourlitis, G.L., Verfaillie, J., Crawford, T., Brooks, S., Dumas, E., Hope, A., Stow, D., Boynton, B., Nosov, V., Zulueta, R., 2000. A scaling approach for quantifying the net CO2 flux of the Kuparuk River Basin, Alaska. Glob. Chang. Biol. 6, 160–173. doi:10.1046/j.1365-2486.2000.06018.x

Ohmann, J.L., Gregory, M.J., 2002. Predictive mapping of forest composition and structure with direct gradient analysis and nearest- neighbor imputation in coastal Oregon , U . S . A . Can. J. For. Res. 741, 725–741. doi:10.1139/X02-011

Osterkamp, T.E., 2005. The recent warming of permafrost in Alaska 49, 187–202. doi:10.1016/j.gloplacha.2005.09.001

Plattner, C., Braun, L.N., Brenning, A., 2004. Spatial variability of snow accumulation on Vernagtferner, Austrian Alps, in winter 2003/2004. Zeitschrift fuer Gletscherkd. und Glazialgeol. 39, 43–47.

R Core Team, 2017. R: A language and environment for statistical computing. R Found. Stat. Comput. Vienna, Austria. URL http//www.R-project.org/.

Raynolds, M.K., Walker, D.A., Maier, H.A., 2005. Plant community-level mapping of arctic Alaska based on the circumpolar arctic vegetation map. Phytocoenologia 35, 821–848. doi:10.1127/0340-269X/2005/0035-0821

Reese, H., Nyström, M., Nordkvist, K., Olsson, H., 2014. Combining airborne laser scanning data and optical satellite data for classification of alpine vegetation. Int. J. Appl. Earth Obs. Geoinf. 27, 81–90. doi:10.1016/j.jag.2013.05.003

Richardson, A.D., Jenkins, J.P., Braswell, B.H., Hollinger, D.Y., Ollinger, S. V., Smith, M.L., 2007. Use of digital webcam images to track spring green-up in a deciduous broadleaf forest. Oecologia 152, 323–334. doi:10.1007/s00442-006-0657-z

Stow, D.A., Hope, A., McGuire, D., Verbyla, D., Gamon, J., Huemmrich, F., Houston, S., Racine, C., Sturm, M., Tape, K., Hinzman, L., Yoshikawa, K., Tweedie, C., Noyle, B., Silapaswan, C., Douglas, D., Griffith, B., Jia, G., Epstein, H., Walker, D., Daeschner, S., Petersen, A., Zhou, L., Myneni, R., 2004. Remote sensing of vegetation and land-cover change in Arctic Tundra Ecosystems. Remote Sens. Environ. 89, 281–308. doi:10.1016/j.rse.2003.10.018

Vierling, L.A., Eitel, J.U.H., Boelman, N.T., Griffin, K.L., Greaves, H., Magney, T.S., Prager, C., Ajayi, M., Gibson, R., 2013a. Bare earth LiDAR dataset for Toolik Field Station, AK, and nearby field sites along Dalton Highway. doi:10.7923/G4057CV5.

Vierling, L.A., Eitel, J.U.H., Boelman, N.T., Griffin, K.L., Greaves, H., Magney, T.S., Prager, C., Ajayi, M., Gibson, R., 2013b. Four-band, 5cm resolution orthophotographs of Toolik Field Station, AK, and nearby field sites along Dalton Highway. doi 10.7923/G4VD6WCW.

Walker, D.A., Barry, N.C., 1991. Toolik Lake permanent vegetation plots: Site factors, soil physical and chemical properties, plant species, cover photographs, and soil descriptions. R4D Progr. Data Rep.

Walker, D.A., Maier, H.A., 2007. Geobotanical maps in the vicinity of the Toolik Lake Field Station, Alaska. Inst. Arct. Biol. Biol. Pap. Univ. Alaska, No. 27.

Walker, D.A., Raynolds, M.K., Daniëls, F.J., Einarsson, E., Elvebakk, A., Gould, W.A., Katenin, A.E., Kholod, S.S., Markon, C.J., Melnikov, E.S., Moskalenko, N.G., Talbot, S.S., Yurtsev, B.A., CAVM Team, 2005. The Circumpolar Arctic vegetation map. J. Veg. Sci. 16, 267–282.

Walker, D.A., Walker, M.D., 1996. Terrain and Vegetation of the Imnavait Creek Watershed, in: Reynolds, J.F., Tenhunen, J.D. (Eds.), Landscape Function: Implications for Ecosystem Disturbance, a Case Study in Arctic Tundra. Springer-Verlag, New York, NY, pp. 73–108.

Walker, M.D., Walker, D.A., Auerbach, N.A., 1994. Plant communities of a tussock tundra landscape in the Brooks Range foothills, Alaska. J. Veg. Sci. 5, 843–866.

Walter, K.M., Smith, L.C., Chapin, F.S., 2007. Methane bubbling from northern lakes: present and future contributions to the global methane budget. Philos. Trans. R. Soc. A Math. Phys. Eng. Sci. 365, 1657–1676. doi:10.1098/rsta.2007.2036

Yan, W.Y., Shaker, A., 2014. Radiometric Correction and Normalization of Airborne Lidar Intensity Data for Land Cover Classification. IEEE Trans. Geosci. Remote Sens. 52, 7658–7673. doi:10.1109/TGRS.2014.2316195

Supplemental Data

Table S4.1. Crosswalk between original classification of reference plot photos and final collapsed class names.

Original class name	n	Final class name
Acidic dry prostrate dwarf-shrub	37	Dry exposed tundra
Acidic hemi-prostrate dwarf-shrub (moderately deep snowbed)	19	Shrubby moist non-tussock tundra
Acidic hemi-prostrate dwarf-shrub fruticose-lichen tundra (shallow snowbed)	45	Dry Sheltered Tundra
Acidic hemi-prostrate shrub-sedge-forb fruticose-lichen (moist shallow snowbed)	28	Moist snowbed
Barren	25	Barren
Betnan-Rubcha dwarf shrub	24	Low to tall moist shrub
Carex bigelowii-Sphagnum (acidic non-tussock sedge)	76	Moist non-tussock tundra
Dry hemi-prostrate Betnan	47	Low dense shrub
Dwarf to low-shrub tussock tundra (birch)	45	Shrubby tussock tundra
Dwarf to low-shrub tussock tundra (willow)	12	Shrubby tussock tundra
Eriophorum vaginatum-Sphagnum	100	Tussock tundra
Herbaceous marsh	9	Water
Lichen on rock	24	Rock
Low to tall shrublands (willow)	29	Low to tall moist shrub
Non-acidic dry prostrate dwarf-shrub sedge forb fruticose-lichen tundra	6	Dry exposed tundra
Non-acidic hemi-prostrate dwarf-shrub (deep snowbed)	33	Moist snowbed
Non-acidic non-tussock -sedge (subhygric to mesic)	25	Moist non-tussock tundra
Non-acidic non-tussock sedge with Cassiope and horsetails (subhygric)	9	Moist non-tussock tundra
Partially vegetated barren and disturbed	3	Barren
Prostrate dwarf-shrub (Dryas octopetala)	9	Dry exposed tundra
Riparian forb-grass meadow	13	Low to tall moist shrub
Sedge-moss tundra - poor fens (Sphagnum)	10	Wet tundra
Sedge-moss tundra (fens)	7	Wet tundra
Shrubby Carex bigelowii-Sphagnum (shrubby acidic non-tussock sedge)	60	Shrubby moist non-tussock tundra
Tall Salpul-Eriang water tracks	15	Low to tall moist shrub
Tall shrublands (riparian)	17	Tall shrub
Upland grass-forb meadow	2	Moist non-tussock tundra
Water	25	Water
Wet raised microsites	43	Raised areas in wet tundra
Wet sedge-Salix chamissonis	3	Low to tall moist shrub

Table S4.2. Weights matrix used to calculate Cohens weighted kappa. 0 indicates perfect agreement; 1, 2, and 3 indicate increasing degrees of disagreement.

	Barren	Rock	Dry exposed tundra	Dry Sheltered Tundra	Low dense shrub	Moist snowbed	Tussock tundra	Shrubby tussock tundra	Moist non-tussock tundra	Shrubby moist non-tussock tundra	Low to tall moist shrub	Tall shrub	Raised areas in wet tundra	Wet tundra	Water
Barren	0	1	1	2	3	3	3	3	3	3	3	3	3	3	3
Rock	1	0	1	2	3	3	3	3	3	3	3	3	3	3	3
Dry exposed tundra	1	1	0	1	1	3	3	3	3	3	3	3	3	3	3
Dry Sheltered Tundra	2	2	1	0	1	1	3	3	3	3	3	3	3	3	3
Low dense shrub	3	3	1	1	0	1	3	2	3	2	2	3	3	3	3
Moist snowbed	3	3	3	1	1	0	2	2	1	2	3	3	3	3	3
Tussock tundra	3	3	3	3	3	2	0	1	1	2	3	3	3	3	3
Shrubby tussock tundra	3	3	3	3	2	2	1	0	2	1	1	3	3	3	3
Moist non-tussock tundra	3	3	3	3	3	1	1	2	0	1	3	3	2	2	3
Shrubby moist non-tussock tundra	3	3	3	3	2	2	2	1	1	0	1	2	2	3	3
Low to tall moist shrub	3	3	3	3	2	3	3	1	3	1	0	1	2	2	3
Tall shrub	3	3	3	3	3	3	3	3	3	2	1	0	3	3	3
Raised areas in wet tundra	3	3	3	3	3	3	3	3	2	2	2	3	0	1	2
Wet tundra	3	3	3	3	3	3	3	3	2	3	2	3	1	0	1
Water	3	3	3	3	3	3	3	3	3	3	3	3	2	1	0

Table S4.3. The fifteen most important Random Forest variables ranked per class. Numbers represent mean decrease in class accuracy when variable was permuted. See Table 4.2 for variable explanations. (Table continues next page.)

Barren		Rock		Dry exposed tundra		Dry snowbed		Low dense shrub		Moist snowbed		Tussock tundra		Shrubby tussock tundra	
dsi_1	0.136	ndvi_1	0.134	int_1	0.092	pan_1	0.100	2grbi_05	0.110	pctr_1	0.080	pctr_1	0.044	2grbi_05	0.111
hue_1	0.135	pctb_1	0.128	tpi_5	0.092	int_1	0.099	dsi_05	0.101	hli_05	0.075	pan_sd	0.035	pctb_1	0.108
dsi_05	0.133	ndvi_05	0.112	pctb_1	0.085	tpi_250	0.090	2grbi_1	0.101	hue_1	0.071	pctb_1	0.032	2grbi_1	0.100
2grbi_1	0.129	dsi_1	0.110	tpi_10	0.081	2grbi_05	0.087	dsi_1	0.094	tpi_250	0.069	ndvi_05	0.029	pctr_1	0.093
ndvi_1	0.129	dsi_05	0.104	int	0.078	2grbi_1	0.087	ndvi_05	0.088	2grbi_05	0.068	pan_1	0.028	ndvi_05	0.091
2grbi_05	0.120	int_1	0.098	pctr_1	0.078	pctb_1	0.085	tpi_10	0.088	tpi_100	0.067	cnht_sm1	0.027	tpi_250	0.088
ndvi_05	0.115	pctr_1	0.095	tpi_250	0.075	ndvi_1	0.085	tpi_250	0.085	pctb_1	0.065	ndvi_1	0.026	ndvi_1	0.085
pctb_1	0.091	hue_sd	0.088	cnht_sd	0.074	hue_1	0.084	tpi_5	0.083	2grbi_1	0.065	dtm	0.025	dsi_1	0.084
cnht_sd	0.079	int	0.086	cnht_sm1	0.073	tpi_100	0.081	int_1	0.082	ws_05	0.064	dsi_1	0.025	tpi_100	0.083
biomass	0.079	2grbi_05	0.068	tpi_100	0.072	ndvi_05	0.077	tpi_100	0.081	tpi_5	0.063	dsi_05	0.025	tpi_10	0.082
pan_1	0.070	site	0.068	tpi_25	0.069	int	0.077	ndvi_1	0.080	ws_1	0.063	2grbi_1	0.025	dsi_05	0.080
hue_sd	0.067	2grbi_1	0.067	tpi_50	0.067	biomass	0.076	pctr_1	0.080	ndvi_1	0.063	cnht_sm05	0.025	site	0.079
swi_05	0.058	pan_sd	0.057	biomass	0.066	pctr_1	0.076	swi_05	0.078	tpi_50	0.063	int_1	0.024	pan_1	0.075
cnht_sm1	0.055	dtm	0.057	swi_05	0.066	dsi_05	0.075	tpi_25	0.076	ndvi_05	0.061	tpi_25	0.024	tpi_50	0.075
tpi_10	0.048	ws_1	0.052	2grbi_05	0.062	ws_1	0.073	swi_1	0.074	dsi_05	0.061	2grbi_05	0.024	tpi_5	0.075

Table S4.3 (continued). The fifteen most important Random Forest variables ranked per class. Numbers represent mean decrease in accuracy when variable was permuted. See Table 4.2 for variable explanations.

Moist non-tussock tundra		Shrubby moist non-tussock tundra		Low to tall moist shrub		Tall shrub		Raised areas in wet tundra		Wet tundra		Water		Mean Decrease in Accuracy		Mean Decrease in Gini Index	
pctr_1	0.016	tpi_250	0.054	tpi_100	0.059	cnht_sm1	0.157	site	0.120	int_sd	0.146	pan_sd	0.087	2grbi_05	0.073	int_1	42.371
int_1	0.011	2grbi_05	0.054	2grbi_1	0.058	cnht_sm05	0.149	int_sd	0.115	pctr_1	0.144	int_1	0.084	dsi_05	0.072	ndvi_1	40.387
pctb_1	0.010	2grbi_1	0.052	dsi_1	0.055	cnht_sd	0.148	tpi_250	0.102	hue_1	0.143	dtm_sd	0.083	ndvi_1	0.071	cnht_sd	39.822
ndvi_05	0.009	tpi_100	0.050	tpi_250	0.054	biomass	0.130	pctr_1	0.093	dtm	0.131	pan_1	0.078	pctr_1	0.070	dsi_05	39.716
int	0.008	dsi_1	0.049	2grbi_05	0.053	dtm	0.108	tpi_100	0.090	tpi_250	0.128	dsi_05	0.074	dsi_1	0.070	ndvi_05	39.379
dsi_1	0.008	dsi_05	0.049	dsi_05	0.051	dsi_05	0.094	2grbi_05	0.089	2grbi_05	0.110	ndvi_05	0.073	pctb_1	0.069	biomass	39.313
hue_1	0.008	ndvi_1	0.049	pctb_1	0.048	pctr_1	0.094	int	0.088	swi_1	0.110	ndvi_1	0.073	2grbi_1	0.069	dsi_1	38.918
cnht_sm05	0.007	site	0.046	ndvi_1	0.046	tpi_5	0.091	int_1	0.088	int	0.110	int	0.073	ndvi_05	0.069	2grbi_1	38.543
hue_sd	0.007	pctr_1	0.046	tpi_50	0.044	swi_05	0.088	dtm	0.085	tpi_100	0.108	tpi_100	0.064	tpi_250	0.066	2grbi_05	38.446
2grbi_05	0.006	hue_1	0.044	ndvi_05	0.043	tpi_10	0.084	dsi_05	0.085	tpi_10	0.107	tpi_250	0.061	hue_1	0.066	pctb_1	38.260
dsi_05	0.006	pctb_1	0.044	cnht_sm1	0.042	hue_1	0.078	ndvi_1	0.085	int_1	0.106	2grbi_05	0.061	int_1	0.065	hue_1	38.225
tpi_10	0.006	dtm	0.043	biomass	0.041	tpi_250	0.078	tpi_10	0.085	tpi_50	0.105	dsi_1	0.057	tpi_100	0.062	cnht_sm1	37.854
cnht_sd	0.006	int_1	0.043	hue_1	0.040	2grbi_05	0.078	tpi_50	0.084	swi_05	0.101	tpi_10	0.057	cnht_sd	0.060	int	37.073
tpi_25	0.005	tpi_50	0.043	tpi_25	0.039	tpi_100	0.077	cnht_sd	0.083	dtm_sd	0.100	dtm	0.056	tpi_10	0.060	cnht_sm05	36.621
biomass	0.005	ndvi_05	0.043	pctr_1	0.037	dsi_1	0.077	pctb_1	0.082	hue_sd	0.099	swi_05	0.055	dtm	0.059	pctr_1	36.431

APPENDIX A: COPYRIGHT PERMISSION FROM ELSEVIER

Elsevier (publisher of *Remote Sensing of Environment*) permits inclusion of published journal articles in theses and dissertations without explicit written permission under their Author's Rights documentation, which is currently available at http://www.elsevier.com/about/company-information/policies/copyright#Author%20rights. (Confirmed via email by Laura Stingelin, Elsevier Permissions Helpdesk Associate, May 23, 2017.)

APPENDIX B: COPYRIGHT PERMISSION FROM TAYLOR & FRANCIS

Our Ref: JB/TRSL/P17/649

12TH June 2017

Dear Heather E Greaves

Thank you for your correspondence requesting permission to reproduce the following article published in our journal in your printed thesis and to be posted in your university's repository at University of Idaho.

'Applying terrestrial lidar for evaluation and calibration of airborne lidar-derived shrub biomass estimates in Arctic tundra' by Greaves, H.E., Vierling, L.A., Eitel, J.U.H., Boelman, N.T., Magney, T.S., Prager, C.M., Griffin, K.L. *Remote Sensing Letters* Vol 8:2 pp. 175-184 (2016).

We will be pleased to grant permission on the sole condition that you acknowledge the original source of publication and insert a reference to the article on the Journals website:

This is the authors accepted manuscript of an article published as the version of record in Remote Sensing Letters 27TH October 2016.
http://www.tandfonline.com/
http://dx.doi.org/10.1080/2150704X.2016.1246770

Please note that this license does not allow you to post our content on any third-party websites or repositories.

Thank you for your interest in our Journal.

Yours sincerely

Jo Bateman
Routledge, Taylor & Francis Group.
4 Park Square, Milton Park, Abingdon, Oxon, OX14 4RN, UK.
Tel: +44 (0)20 7017 7617
Fax:+44 (0)20 7017 6336
Web: www.tandfonline.com
Email: Joanne.bateman@tandf.co.uk